DEPARTMENT OF
TRANSPORTATION

Load Rating Assessment of Three Slab-Span Bridges Over Shingle Creek

Ben Dymond, Principal Investigator
Department of Civil Engineering
University of Minnesota Duluth

AUGUST 2022

Research Report
Final Report 2022-29

Technical Report Documentation Page

1. Report No. MN 2022-29	2.	3. Recipients Accession No.	
4. Title and Subtitle Load Rating Assessment of Three Slab-Span Bridges Over Shingle Creek		5. Report Date August 2022	
		6.	
7. Author(s) Kendall A. Hill, Dr. Benjamin Z. Dymond, Dr. Brock D. Hedegaard, Dr. Lauren E. Linderman		8. Performing Organization Report No.	
9. Performing Organization Name and Address Department of Civil Engineering University of Minnesota Duluth 1405 University Drive Duluth, MN 55812		10. Project/Task/Work Unit No. CTS #2021001	
		11. Contract (C) or Grant (G) No. (c) 1036194	
12. Sponsoring Organization Name and Address Minnesota Department of Transportation Office of Research & Innovation 395 John Ireland Boulevard, MS 330 St. Paul, Minnesota 55155-1899		13. Type of Report and Period Covered Final Report	
		14. Sponsoring Agency Code	
15. Supplementary Notes https://www.mndot.gov/research/reports/2022/202229.pdf			

16. Abstract (Limit: 250 words)

Three slab-span bridges crossing Shingle Creek in Brooklyn Center, Minnesota, have poor American Association of State Highway and Transportation Officials (AASHTO) load rating factors for certain truck configurations. Characterization of load distribution is useful for determining the load rating of bridges, but results in the literature have shown that the AASHTO code results in conservative load rating factors. The focus of this study was to determine if the load rating of the three concrete slab-span bridges was conservative and could be improved using results from live load testing and finite element analysis. Field testing used a suite of instrumentation that included displacement transducers, strain gauges, accelerometers, and tiltmeters. A three-dimensional solid-element finite element model was used to determine an expected range of behaviors and corroborate the field data regarding how load distributed when placed near and away from a barrier. In addition, a method for developing a simple plate model of slab span bridges was developed considering in-situ material properties and effects of secondary elements such as barriers. Results indicated that the AASHTO load rating was conservative, and an improved rating factor could be obtained considering the field test data and computational modeling results.

17. Document Analysis/Descriptors Bridge decks, Reinforced concrete, Load transfer, Load factor, Tests, Instrumentation, Finite element method, Plates (engineering)		18. Availability Statement	
19. Security Class (this report) Unclassified	20. Security Class (this page) Unclassified	21. No. of Pages 189	22. Price

LOAD RATING ASSESSMENT OF THREE SLAB-SPAN BRIDGES OVER SHINGLE CREEK

FINAL REPORT

Prepared by:

Kendall A. Hill
Dr. Benjamin Z. Dymond
Dr. Brock D. Hedegaard
Department of Civil Engineering
University of Minnesota Duluth

Dr. Lauren E. Linderman
Department of Civil, Environmental, and Geo- Engineering
University of Minnesota Twin Cities

August 2022

Published by:

Minnesota Department of Transportation
Office of Research & Innovation
395 John Ireland Boulevard, MS 330
St. Paul, Minnesota 55155-1899

ACKNOWLEDGMENTS

Funding for this research was provided by the Minnesota Department of Transportation and is gratefully acknowledged. This research would not have been possible without the expertise of the MnDOT Technical Liaison (Yihong Gao) or the Technical Advisory Panel, which consisted of Duane Green, Robert Holschbach, Edward Lutgen, and Kristine Schadegg. Their knowledge and assistance were greatly appreciated. Assistance throughout the project was provided by numerous graduate students, undergraduate students, faculty, and staff. Their invaluable contributions were also greatly appreciated.

TABLE OF CONTENTS

LIST OF TABLES

LIST OF FIGURES

EXECUTIVE SUMMARY

Three concrete slab-span bridges over Shingle Creek in Brooklyn Center, Minnesota, have operating level load ratings less than unity, which results in a permit detour route that is approximately 15 miles longer than the I-94/I-694 route across Minneapolis and St. Paul. The three Shingle Creek bridges are a bottleneck for the northern route across Minneapolis and St. Paul. Permit detours funnel traffic onto other structures, which may deteriorate faster due to extensive use on permit routes. The three slab-span structures are not scheduled for replacement or rehabilitation. Thus, the objective of this study is to either verify that the American Association of State Highway and Transportation Officials (AASHTO) rating factors are representative of the condition of the structures or that the rating factors may be changed to better reflect the bridge condition and load distribution behavior. AASHTO specifications allow for bridges to be rated using alternative methods such as diagnostic live load testing or finite element modeling. Live load tests are thus conducted on two structures in this study and guidance for modeling slab-span structures using a technique validated against the field test data is recommended.

MnDOT Bridge 27926 was selected to be the primary structure and Bridge 27925 was selected as the secondary structure for modeling and testing. Each structure was instrumented with strain gauges, linear variable displacement transducers, and accelerometers. Static tests were conducted with three-axle trucks loaded to 50 kips, and dynamic tests were conducted with an impact hammer. The field test data were used to validate a finite element model of the primary structure, and live load distribution factors were determined from the strain and displacement profiles obtained from the field data. In addition, concrete core and steel reinforcement samples were obtained from Bridge 27926 and analyzed to determine the concrete compressive strength, concrete elastic modulus, steel yield strength, and steel elastic modulus.

A complex three-dimensional finite element model was completed for Bridge 27926 and validated using data collected during field testing. A simple plate model was also developed and validated using the same field data. The models were used to obtain live load distribution factors for Bridge 27926; equivalent width values from the plate model were within 2% and 7% of those obtained from field strain and displacement data, respectively. Additionally, the plate modeling technique was applied to Bridge 27925 to determine if it was applicable to other slab-span structures. The plate model results from Bridge 27925 underestimated the maximum strain and displacement observed in the field. However, the equivalent width values for Bridge 27925 obtained from the plate model were within 15% of the equivalent widths obtained from the field test using displacement data. The equivalent width values for Bridge 27925 from the plate model were within 52% of the equivalent widths obtained from the field test using strain data for single truck positions. This was expected because Bridge 27925 has more cracking and spalling compared to Bridge 27926. The measured strain data from the field test exhibited irregular profiles across the width of the bridge, whereas the simple elastic plate model provided uniform strain results. In addition, outlier data points were retained in the strain profiles because they provided more conservative equivalent width values.

The equivalent width results were compared to the AASHTO Specification values for each structure. Overall, the AASHTO Specification was shown to be conservative. The distribution factors from field testing and modeling were implemented in the AASHTOWare Bridge Rating software used by MnDOT to load rate bridges. The primary structure load rating could be increased by 24% when the plate model distribution factors and design material properties were used or 44% when the AASHTO specification distribution factors and measured material properties (excluding concrete compressive strength) were used. Based on the AASHTOWare results using distribution factors from the field data or plate models, the three OSOW vehicle configurations provided by MnDOT had operating rating (OR) values greater than unity for single truck scenarios. It is recommended that MnDOT adopt the plate modeling technique for load rating the concrete slab-span bridges included in this study.

CHAPTER 1: INTRODUCTION

1.1 BRIDGE DESIGN AND EVALUATION

1.1.1 Concrete Slab-Span Bridges

Bridge structures typically have three main components including the substructure, superstructure, and deck. The substructure includes piers and abutments, the superstructure includes girders or framework to support the loading between the substructures, and the deck transmits the live load from the traffic to the superstructure and substructure. Concrete slab-span bridges combine the deck and superstructure into one element. Thus, the deck alone is primarily responsible for resisting the applied live loads.

Slab-span bridges are cast on a falsework form constructed from wood or other materials. Falsework is essentially a secondary structure on which the final product is built. Once the concrete is cured, the falsework can be removed. Slab-span structures can span up to 40 ft for single spans and 50 ft for three or more spans (MnDOT, 2020b). Slab-span bridges do not have girders, which allows for a lower relative structure depth. The lower structure depth facilitates the construction of curved structures and superelevated structures. The structure depth is typically between 15 and 24 in. (MnDOT, 2020b), which allows for extra clearance below the structure that might not be available if girders are in place. Additionally, these structures are cost-effective compared to other alternatives; in 2019, the unit cost per square foot to construct slab-span bridges for the Minnesota Department of Transportation (DOT) (MnDOT) was $143.34 compared to $160.81 for inverted tee-beam bridges, which are an alternative structure with similar advantages (Conkel, 2019; MnDOT, 2020b). These qualities historically made slab-span bridges an important component of local infrastructure. However, slab-span structures do have some drawbacks. Falsework and pouring concrete can lead to longer construction and roadway closures. Falsework can also impede traffic on underpasses and damaged falsework can cause the structure to be unsafe by creating an irregular or unplanned curing surface. In addition, falsework spanning public waters requires a stormwater pollution prevention plan to ensure proper removal of falsework timbers (MnDOT, 2020b). Limited span lengths increase the number of piers necessary to complete the structure (MnDOT, 2020b). Despite some limitations, slab-span structures are suited for a wide application of roadway crossings, especially short span crossings.

1.1.2 Load Rating

Load ratings are expressed in terms of a rating factor or vehicle tons. The rating factor is used to establish the carrying capacity of the bridge based on uncertainties in the load rating calculation (MnDOT, 2020a). This can result in a conservative rating number by design. However, over-conservative load ratings have been observed in many slab-span structures similar to the Shingle Creek bridges, and live load testing has been shown to reduce uncertainties related to the performance of the structure (Azizinamini et al., 1994a; Azizinamini & Choobineh, 1995; Csagoly & Lybas, 1989; Russian et al., 2020). Furthermore, rating equations do not account for secondary elements that may contribute additional capacity such as curbs and barriers.

Load restrictions limit access to certain trucking corridors, but permits may be obtained for overweight vehicles to cross structures with load restrictions. State highway authorities have provisions for vehicles above legal weight limits to traverse highway systems. While bridge structures are designed for a standard truck size and configuration, they can lose strength over time due to general wear during service. The American Association of State Highway and Transportation Officials (AASHTO) has three distinct categories for load rating: design load rating, legal load rating, and permit load rating (AASHTO, 2018a). A design load rating evaluates the bridge in its current condition with standard load factors. If the bridge capacity is determined to be lower than demands, the bridge is evaluated for legal and permit loads using further analysis and adjusted load factors. These additional load ratings allow for permits to be issued to overweight vehicles regulated by AASHTO. Permits are issued describing vehicle characteristics such as axle configuration and load. Some permits also specify permissible routes for travel. Certain vehicle configurations with special loads are not allowed to mix with normal traffic and require an escort. Permit vehicle escorts can control speed, lane position, and presence of other vehicles on the structure (AASHTO, 2018a). Two types of permits are issued for overweight vehicles: routine and special. Routine permits are for a specified load and axle configuration for a certain period, and special permits are typically for a single use route for a vehicle greatly exceeding the weight restrictions. Permit load ratings for bridges are determined using a live load based on the truck or vehicle configuration producing the largest effects in a specified vehicle class. In addition, load factors are applied to the loading based on the vehicle configuration and expected traffic conditions (AASHTO, 2018a). This results in a more precise maximum loading with a smaller factor of safety to allow for a wider range of vehicles to cross a given structure. In the 21st century, more permits are required as bridge conditions diminish with age, freight traffic increases, and detour routes become more congested.

Load ratings are obtained through calculations or live load testing of a structure. The *AASHTO Manual for Bridge Evaluation* (MBE) sets guidelines for load rating bridges. While the load rating equations have been shown to be conservative, live load testing can clarify and reduce uncertainty related to the structural performance of a bridge (Sherman et al., 2020). Live load testing is separated into two categories: diagnostic and proof. Diagnostic testing involves loading a bridge with known vehicle weights and configurations and monitoring the behavior of the structure. This can be done with both static and dynamic loads. The loads in diagnostic testing are within the acceptable carrying capacity of the structure. Proof testing involves inducing a single, usually static load on a structure to verify that it can sustain that load. Both are acceptable means of load rating a bridge according to the AASHTO MBE (2018).

Live load testing is often used to validate a computer model of the structure in question. Live load testing and computer modeling have been coupled to provide reduced uncertainties in bridge performance. Finite element analysis (FEA) can account for additional capacity observed during live load testing of bridges and thus lead to an improved load rating (Azizinamini et al., 1994c). Results from field-validated FEA models may be used for determining the load rating of a structure.

1.1.3 Slab-span Bridges Crossing Shingle Creek

The three slab-span bridges spanning Shingle Creek in Brooklyn Center, Hennepin County, Minnesota, approximately 0.6 mi. west of the Highway 100 junction are shown in Figure 1.1. Photographs of the structures are shown in Appendix A. Two of the bridges compose the eastbound and westbound lanes of I-94. The eastbound structure, Bridge 27909, was constructed in 1980, widened in 1983, and remodeled in 2003. The westbound structure, Bridge 27925, was built in 1964 and remodeled in 1980. The third bridge is the eastbound lanes of I-694, Bridge 27926, which was constructed in 1964 and remodeled in 2003 (Nelson, 2011).

Current load restrictions limit certain overweight vehicles from crossing the bridges, which lengthens trucking routes. MnDOT considers each bridge to be in poor condition per annual bridge inspection criteria. The inventory rating of the bridges is 18.3, which is less than the design rating of HS 20. Load restrictions on the Shingle Creek bridges limit truck configurations that place more than 80 kips in any of the three spans; this loading scenario is induced by most 13-axle or larger truck configurations. Without planned improvements to the structures, the only way to allow oversized, overweight (OSOW) vehicles, such as the one shown in Figure 1.2, to cross the Shingle Creek bridges would be to increase the load rating.

1.2 MOTIVATION

Evaluating bridges for permit loads can improve trucking routes and reduce travel distances. With trucking being essential for delivery of both finished and unfinished goods, it is imperative to maintain haul routes. The ability to transport goods via the highway systems can be related to positive economic growth.

MnDOT has identified critical trucking corridors on I-94, I-694, and I-494. I-94 is older than both I-494 and I-694 and has more restrictions, with the three Shingle Creek bridges being the limiting factor for OSOW vehicles. The detour for OSOW vehicles avoiding these bridges includes traveling on I-494; this route is approximately 15 miles longer and significantly more congested. Figure 1.3 depicts the detour compared to the I-94/I-694 corridor. This detour results in additional costs to the trucking industry and the people whose goods are being moved, which has negative effects on the state economy. For example, the Indiana Soybean Alliance and Indiana Corn Marketing Association found that a 20 mi. detour has been shown to cost 15 farmers between $3800 and $7500 annually (ISA & ICMC, 2015). These costs are incurred through the extended travel time resulting in increased labor and fuel costs. Reducing these immediate or first-order costs can have a positive impact on both the carriers and shippers. Savings resulting from decreased travel time can promote economic growth (U.S. DOT FHWA et al., 2009).

In addition to trucking costs, this project is motivated by safety. Improved safety is the priority of a load rating. Reduced uncertainties with the Shingle Creek structures will promote the public welfare and provide insight into the structural performance that can be expected from the bridges.

1.3 OBJECTIVES

One of three slab-span bridges spanning Shingle Creek near Brooklyn Center, Minnesota, was selected for finite element modeling and field testing to characterize the load distribution of the slab-span system. The research objectives were as follows: (1) collect data from field testing to characterize the behavior (strains, deflections, dynamic response) of a slab-span bridge under a known truck load; (2) further evaluate live load response and bridge capacity using a refined method of numerical analysis validated using field test data; (3) assess the impact of the measured and modeled live load response on bridge behavior and permit load rating; (4) and contribute to the development of guidance related to the permit load rating of these three slab-span structures.

1.4 REPORT ORGANIZATION

Chapter 2 contains the literature review. This review includes information from bridge design and load rating codes, relevant research in slab-span finite element modeling, and live load testing of bridge structures. Chapter 3 includes the instrumentation and testing plans for the field tests. This chapter also describes preliminary processing of data collected in the field. Chapter 4 details the finite element modeling technique, including the various models developed and parameters employed. Detailed finite element models using in-situ conditions for the bridges are developed for precise load rating results. Additionally, simplified plate models are developed for easy application to these and other similar structures. Chapter 5 includes equivalent width estimates using the field test data and from the various analytical models. Load rating values are also presented in this chapter. Chapter 6 summarizes the results, guidance, and recommendations determined from the conclusion of the project.

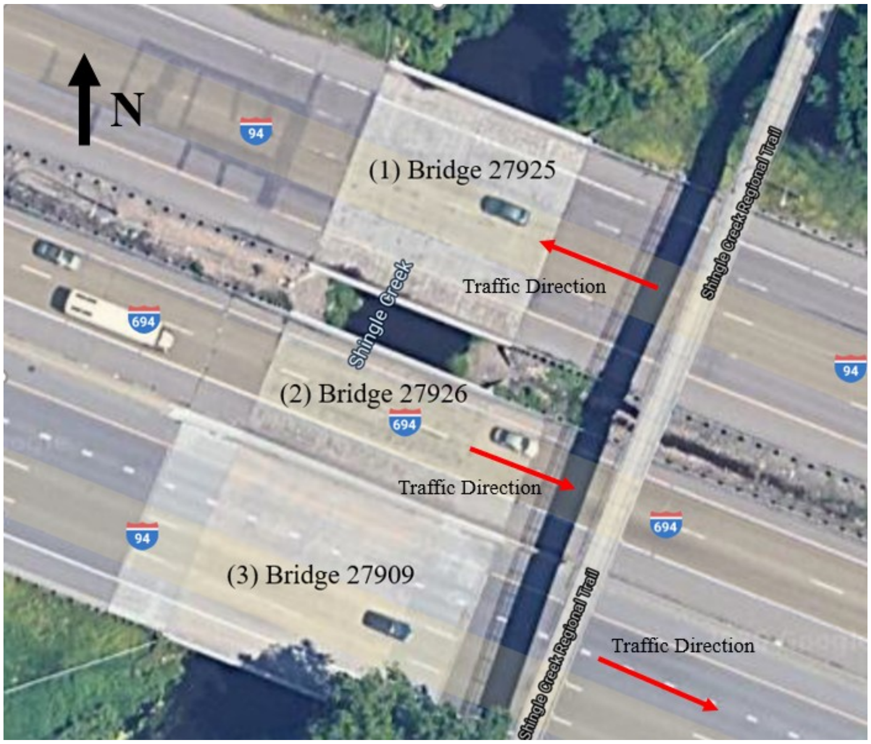

Figure 1.1 Arial view of the three slab-span bridges crossing Shingle Creek with MnDOT Bridge numbers.

Figure 1.2 OSOW vehicle hauling a windmill blade

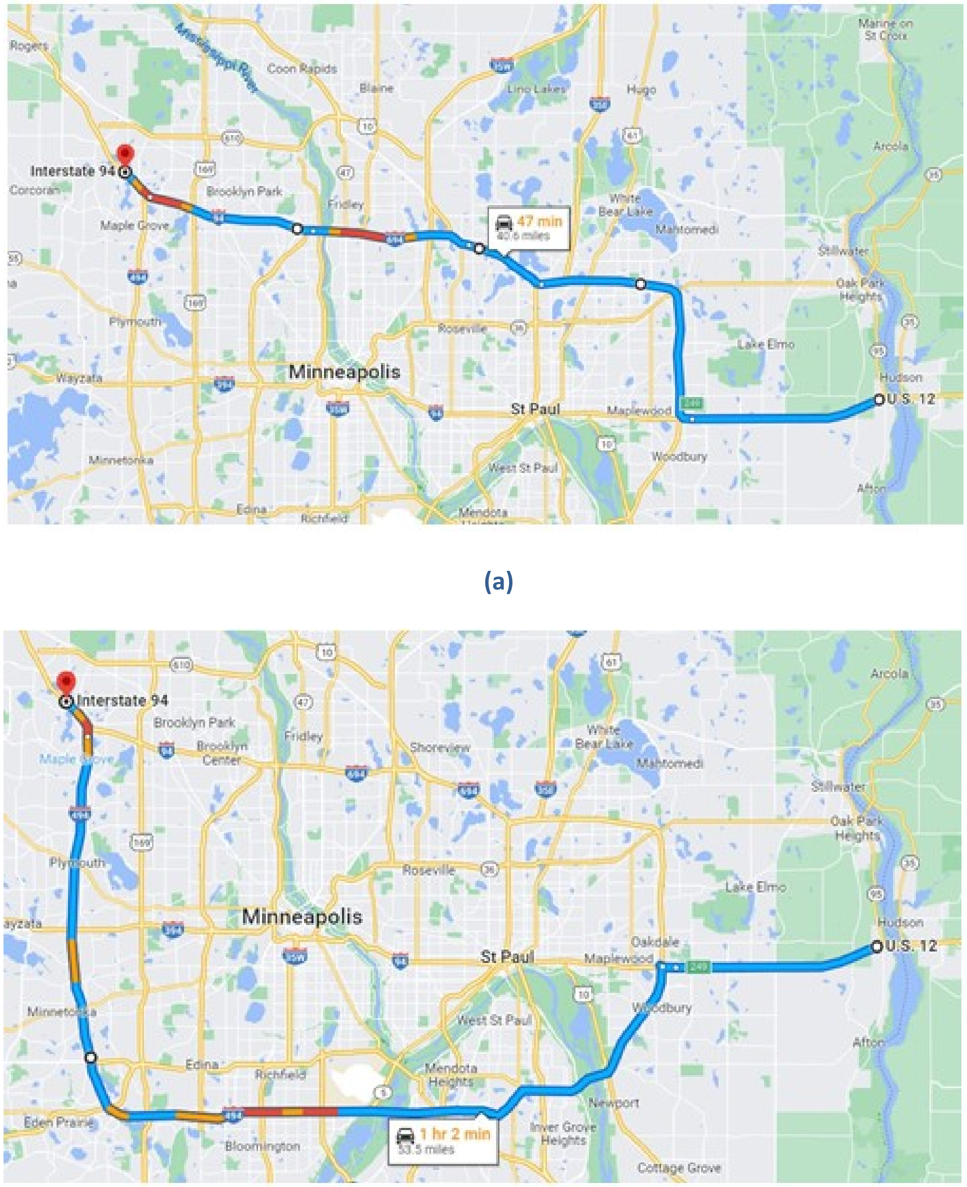

(a)

(b)

Figure 1.3 Haul routes across the Twin Cities using (a) I-94 or (b) the I-494 Shingle Creek Bridge detour, which is approximately 15 miles longer (Google, 2020).

CHAPTER 2: LITERATURE REVIEW

2.1 BRIDGE LOAD RATING

Bridge load rating attempts to balance safety, how much traffic the structure can support, economy, and how long the structure can last with reasonable maintenance, which can result in a rating that is lower than the design load. Bridge design often requires load cases specific to a particular structure, which limits the generality of bridge design. The AASHTO MBE (2018c) defines categories of loads that are evaluated when considering the load rating for a bridge. Bridge design and rating methodologies have evolved through the 20th and 21st centuries with a growing knowledge base related to bridge structural behavior. Historically, allowable stress analysis transitioned to load factor analysis, and recently, load factor analysis has given way to load and resistance factor analysis. The AASHTO and Federal Highway Administration (FHWA) set a transition date of October 1, 2007, after which all preliminary engineering on new bridges by DOTs must be designed with the AASHTO LRFD Bridge Design Specifications. However, for modifications or evaluation of existing structures, a state DOT shall have the option of using the LRFD Specifications or the specifications which were used for the original design (Densmore, 2000). The methodology behind evaluation of existing structures has been in transition from the AASHTO Manual for Condition Evaluation of Bridges (2003), which included LFR aligned with the AASHTO Standard Specifications (2002), to the MBE (2018c), which includes both LFR and LRFR aligned with the AASHTO LRFD Bridge Design Specifications (2017).

MnDOT frequently conducts special (single trip) permit load ratings in accordance with state (MnDOT, 2018) and national (AASHTO, 2018b) standards to establish efficient routes around the Metro area to meet freight and hauling demands. Permit load rating is a review of the safety and serviceability of a bridge conducted so that vehicles above the legally established weight limitations may pass over a structure. MnDOT specifies that single lane loading may be used for permit load ratings because the permit loads “are infrequent and are likely the only heavy loads on the structure during the crossing” (MnDOT, 2018).

2.1.1 Load Rating Factors

Either the LRFR or LFR methodology can be used to determine the load rating of a bridge, which is often expressed as a rating factor (RF). The following equations are used to calculate rating factors in accordance with the LFR and LRFR methods, respectively.

$$\mathrm{RF} = \frac{C_M - A_1 D}{A_2 L(1 + IM)} \tag{2.1}$$

$$\mathrm{RF} = \frac{C_S - \gamma_{DC} DC - \gamma_{DW} DW \pm \gamma_P P}{\gamma_L LL(1 + IM)} \tag{2.2}$$

Where RF is the rating factor; C_M is the member capacity; *D* is the dead load effects on the member; A_1 is the factor for the dead loads; A_2 is the factor for the live loads; *L* is the live load effects on the member; *IM* is the dynamic load allowance used with the live load effect; C_S is the structural capacity; *DC* is the dead load effect of structural components and attachments; γ_{DC} is the load factor for structural components and attachments; *DW* is the dead load effect of wearing surfaces and utilities; γ_{DW} is the load factor for wearing surfaces and utilities; *P* is the permanent loading other than dead loads; γ_P is the load factor for permanent loads other than dead loads; *LL* is the live load effect; and γ_L is the evaluation live load factor (AASHTO, 2018a). Load effects can be axial force, vertical shear force, bending moment, axial stress, shear stress, and bending stresses (AASHTO, 2018a). The live load demand used in the LRFR methodology consists of the AASHTO HL-93 design load, which includes both the HS-20 truck and a lane load; the live load demand used in the LFR method includes either the HS-20 truck load or the lane load. The HS-20 truck is defined as one 8-kip front axle load, followed by a 32-kip middle axle load 14 ft behind, followed by another 32-kip rear axle load between 14 and 30 ft behind the middle axle load. The lane load is defined as 0.64 k/ft distributed load. Once the load effect being evaluated is selected, the capacity of the structure is also determined. To compute the member rating in the LFR method, the rating factor is multiplied by the weight of the truck used to determine the live load effects as follows.

$$RT = (\mathrm{RF}) * W \tag{2.3}$$

Where *RT* is the bridge member rating in tons; RF is the rating factor, and *W* is the weight of the truck used to calculate live load effects in tons (AASHTO, 2018a). The bridge rating should be checked for each member and the overall bridge rating is typically controlled by the member with the lowest rating factor.

2.2 SLAB-SPAN BRIDGE ANALYSIS

Bridge design is dictated by design codes such as AASHTO Load and Resistance Factor Design (LRFD) Bridge Design Manual and the MnDOT LRFD Bridge Design Manual (BDM). These specify general equations and procedures that are accepted practice, such as software and spreadsheets utilized by vendors and state highway officials for designing and load rating bridges. Additionally, hand calculations may be used to verify software and design basic components of the structures (AASHTO, 2017; MnDOT, 2020a).

2.2.1 Equivalent Width and Load Distribution

Slab-span bridge design splits the structure into equivalent longitudinal widths that are assumed to carry one lane of traffic considering single lane and multiple lane loading conditions. The equivalent width can be used to determine the amount of live load carried per one-foot width of slab. The MnDOT MBE (2020a) equation for single lane loaded equivalent strip widths is presented in Equation 2.4 and the equation for multiple lanes loaded is presented in Equation 2.5, both from AASHTO LRFD Bridge Design Specifications (2020) 4.6.2.3-1.

$$E = 10 + 5\sqrt{L_1 W_1} \qquad 2.4$$

$$E = 84 + 1.44\sqrt{L_1 W_1} \leq 12\frac{W}{NL} \qquad 2.5$$

Where *E* is the equivalent width (in.); L_1 in the modified span length (ft), taken as the smaller of the actual span length and 60 ft; W_1 is the modified bridge width (ft), taken as the minimum of the actual bridge width and 30 ft (AASHTO, 2020). The equivalent strip width calculated using Equation 2.4 has already been divided by 1.2 to account for the multiple presence effect. The multiple presence factor accounts for multiple trucks appearing on a structure simultaneously. For multilane loading, W_1 is the smaller of the actual bridge width or 60 ft, instead of 30 ft for single lane loading; *W* is the physical edge-to-edge width of the bridge (ft); *NL* is the number of lanes as specified in AASHTO Article 3.6.1.1.1 (2017). The resulting value of *E* (in.) is limited to 222 in. (18.5 ft) for the single lane loaded case in Equation 2.4 and 170 in. (14.2 ft) in the multilane loaded case in Equation 2.5.

With multiple lanes loaded, the equivalent strip width equation returns a smaller strip width than the single lane loaded equations depending on the size of the structure. This is because the multilane loaded case accounts for the fact that more load is spread out over the structure surface and the strips expected to carry the load are forced to become narrower.

Section 4.6.2.1.3 of the AASHTO LRFD Bridge Design Specifications (2017) also gives a different, simplified set of equations for cast-in-place concrete slab equivalent widths compared to those in AASHTO Section 4.6.2.1.3-1. These equations are applicable to slab bridges and concrete slabs spanning less than 15 ft. They differ for the positive moment (+M) and negative moment (−M) regions of the structure and offer an approximate value for the equivalent strip width.

$$\begin{aligned} +M&: \quad E = 26.0 + 6.6S \\ -M&: \quad E = 48.0 + 3.0S \end{aligned} \qquad 2.6$$

Where *E* is the equivalent width (in.) and *S* is the span length (ft). This set of equations is simplified in that it ignores the width of the roadway and structure; However, it requires information on positive and negative moment zones, which can further complicate the issue of determining equivalent strip widths.

In an effort to simplify the determination of strip widths for slab-span bridges, Amer et al. (1999) conducted research comparing values calculated using the AASHTO Standard Specifications for Highway Bridges (1992) and AASHTO LRFD Bridge Design Specifications (1994) equations to results from field observations and modeling using the grillage analogy method. The AASHTO LRFD equations differ from the AASHTO Standard equations in that they consider bridge width and the number of lanes. The grillage analogy method is used to find the distribution of moments in an assembly of beams representing the concrete slab. The equivalent strip width is taken from the plot of the moment distribution curve either from field tests or the grillage analysis. This study found that equivalent widths from the grillage method calculations ranged from 10 to 20% larger than values calculated with the AASHTO Standard and AASHTO LRFD methodologies. The researchers determined that the span length was the most critical parameter to consider when calculating the equivalent width and proposed an equation based on this conclusion. Equation 2.7 was proposed by the researchers to calculate the equivalent width for a slab-span bridge with or without edge beams. Edge beams are components that provide lateral confinement for the slab, defined as either a slab section with additional reinforcement, a beam integral with the slab and deeper than the slab, or a reinforced section of the slab integral with the curb.

$$E = 82.68 + 108.66L \leq 12\frac{W}{NL} \tag{2.7}$$

Where E is the equivalent width (in.); L is the length of the structure span (ft); W is the edge-to-edge width of the structure (ft); NL is the number of driving lanes on the structure. This equation can be multiplied by an edge beam factor C_{edge}, which is a function of the edge beam depth. While the slab-span structures in question for this MnDOT research project do not have edge beams, the concrete barriers may contribute to stiffness in a manner like edge beams. Results from Amer et al. (1999) also showed that the span width and slab thickness play a smaller role in determining the width that carries live load than do the span length of the structure. Edge beams provide a significant increase in maximum moments in bridges with these elements; however, they are not accounted for in Equations 2.4 through 2.7. In addition, the study noted that bridges with significant cracking may not exhibit the linear behavior expected by the existing models for equivalent width; in this case, field testing should be used to validate the calculated strip widths.

After determining the interior live load equivalent strip widths, the MnDOT LRFD BDM (2020a) specifies that the exterior live load strip width should be calculated. This section of the slab carries one wheel line and a tributary portion of the lane load. The AASHTO LRFD Bridge Design Specifications (2017) presents this equation in text as the “sum of the distance between the edge of the deck and the inside face of the barrier, plus 12.0 in., plus one-quarter of the strip width” … “but not exceeding either one-half the full strip width or 72.0 in.” (2017). The MnDOT LRFD BDM (2020a) includes that one quarter of the smallest strip width is added to the summation rather than just one quarter of the strip width. This expression is formalized as the following equation.

$$E = d_e + 12 + \left(\frac{E_{min}}{4}\right) \tag{2.8}$$

Where E is the equivalent exterior edge width (in.); d_e is the distance from the edge of the slab to the inside edge of the barrier (in.); E_{min} is the smallest interior equivalent width (in.). This completes the strip width calculations.

Equivalent width values are converted to a live load distribution factor (LLDF) to determine the portion of the live load from one lane of traffic that is estimated to be carried by a 1-ft strip of slab. For slab-span bridges, the LLDF is equal to the inverse of the equivalent width, *E*, converted to the units of feet as shown below.

$$\mathrm{LLDF} = {}^{12}/_{E} \qquad 2.9$$

2.2.1.1 Equivalent Width Origins

The equivalent width equations used by AASHTO were implemented based on recommendations from the research conducted by Zokaie et al. (1991a) for National Cooperative Highway Research Program (NCHRP) Project 12-26. The study was initiated in the 1980s to address two issues: (1) how to calculate wheel load distribution for the strength and serviceability analysis of highway bridges and (2) a lack of specifications for distribution factors to be used in design and evaluation. Zokaie et al. created a bridge database with average specifications for common bridge types such as slab-span, box girder, and beam. Each bridge type was evaluated in a finite element model while varying one parameter at a time to obtain wheel load distribution factors for shear and moment. Each parameter was assumed to be independent of the rest, which allowed for an exponential function to be developed of the type $a \cdot x^b$, where x is the value of the parameter and a and b are determined based on the variation of the parameter. The use of a limited set of bridge span lengths and aspect ratios resulted in equations in the code that failed to represent the variability of distribution factors based on bridge geometries that differed from those investigated in the study.

Zokaie et al. used three parameters to define a slab-span bridge: span length, bridge width, and slab thickness. Span length had the largest impact on the design distribution width *E*. The average bridge, with a span of 33 ft, width of 38 ft, and slab thickness of 17.7 in., had a multi-lane moment distribution width of 6.173 ft per lane and a single lane moment distribution width of 9.066 ft per lane. Zokaie et al. observed that the multi-lane moment distribution diverged significantly from the moment distribution calculated with the prior AASHTO equations as bridge span length increases. The same is true of the moment distribution of a slab-span bridge with multi-lane loading as bridge width increases. The results from Zokaie et al. (1991a) were recommended for adoption into the AASHTO LRFD Bridge Design Specifications. However, the equations developed by Zokaie et al. based on the average simply supported, single span slab-span bridge are not representative of all slab-span bridges.

Zokaie et al. (1991a) showed that curbs and parapets reduce the actual stresses in exterior girders while increasing the load they carry (i.e., greater load distribution). However, the actual effects are difficult to determine since these elements are often discontinuous and not adequately reinforced to carry tensile forces or distribute shear forces across the interface between the element and the deck. Few studies have sought to quantify load carrying capacity of secondary elements. To this end, studies such as Zokaie et al. reference secondary elements as likely sources of additional load carrying capacity when the AASHTO LRFD Bridge Design Specifications provide conservative estimates compared to results of field tests. Zokaie et al. evaluated several data sets of slab-span bridge field tests.

A bridge studied in Florida (Sessions, 1985) was instrumented with strain gauges to determine the wheel load distribution based on two-axle trucks at stationary positions on the bridges. Additionally, results from a structural analysis program were compared to the field test findings and results calculated using the AASHTO LRFD Bridge Design Specifications.

A quarter-scale three-span continuous slab-span bridge model in South Dakota (Iyer, 1985) was tested with a loading frame and electrical strain gauges. Moment distribution data were compared to several modeling techniques to determine which provided the best representation of the model bridge behavior. Of the models, a grillage model generated in the program CURVBRG gave the best results. Grillage models can be used to determine moment distribution design width factors, which are taken as the inverse of force per unit width. It is up to the engineer to decide what section properties and edge stiffening elements may be used in the model. For slab bridges, grillage model meshing cannot follow longitudinal girder lines since they are not present in the superstructure. Cracking also prevents the use of gross section properties.

Scrardelis et al. (1960) instrumented the Bacon Street bridge in San Francisco with 24 Carlson strain meters transversely across the centerline of the bridge. The bridge itself was a single simple-span slab-span structure designed for six traffic lanes with a 26-in. slab depth, 60-ft clear span, and 99.5-ft total width. The bridge was tested with a 15-ton truck. Results from an analytical investigation of the same bridge fit the experimental moment distribution results well except near the edges of the slab where a curb and guardrail were present; these features were neglected in the analysis software and the results were underestimated.

2.2.1.2 Equivalent Width from Field Data

Freeman and Vasconcelos (2018) reported on how the equivalent slab width impacts slab-span bridge load ratings. The first part of their study compared the load rating calculated using the load factor rating (LFR) method based on the discontinued AASHTO Standard Specifications (2002) to that calculated using the load and resistance factor rating (LRFR) (2018c) method based on the AASHTO LRFD Bridge Design Specifications (2017) while considering different bridge aspect ratios. The second portion involved field testing of five slab-span bridges.

In the initial comparison, the authors noted that bridges rated with the LFR method or with aspect ratios (length to width) less than two were more likely to be load restricted. In addition, 20.9% of bridges with parapets less than 10 ft wide were load restricted while only 4.5% of bridges with parapets greater than 10 ft wide were load restricted (six structures in the study had parapet widths greater than 10 ft). Surprisingly, the authors stated that updating bridge ratings from those calculated using LFR to those calculated using LRFR would increase the distribution factors by 12%, which would in turn decrease the average load rating of these bridges by 10.7%. In the second part of this study, Freeman and Vasconcelos (2018) compared load ratings of bridges in the Florida Department of Transportation (FDOT) inventory using the LFR method and a different Structural Analysis for Load Distribution (SALOD) method. The SALOD method uses a database of interaction surfaces found using the finite element method (Hays et al., 1986) and would decrease the distribution factor for bridges rated using the LFR method by 11% and increase the load rating by 13%. Freeman and Vasconcelos found that the equations provided in the AASHTO Standard Specifications and LRFD Specifications (AASHTO, 2002, 2017) result in values that were less conservative for equivalent width than the SALOD method; however, the strains obtained with the SALOD method were a closer fit to the data from the five field tests than the AASHTO equations. Generating ratings using the SALOD method resulted in 12.1% of the bridges having deficient ratings while generating ratings using the LFR method resulted in 18.4% of the bridges having deficient ratings; these trends were due to the increased equivalent strip widths determined using SALOD versus LFR. Freeman and Vasconcelos found that alternative procedures for determining equivalent widths may improve ratings of many structures. The authors concluded that the AASHTO Specifications (2017) produced conservative estimates for equivalent widths; however, most engineers rely on these for design and evaluation of slab-span bridges. The AASHTO specifications are suitable for design and rating, but some deficient ratings could be improved by using more refined methods of calculating load ratings.

Freeman and Vasconcelos presented the simple beam moment method and section modulus method for calculating the equivalent width using field strain data. These two methods are shown in Equation 2.10 and Equation 2.11, respectively.

$$E = \frac{M_b}{S \times \varepsilon \times E_c} \qquad 2.10$$

$$E = w \sum \frac{\varepsilon_i S_i}{\varepsilon_n S_n} \qquad 2.11$$

Where *E* is the equivalent width (in.), M_b is the simple beam moment (kip-in.), *S* is the section modulus (in.^{3}), ε is the peak strain (in./in.), E_c is the concrete modulus of elasticity, *w* is the width of the section for the section modulus method (in.^{3}), ε_i is the strain at the section for the section modulus method (in./in.), S_i is the section modulus (in.^{3}), ε_n is the strain at the point of interest (in./in.), and S_n is the section modulus at the point of interest (in.^{3}). The simple beam moment method uses the concrete modulus of elasticity, which is often underestimated and therefore can result in an equivalent width that is larger than the actual value. The section modulus method uses strain data from each location that strain is measured across the width of the slab, which can be more accurate than only considering the peak observed strain. The section modulus method also considers added stiffness from curbs or barriers that are not accounted for in the AASHTO equations.

Jones and Shenton (2012) investigated the equivalent width in concrete slab bridges in Delaware using strain data collected during load tests of six bridges. The authors selected their six bridges for testing in a manner that would provide an encompassing sample of the 250 slab span bridges in Delaware. A load test consisted of driving trucks across the bridge along different transverse paths after mounting strain transducers across the centerline of the bridge span.

Jones and Shenton (2012) defined the equivalent width as follows: the width that would have a uniform strain equal to the maximum strain but creates the same total effect as that caused by the actual strain distribution. Jones and Shenton determined equivalent width from measured strain values using Equation 2.12.

$$E = \frac{A_\varepsilon - A_t}{\varepsilon_{max}} + w_t \qquad 2.12$$

Where E is the equivalent width (in.), A_ε is the area under the strain curve (in.), A_t is the area under the strain curve between the truck wheel patches (in.), ε_{max} is the maximum measured strain (in./in.), w_t is the width of the truck (in.). The authors compared their measured equivalent widths to those found using the AASHTO formula and determined that the measured equivalent width was up to 116% greater than the AASHTO result for single lane loaded cases and up to 33% greater than the AASHTO result for multi-lane loaded cases.

2.3 LOAD TESTING

Load testing is a method of verifying the ability of a structure to safely carry a load. For bridges, this is especially important because failure can result in loss of life and destruction of property. Furthermore, load testing coupled with a finite element model (FEM) can be used to reduce costs associated with maintaining bridges and restrictions of legal loads. There are two categories of bridge load testing: proof and diagnostic. While each seeks to verify the load carrying capacity of a structure, the approaches to each category are significantly different. Proof load testing verifies the safety of a structure for a single given load. Modern proof load tests typically use a single static load calculated from the MBE that would translate to an equivalent load where the rating factor is equal to unity (AASHTO, 2018a). Proof load testing typically provides a more accurate representation of the capacity of a structure with less structural analysis regarding individual member capacities and maximum force effects (Alampalli et al., 2021). However, proof load testing is not used for reasons such as the increased risk, multi-step loading, and increased need for planning, knowledge, and expertise. While proof tests typically use one large load, diagnostic tests incorporate multiple smaller static or dynamic loads that would represent normal traffic loading. Diagnostic tests are frequently used to compare measured responses from the field to the responses predicted by an analytical model (Lantsoght, 2019). Some advantages of diagnostic testing are that it limits the possibility of damaging the structure due to inducing a demand larger than the structure can safely handle and that diagnostic testing can be accomplished with loads that are easier to manage and move. Both types of load testing have been used to understand the behavior of slab-span bridges.

Alampalli et al. (2021) summarized guidelines for completing load testing of bridges based on a review of in-place guidelines and procedures as well as practices currently used by bridge owners. In this state-of-practice document, the authors outline how load testing has transitioned from being used to convince the public of a bridge's safety to assessing bridge performance when traditional methods are not representative of the structural behavior. The authors state that the current provisions for load testing do not reflect the current state of the practice because the guidelines currently set out by the National Cooperative Highway Research Program (NCHRP) (1998) and Chapter 8 of the AASHTO MBE

(2016) are based on research conducted in the 1980s and 1990s. Since that time, communications, data sharing capabilities, FEMs, and data acquisition systems have changed and improved dramatically. Chapter 8 of the AAHSTO MBE allows for a new rating factor to be computed after comparing the maximum observed strain in a diagnostic test to the maximum expected strain. The new rating factor is computed by multiplying the current rating factor by an adjustment factor, *K*, which is based on the ratio of the measured and expected strain as well as additional factors pertaining to the test conditions and uncertainties. The authors did not elaborate on the additional factors that need to be considered when calculating the load rating from a diagnostic test or where in AASHTO they may be found.

There are nine applications for load testing identified by Alampalli et al.: developing field validated FEMs, evaluating effects of material damage, assessing bridges without plans, evaluating strengthening measures and retrofitting, analyzing heritage (historic) bridges, evaluating additional load carrying mechanisms, evaluating new materials, determining remaining fatigue life, and verifying design assumptions for new bridges. The authors present three reasons for using diagnostic load testing in the US based on a survey of 41 states: (1) re-evaluating the capacity of posted bridges, (2) evaluating new materials in service, and (3) evaluating structures without as-built plans. Based on the overall limited response in the US, the authors suggest that the NCHRP should be updated which may encourage more bridge owners to employ load testing.

The authors also discuss uncertainties and their effects on load rating and load testing. The first, structural reliability, considers uncertainties in the capacity stemming from design models, material properties, member fabrication, and construction. The second, demand uncertainties, pertains to vehicle weight and configuration, traffic speed, and road surfaces. These uncertainties are largely ignored by deterministic evaluation procedures such as allowable stress rating (ASR) and LFR. Load testing addresses the previously mentioned uncertainties and improves structural reliability by reducing uncertainties related to structural capacity. The authors show methods for determining cost savings and expenditures for a passed or failed load test. A passed load test can be used to determine a reduced probability of structural failure and thus an economic benefit can be calculated based on the reduced risk of failure.

Alampalli et al. (2021) suggest incorporating load testing into the life-cycle cost analysis for a bridge and even suggest installing permanent sensors for deflection, strain, and acceleration measurement. Since sensor and acquisition technologies have improved significantly, these could be used long-term without the need for set up and removal, which would allow for load tests to occur with significantly less effort. The authors state that load testing is 60% set up and 40% actual testing.

2.3.1 Load Testing Slab-span Bridges

Sessions (1985) used diagnostic testing to evaluate the load rating of slab-span bridges. A group of bridges in Florida were considered for load restrictions, although none exhibited visible signs of distress. A representative group were chosen for load testing. One structure was tested to determine if there was composite action between the original bridge deck slab and the concrete topping. Two additional three-span slab-span bridges were load tested to accurately determine the bridge capacity; strains were recorded on exposed reinforcing bars at six transverse locations across the 33-ft 3-in. wide bridge at the centerline of the middle span and one end span. In addition, a detailed crack survey was completed to characterize the moment-strain relationship of the reinforcing steel. The measured strains were significantly higher where cracking was observed. The relationship between bending moment and the reinforcing steel strain was established using the transformed area linear stress-strain relationships. Material properties were obtained for the concrete and steel reinforcement. Concrete compressive strengths were 4792, 6067, and 5411 psi for the three bridge decks compared to the 4000-psi design concrete compressive strength. The steel reinforcement modulus of elasticity was 28400, 27600, and 28300 ksi compared to the 29000-ksi design strength.

The authors calculated the design moments for 1-ft-wide strips of the slab-spans and compared them to the distribution factors and design moments determined using the SALOD analysis program. For bridge 930125, the SALOD program gave design moments that were 89% of those found using the AASHTO distribution factors. For the end span of bridge 930215, the SALOD design moment was 90% of the AASHTO moment. A finite element model was developed for each span of the two bridges. This model gave design moments that were between 65% and 70% of the AASHTO values.

Azizinamini and Choobineh (1995) developed models and methods for accurately determining the load carrying capacity slab-span bridges that were rated as insufficient. The researchers conducted both service (diagnostic) and ultimate (proof) load tests. The service load study utilized a variety of vehicle configurations and speeds and compared field results to both two-dimensional (2D) and three-dimensional (3D) finite element models. The results indicated that the 2D model calculated maximum moments as much as two times larger than the maximum moments from the 3D model. The reduced maximum moments found in the 3D analysis indicated that refined analyses can be used to quantify reserve capacity of slab-span structures. In addition, material samples were taken from a slab-span bridge to determine in-situ material properties. The structure was tested to collapse using eight hydraulic rams simulating two HS-20 trucks side-by-side with the front axles of the trucks already off the span. The structure was rated at 67% of an HS20-44, but the structure sustained a load equivalent to two rear axles of seven HS20-44 AASHTO trucks side-by-side on the bridge. The study attributed the extra capacity to using in-situ material properties of the reinforcing bars, accounting for the contribution of the barriers, and strain hardening of the reinforcing bars.

Old slab-span bridges have been frequently rated as deficient by transportation departments. Many of these structures were originally designed for small trucks, not modern traffic loads that have increased in size and volume. A study by Azizinamini et al. (1994c) investigated this issue; the authors tested six Nebraska slab-span bridges under service loads and two spans of a decommissioned bridge under ultimate loads. The bridges were designed for an HS15 truck load. In general, slab-span bridges often exhibit higher strength than predicted by design codes and standards; this is typically attributed to the development of membrane forces in the slab when deformation is prevented by restraints. This study tested each bridge four times with trucks travelling at crawling speeds across the structures. One test had two trucks travelling side-by-side and three tests used one truck positioned in either the left lane, straddling the roadway centerline, or the right lane. The study measured strains and deflections as the vehicles traveled the length of the bridges. The results were compared to a finite element model. Due to the cracked nature of the bridge decks, the observed strains differed significantly from those predicted by the model. However, the observed and predicted deflections correlated well and showed that local cracking in the tested structures had little impact on the overall performance of the structures. In addition to the six bridges tested under service loads, one structure was tested under ultimate loads using hydraulic rams to simulate different HS20 combinations. A simple span and a continuous span of the bridge were tested. The simple span was tested with 16 different load combinations before being loaded to collapse, and the continuous span was tested with 10 different combinations before being loaded to collapse. The test results showed that the continuous and simple spans had linear elastic behavior at the final test of 4.0-times and 3.6-times a HS20 truck load, respectively. The authors used yield line analyses that included the curb in the bridge deck cross section to obtain the ultimate capacity of the two spans tested to collapse. Using material properties obtained from the structure and moment curvature analysis, the analyses yielded ultimate capacities that compared well with the values obtained from field testing. Results indicated that the ultimate capacity of the bridges increased by as much as 28% with the inclusion of curbs in the analysis, showing that these nonstructural elements can provide a meaningful contribution to the load carrying capacity of the structure. In addition, the actual material properties of the steel reinforcing bars contributed to the increase in strength. This study showed that yield line analysis was an accurate and equivalent method for predicting the strength of slab-span bridges and identifying extra strength not accounted for in traditional analysis methods.

Various methods of diagnostic testing have been employed with similar results. Csagoly and Lybas (1989) tested slab-span bridges in Ontario and throughout the United States. In the Ontario study, 40 bridges were loaded to 100,000 lb using a tractor-trailer semi combination and a hydraulic jack. All but one of the bridges successfully carried the load. A secondary study investigating the span-to-thickness ratio compared to the ultimate capacity of deck slabs found that the slab strength increased as the ratio decreased. In addition, most slabs failed in punching shear.

Saraf (1998) conducted diagnostic testing of three slab-span bridges built in 1946, 1952, and 1966. All were continuous three-span structures. The tests used four dump trucks loaded so that the front axle weight was 9 kips and the rear axle weight was 20 kips. Truck positions were selected to induce maximum positive moments at midspan of the selected end span, midspan of the center span, and maximum negative moments at the support between the two spans. Saraf found that the equivalent strip equations from the AASHTO Standard Specifications (1992) were conservative. Results from the diagnostic testing and a FEA showed that bridge ratings for the three structures could be increased between 14 and 110%.

Jáuregui et al. (2010) conducted research on a slab-span bridge to find a more accurate equivalent strip width than the value found using Equations 2.4 and 2.5. The study included diagnostic testing and FEA. The diagnostic test included two dump trucks, one with a 10-kip front axle and 23.7-kip rear axle and one with a 14.7-kip front axle and a 38.2-kip rear axle. The trucks were driven across the structure in five load paths that covered the shoulders, driving lanes, and road centerline. In addition, the slab was evaluated in an FEM to compare results to the diagnostic test data. The authors found that the positive moment equivalent widths could be increased by 22% and the negative moment equivalent widths could be increased by 11%. These corresponded to an 11% (controlled by negative moment) increase in the bridge load rating.

Some tests on slab-girder bridges have relevance for slab-span bridge behavior. The Ontario Ministry of Transportation constructed reduced reinforcement slabs in the Conestogo River Bridge specifically for experimental testing and investigation of membrane action (Dorton et al., 1976). The Conestogo River Bridge is a three-span steel girder bridge with a composite concrete deck. The deck is 7.5-in. thick and longitudinally prestressed, resting on four girders spaced at 8 ft 8 in. The middle span is 145 ft, and the end spans are 114 ft. AASHTO (1973) required 1.0% reinforcing steel in bridge decks; this study varied the reinforcing steel from 0.95% down to 0.2% for three different slab thicknesses. Section C9.7.2.5 of AASHTO (2017) states that past research supports using a minimum of 0.2% reinforcement per layer of steel but uses a value of 0.3% in the empirical design procedure. The spans were monitored for strain, deflection, and load during static and dynamic live load testing. Two vehicles weighing 200 kips were used for the static tests and two vehicles weighing 95 kips were used for the dynamic tests. Static tests were performed in five lane locations across the width of the structure. The dynamic tests were conducted in two locations, one with a vehicle travelling down the center of the right lane and one with a vehicle straddling the centerline; these tests were conducted at incremental speeds of 10, 20, and 30 mph. In addition, impact tests were conducted with the test truck travelling at 10 mph over a 2 by 4 in. piece of timber placed in the path of the truck. In addition to the static and dynamic loads, test panels were constructed and tested for punching shear failure. In all but 2 of 32 test panels, the measured deflections were less than the expected deflections, which implied an additional stiffness of the slabs was not accounted for in the evaluation methods. The stress measured in the bottom layer of reinforcing steel was significantly lower than the expected values. The study concluded that advanced design methods for the deck slabs can be used to increase the load rating of the structure and employ higher flexibility of members. Furthermore, the study showed that arching action or membrane forces can be expected in two-way slab situations where the slab is confined by beams in the direction of loading.

Csagoly and Lybas (1989) referenced a study by Beal with the New York Department of Transportation that confirmed the results of the Ontario Department of Ministry and the Conestogo River Bridge, where bridge decks reinforced with isotropic mats can withstand a point load as much as six times the design wheel load plus impact. These results were also confirmed by Fang et al. (1986) who created a test bridge following the Ontario design method consisting of three girders and a 7.5-in. thick deck slab that was 49 ft by 20.5 ft. The slab was reinforced with two layers of reinforcement spaced at 8.75 in. in both directions and 4.375 in. in the top layer of reinforcement where the slab overhangs the edge girders. The researchers used 20.8 kips as a standard wheel load, which is the 16-kip maximum load induced by an HS20 truck multiplied by the AASHTO impact factor of 1.33. Fatigue tests were conducted with four hydraulic actuators spaced 6 ft apart transversely and 20 ft apart longitudinally, centered over the middle of the deck. The applied load, deflection, and strain were recorded during the test. The actual load testing consisted of loading all four actuators to 60 kips (which represented about three times the service live load of 20.8 kips), five million cycles of sinusoidal loading varying from 5 to 26 kips (which represented the service live load), and finally each actuator was loaded to 40 kips (which represented about two times the service live load). In this test, the slab-girder system performed satisfactorily compared to AASHTO standards. Fatigue and cracking from the load cycles did not appear to affect the stiffness of the slab as it continued to behave linearly. It was noted that membrane action, which is negligible until the deck begins to crack, may have been limited by deflections in the slab and lack of confinement on the edges of the slab.

2.3.2 Dynamic and Vibration Tests

Agardh (1994) used an impact device to excite a damaged concrete bridge for modal analysis and to validate an FEM technique. Measured input tests using an impact force are typically conducted for smaller bridges such as slab-span bridges, which was corroborated by Farrar et al. (1999) and Hsieh et al. (2006). This was accomplished by loading a concrete bridge to failure and monitoring modal properties through excitation during the process. The bridge was excited by dropping a 132-lb weight on the structure resulting in an impact force of 3.8 kips. Acceleration was measured at 27 points in three lines along the width of the deck. The acceleration data were used to identify mode shapes and resonant frequencies. Damage was achieved by loading the bridge with hydraulic jacks to induce bending cracks. The results of the study showed that the resonant frequency changed by as much as 8% as the bridge was incrementally damaged. This technique has been employed recently to monitor the health of bridges using vibration techniques including ambient and forced excitation (Hsieh et al., 2006). Hsieh et al. found that increasing damage to structures lowered the natural frequency while repairing and retrofitting the structure increased the natural frequency.

Hardyniec et al. (2009) evaluated dynamic testing guidelines through forced vibration testing and finite element modeling of a simple span highway bridge. The structure had a concrete deck on seven steel girders. The tests were conducted by striking the bridge deck with an impact hammer, which is a device used to induce vibrations caused by a known force at a known location. The force is measured by a force transducer or an accelerometer on the hammer with the force transducer providing the most accurate results. Impact hammers are low cost and easy to use, but they do not provide control over the exact frequency bandwidth and amplitude of the excitation force. The bridge was instrumented with nine PCB ±2 g accelerometers. The PCB impact hammer had a peak force of 5000 lbf and a frequency range of 0 to 500 Hz. The instruments were placed at locations that corresponded to nodes in the finite element model on the top of the bridge deck in rows parallel to the skew of the bridge. Excitation occurred at three locations on the bridge that were chosen away from the accelerometers and to highlight certain modes using the medium hardness hammer tip. This hammer tip produced a flat spectrum response for frequencies below 100 Hz, which were the target frequencies. Data were collected for four seconds after each impact and ten repetitions were conducted at each impact location. The time domain signals from the accelerometers were frequently checked for irregularities; when irregularities occurred, the test was either repeated or sensors were replaced.

The data collected were evaluated using frequency response function (FRF) inertance at each test location. FRF inertance refers to the force input and acceleration output matrix. The resulting plots were evaluated for peaks that correspond to natural frequencies. Natural frequencies and imaginary values of the FRF inertance were used to determine mode shapes. Hardyniec proposed that the mode shapes determined using dynamic testing with an impact hammer were adequate for bridge analysis and comparable to the mode shapes found using FEM techniques.

Important considerations for impact hammer testing included recording a single hammer impact per data set, which requires allowing the responses at all measurement locations to return to pre-test conditions. Impact hammer tips should not be changed between tests. It was also important to use a consistent impact magnitude, which can be difficult when the impact force is supplied by a person striking the bridge deck with the hammer. The type of hammer tip and the magnitude of applied force both affect the force spectrum and time pulse of the impact. Harder hammer tips have the least variability while softer tips have the most variability (Avitabile, 2017). Additionally, reference tests should be repeatable to within roughly 1 in. for large structures such as bridges. Another method for providing an impact load to a bridge involves driving a truck over a short ramp or a timber, as done for the Conestogo River Bridge tests (Dorton et al., 1976).

2.3.3 Considerations for Testing Cracked Structures

A significant stumbling block for determining suitable load ratings for a reinforced concrete structure is cracking. Cracked structures may no longer behave linearly, which may cause deviations from accepted models. Fenwick and Dickson (1989) tested 4-in. deep simply supported, flexurally-restrained, and fully-restrained concrete slabs under concentrated loads to investigate plate theory. The results of the study suggested that thin plate theory and elastic section analysis over-predict the peak flexural forces in the slab during loading. The study tested a simply supported slab that exhibited peak reinforcement forces that were 65% of the predicted values. For the flexurally-restrained slab, the measured forces were 50% of the predicted values. For the fully restrained slabs the measured forces were 35% of the predicted values. One reason that the slab resisted smaller forces than those predicted by thin plate theory in the restrained case was the development of membrane forces in the slab during loading. Other reasons for the lower-than-expected forces include a wider-than-expected distribution of flexural forces across the slab and residual tensile capacity of the concrete at the cracks. This could be relevant to cracked bridge decks and provide insight into their behavior.

2.4 FEM MODELING

AASHTO (2017) dictates parameters for computer modeling of bridge geometry. Concrete structures are modeled as elastic until the elastic limit, and inelastic behavior is assumed beyond that point. The MnDOT LRFD BDM (2020a) recommends using gross section properties or equivalent section properties for modeling. The same gross section properties should be used to determine loadings and deflections for design and bridge rating. MnDOT also recommends modeling redundant and non-prismatic structures with non-prismatic elements (MnDOT, 2020a). Various modeling techniques have been developed for bridge analysis and load rating and are accepted by the MBE (2018c) as modes of determining the load rating of a structure. The following section details studies in finite element modeling of bridge structures.

2.4.1 Field-Validated Modeling Techniques

Davids et al. (2013) investigated methods for load rating flat slab concrete bridges using finite element analysis. This study was in partnership with the Maine Department of Transportation (MaineDOT), which identified slab bridges as being high risk for having over-conservative load ratings. The authors cited several previous research papers noting that the AASHTO equivalent width method is conservative and results in many older bridges having weight restrictions or even facing closure. The AASHTO equivalent width (Equations 2.4 and 2.5) method for rating factors of slab bridges estimates the equivalent strip width for load distribution. The authors set out to develop finite element analysis tools that would streamline load rating specifically for flat slab bridges and compare results from the analysis tools to field data from live load testing. One bridge in Bradford, ME was chosen for field testing and 14 flat slab bridges were chosen to be load rated with the finite element analysis software developed in this study.

Davids et al. (2013) developed a software package called SlabRate for analyzing slab bridges in Matlab. This program was designed to test many load combinations and truck configurations. The program assumed the slabs were simply supported, limiting the programs applicability to simple span structures. All the structures analyzed in this study were single span structures. The authors conducted a convergence study on a 7.62 m wide, 7.16 m span bridge with the SlabRate program using mesh densities ranging from 20 x 20 elements to 50 x 50 elements. The program output compared well between the low- and high-density mesh with a 0.17% difference in bending moment at midspan between the two. In addition, the SlabRate output and ABAQUS output for a single three-axle truck placed at the location for peak moment differed by less than 0.5% for peak moment.

The bridge that was live load tested was instrumented with six strain transducers with 12-in. extensions. Five were installed at midspan and one was installed at a quarter point of the bridge. The bridge was loaded with two three-axle dump trucks provided by MaineDOT, which weighed 56.6 and 58.0 kips. Individual axle weights were estimated using known axle weights of other MaineDOT trucks used in previous studies. The study used a variety of truck positions and load cases with one and two trucks on the structure while strain data were collected. For each of the tests, the peak strain and corresponding truck position were recorded.

Davids et al. (2013) converted the strain data to live load moment using Equation 2.13 which was originally presented by Jáuregui et el. (2010).

$$M_{LL} = \varepsilon_{LL} E_c S \tag{2.13}$$

Where M_{LL} is the live load moment (k-in.), ε_{LL} is the measured live load strain, E_c is the concrete elastic modulus (ksi), and S is the bottom fiber section modulus of the composite reinforced concrete slab with steel transformed into an effective concrete area (in.^{3}). The conversion required an estimated section modulus that could either be cracked or uncracked. The cracked and uncracked section moduli were applied depending on the strain values at each sensor location. The authors compared the expected cracking moment to the live load moments derived from the strain data and found that the live load moment was 24% less than the cracking moment. To induce a moment equal to the cracking moment, the span would need to be loaded with two trucks that were 71% heavier than the AASHTO HL-93 design tandem.

The live load tested bridge was analyzed using SlabRate and a 32 x 24 element mesh density, which is a finer mesh than the convergence study required for sufficient accuracy. The edges of the slab in the model were thickened to account for the equivalent section of the curb and barrier present on the actual bridge. The model overpredicted live load moments by an average of 45% at all locations. The authors attributed the overprediction to taking the slab span from the centerline of each support rather than as the clear span, arching action of the slab at the abutments, and rotational restraint at the slab ends. Output was obtained from SlabRate with a constant slab thickness to observe the effects of the curb and barriers (modeled as the height of the barrier and the lowest rail of the barrier); the moment increased by as much as 28% for the load case with two trucks side by side. Davids et al. (2013) noted that the curb and barriers carried a significant portion of the bending moment since the model without the curb and barriers had increases in live load moment of 24% compared to the model with the curb and barriers.

The second part of this study involved load rating 14 slab bridges using SlabRate and AASHTO LRFD (2010) equivalent width method. The bridges were assumed to have the slab thickness specified on the construction plans and any wearing surface and stiffness contributions from curbs or barriers were neglected. The load rating from the SlabRate program ranged from 13.1 to 44.8% higher for the bridges modeled. The average load rating increase was 25.5% for the HL-93 design truck, 25.7% for the HL-93 design tandem, and 26.3% for the AASHTO notional load. The notional rating load is not a specific truck, but a grouping of axle configurations up to 80 kips that is expected to produce a worst-case scenario for simple span or continuous span bridges (AASHTO, 2018c). The authors presented their slab-span finite element model as an alternative rating system that was shown to improve the load rating for concrete flat slab bridges that was still conservative compared to field data. Some of the bridges modeled were skewed and these structures had higher increases in load rating than non-skewed bridges.

Azizinamini et. al (1994b) used both 2D and 3D analysis approaches to model the behavior of six bridges that were subjected to service load tests and one bridge that was subjected to an ultimate load test. The 2D analysis discretized the slab as 50 transverse frame elements along the length of each bridge. The 3D analysis followed the same slab element pattern with the addition of the curb as a 3D beam element. The analysis used 780 four-node elements, with 50 elements along the slab length and 15 along the slab width of each bridge; the degrees of freedom were in-plane translation and rotation at each node. A 3D beam element was used to model the 20 in. high curbs at the edges of the slab. Azizinamini et. al (1994b) also noted that many models idealize bridges as 2D structures and neglect the effects of non-structural elements, which is a source of conservatism. In the case of this study, the curb effects were considered and modeled as beam elements. The 2D and 3D models were loaded with four HS20 vehicle patterns: the first had two 50-kip trucks side-by-side, the second had 50-kip trucks in the left lane, the third had 50-kip trucks straddling the centerline, and the fourth had trucks in the right lane.

Results from the model included midspan deflections and midspan strains in the top and bottom of the slab. The model accounted for strains without cracking, thus the recorded strains in the top and bottom were the same. Field test data included higher strains in the bottom of the slabs, which was attributed to transverse cracking of the slab. However, the transverse cracking did not appear to affect the bridge response to live loading since the model and field test deflections matched. The predicted total load from the model and analysis was 3,852 kN compared to the value of 3,987 kN from the live load test. This indicated that the analysis parameters were a good fit to model of the bridge live load field test response.

The predicted and observed strength of the bridges reported by Azizinamini et. al (1994b) indicated that accepted methods of bridge evaluation such as those outlined in the MBE (2018c) do not account for all the factors that contribute to the strength of a structure. For example, many material properties specified at design differ from the actual properties of an in-situ structure, which can result in conservatism. Sources of additional strength identified by Azizinamini et. al (1994b) included strain hardening, material properties that are higher than design properties, and contribution from nonstructural elements; all these aspects are attributed to an increase in strength and load distribution in a structure and possibly allow for an increased load rating. This highlights the importance of determining actual values of material properties and validating calculations and models with results from field tests whenever possible.

Huria et al (1993) sought to standardize procedures for nonlinear finite element analysis (NLFEA) of concrete bridge structures. The authors noted that NLFEA provides insight into unexplained strength in reinforced concrete structures such as bridges that have been subject to ultimate load tests. The bridge in this study was a three-span slab-span bridge in Ohio. The project scope included describing the NLFEA software and a step-by-step process for modeling a slab-span structure, discuss parameters that affect bridge responses, conduct a sensitivity study of the bridge, and analyze results. A study by Shahrooz et al. (1994) noted that boundary conditions also play a significant role in the structural response in NLFEA, possibly to a higher degree than the materials properties.

The researchers modeled one half of the structure since it was observed that the adjacent half could be represented as a spring, which simplified the modeling process. The slab was modeled as reinforced concrete with nine-node shell elements, with springs at the centerline and abutment. The piers were modeled as beam-column elements with rigid ends since the researchers observed that the truck load response on the deck was not affected by flexibility in the soil-pile system. After discretization and mesh refinement, the final model had 66 nine-node elements. The nodes were all on the same plane of the element in rows and columns of three nodes at the middle height of the element. This facilitated modeling of membrane and bending rigidities. Important parameters that caused variance in the results included horizontal restraint and rotational stiffness at the abutments, concrete compressive strength, concrete tensile strength, tension-stiffening, and geometric nonlinearity. Results from the model without tension stiffening indicated that the flexural failure occurred at a load 20% less than the initial reference analysis. Similar differences are possible if concrete compressive strength and steel yield strength vary. The authors of this study noted that extensive parameter studies are not always applicable in civil engineering situations, which highlights the importance of knowing and focusing on critical responses. The authors of the study provided a description of the modelled bridge failure, which was ductile as it resulted from steel yielding. The yield line began at the outer edges of the slab and expanded to the wheel load.

Mabsout et al. (2004) analyzed 112 single span highway bridge case studies using FEA to determine maximum bending moments compared to AASHTO Standard Specifications for Highway Bridges (1996) and AASHTO LRFD Bridge Design Specifications (1998). The finite element program was a predeveloped 3D analysis model that assumed linear elastic elements. The modeled bridge slab included shoulders and confining elements such as edge beams and barriers. The study found that AASHTO (1996) and (1998) overestimated the maximum moment for single lane spans 25 ft or less but provided similar results to the FEA for single span structures with two or more lane and spans 35 ft or longer. The study also indicated that AASHTO overestimated bending moments for edge beams (typically 18 in. width) by as much as 20% for short spans 25 ft or less.

2.4.2 Natural Frequency and Vibration

Bagheri et al. (2017) investigated modeling of concrete bridges with high skew angles using the bridge frequency to identify the structural stiffness. As a baseline to begin the project, the researchers presented the equations below that relate the stiffness of concrete slab bridges without skew to the natural frequency and developed their models based on these.

$$\omega^2 = \frac{\lambda^2 * D}{\rho} \qquad 2.14$$

Where *ω* is the angular frequency; *ρ* is the mass per unit area of the plate (slab); *λ* is a coefficient depending on the plate dimensions and boundary conditions; and *D* is the bending stiffness of the plate as shown below.

$$D = \frac{E * t^3}{12 * (1 - v^2)} \qquad 2.15$$

Where *E* is the elastic modulus; *v* is the Poisson's ratio; *t* is the plate thickness.

The angular frequency can be determined by measuring the acceleration of the bridge in response to live load testing. The values for *ρ*, *t*, and υ can be determined from the structural geometry and material properties. Unfortunately, the study did not present the parameters for determining the value of *λ*; the authors stated that these are available in the literature. This value was not relevant to the study as the literature provides values for slab-span bridges without skew. The study determined *λ* for bridges with high skew values using a finite element model created and run in MATLAB. The value of *λ* increased as span length decreased since the natural frequency of the bridge increased; *λ* increased as skew angle increased since higher skew angles increase the stiffness and modal frequency of the bridge; increasing the slab thickness decreased the value *λ* as it changes the stiffness and barrier contributions.

The study of the plate dimension and boundary condition coefficient was used to predict the value of λ for a live load tested bridge. The researchers used a soft computing algorithm called an artificial neural network to model λ and apply it to a real structure. The slab-span structure modeled and tested by Bagheri et. al (2017) was War Branch Bridge in the State of Virginia. This is a slab-span bridge with a 45º skew that fit the purpose of the study. The authors instrumented one of the two spans of the bridge with accelerometers to measure vibrations from wind, normal traffic, an impact hammer, and a magnetic shaker. A variational mode decomposition (VMD) algorithm was used to decompose accelerations into modes for the structure. This principle was developed by Dragomiretskiy and Zosso (2014) to find a more exact mathematical model for empirical mode decomposition that had unknown limits and properties. The damping ratios were estimated from the modal response. The VMD can also be used to find the center of vibration of the structure from sub-signals decomposed from the acceleration measured in the structure. Two modal frequencies of 26.07 and 30.59 Hz were obtained from the structure. The damping ratios of 4.3 and 3.9% were close to the accepted value for concrete structures of 5%. Bagheri et al. (2017) used the structural characteristics and the experimentally-obtained modal frequency to determine a value of λ and then solve the frequency equation for stiffness, D, and then solve the stiffness equation for the elastic modulus, E. The elastic modulus could, in theory, be used to estimate the compressive strength of the concrete and the bending capacity of the structure, but the study did not present values for these. This approach could be used to validate the findings of live load testing as well as the results found through FEA. However, material properties can be determined from destructive compressive tests of the concrete and tensile tests of the steel present in the structure.

2.4.3 Material Properties

Material properties are important inputs for bridge models and load ratings. These properties can be assumed based on as-built plans, taken from design codes, or determined experimentally through sampling or other non-destructive techniques. Investigating the actual material properties of a structure may yield new insight into the expected behavior of a structure and even explain unexpected behavior documented in field tests. However, even with sampling, uncertainty will exist in the effective material properties, especially for older structures (Huria et al., 1993).

Actual material properties provide the most accurate representation of a structure and should be considered the preferred values used in analysis and load rating. However, Russian et. al (2020) noted that some concrete structures have material properties that do not match as-built plans or the minimum properties specified by design and evaluation codes. The AASHTO MBE (2018c) provides minimum values based on the age of the structure since more accurate values are difficult to obtain. The provided values are conservative (f'_c of 2.5 ksi prior to 1959 and 3 ksi after 1959), which could in turn result in a reduced bridge load rating. The study by Russian et al. (2020) sought higher-than-expected material strength in pre-1959 Texas bridges. This was accomplished using a statistical analysis approach in which material property data were placed in groups based on property, material, and age. The authors used a normal distribution curve with a 95% confidence interval to determine the necessary sample size for each group. More than 6,500 individual tests were documented from the Texas DOT archives. To address the issue of different steel grades existing in each group of steel tests, the researchers used a mixture density probability function that allowed for analysis of sub-populations within each group.

Russian et al. (2020) found that some material properties were likely to be statistically higher than those presented by the MBE or similar codes. The 5th percentile yield strength of reinforcing bars in the group of steel before 1936 and the group of steel bars between 1936 and 1963 in the study were 40% and 6% higher than the AASHTO MBE values, respectively. However, for structural steel (not reinforcing bars) from before 1936, the yield strength was found to be lower than the MBE value while steel from after 1936 had a higher strength. The study notes that there was not a requirement for yield strength in structural steel prior to 1936, which accounts for the lower-than-expected values.

In addition to historic data, steel samples were taken from decommissioned bridges in the Texas inventory. From the seven structures sampled, none of the reinforcing steel yield strengths were less than the statistical analysis values. The study proposed a 40% increase in the expected steel yield stress, from 30 to 42 ksi for bridges built prior to 1954, which could impact load ratings of structures in the Texas highway system. For bridges built after 1954, the study found that the guidelines could potentially be increased by 6% for steel yield stress, which may not be worthwhile as this is a small increase.

Concrete compressive test results were also compiled by Russian et al. (2020). This was accomplished with a single group for statistical analysis. The FHWA National Bridge Inventory (2018) recommends a value of 2.47 ksi for concrete compressive strength in structures with unknown material properties. However, from the statistical analysis in this study, a new value of 3.05 ksi was proposed, which would be a 20% increase in compressive strength. This value was based on a Weibull distribution and the 5th percentile of 2,370 compressive tests of concrete cylinders. An increase in compressive strength likely would have a smaller impact on bridge ratings than increasing steel yield stress; however, the finding is still significant. This study was specific to Texas, but the approach could be applied elsewhere.

2.5 SUMMARY OF LITERATURE REVIEW

The literature review summarizes relevant slab-span bridge evaluation manuals, analysis techniques, and previous research. Previous research showed that the assumed material properties and methodologies used for design and evaluation of bridges are conservative. While conservative design assumptions ensure public safety, their use in the capacity evaluation for load rating can hinder freight traffic and funnel OSOW vehicles onto smaller roads when bridge ratings are overly conservative.

State DOTs are required to follow the AASHTO LRFD Bridge Design Specifications (2017) for design of new structures, and they are permitted to evaluate and modify existing structures with the codes and specifications used in the original design (Densmore, 2000). The MnDOT Bridge Office (2020) made amendments to the AASHTO LRFD Bridge Design Specifications and uses these for design of new structures. The MnDOT LRFD BDM (2020) defines the equations used to determine the equivalent strip width, which is the width of slab that carries one lane of concentrated wheel loads. This width is an important component used to determine the maximum moment induced by a given truck configuration. The equations for calculating equivalent strip widths based on research conducted in the 1980s (Zokaie et al., 1991a) have been shown to be overly conservative through load testing and finite element modeling (Amer et al., 1999; Freeman & Vasconcelos, 2018; Jáuregui et al., 2010; Saraf, 1998). Identifying more accurate equivalent strip widths may increase a bridge load rating. For example, Jáuregui et al. (2010) used diagnostic load testing and finite element modeling to increase a slab-span bridge equivalent strip width by 11% and load rating by 11%. Fenwick and Dickson (1989) observed that flexural forces were more distributed across the slab width than anticipated, which resulted in reinforcement stress that were 65% of those expected. Additional investigations into equivalent width determination for slab-span bridges from field testing have been conducted, resulting in improved load ratings (Freeman & Vasconcelos, 2018; Jones et al., 2012).

In addition to static testing, dynamic impact testing has been shown to provide insight into bridge structural health and to be a useful method for validating FEMs (Davids et al., 2013; Farrar et al., 1999; Hardyniec et al., 2009; Hsieh et al., 2006). Mode shapes and natural frequencies obtained from the field can be used to update FEMs and identify structural stiffness and damping ratios (Bagheri et al., 2017).

Many studies described in the literature indicate that bridge performance is often better than analytical theory suggests (Azizinamini et al., 1994a, 1994b; Azizinamini et al., 1994; Azizinamini & Choobineh, 1995; Csagoly & Lybas, 1989; Mabsout et al., 2004; Saraf, 1998). In-situ bridge material properties are often higher than the values specified in as-built plans and accepted values stated in evaluation manuals (Huria et al., 1993; Russian et al., 2020). Azizinamini et al. (1994) and Freeman and Vasconcelos (2018) noted that more live load is distributed to the slab-span bridge barriers than is expected. In addition, members such as edge beams or barriers restrain the slab, which can create membrane forces that are not accounted for in standard evaluation methods (Dorton et al., 1976).

When structures have load ratings less than unity, diagnostic load testing and finite element analysis can be used to improve the load rating or determine a more accurate structural response to loading (Azizinamini et al., 1994b; Huria et al., 1993; Mabsout et al., 2004). MnDOT (2018) states that bridges may be load rated using data from field live load testing (e.g., diagnostic tests) if the performance of the bridge is expected to be more favorable than analytical theory. To this end, there is a wealth of information in the literature that supports calculating bridge capacity using field testing data (e.g., strains, displacements, or acceleration). However, transverse and longitudinal cracking on a slab-span bridge can make collecting quality data from strain gauges and displacement transducers challenging. Furthermore, using this data to validate a FEM technique for quantifying behavior is similarly difficult. For example, Huria et al. (1993) indicated that modeling of the support conditions significantly affected the predicted response. Shahrooz et al. (1994) corroborated these modeling results and noted that model parameters describing the boundary conditions were more critical than material property parameters.

The available slab-span research provides background and guidance for future evaluation of such structures. Diagnostic testing coupled with finite element modeling can provide an accurate representation of the behavior of slab-span structures and can be used to evaluate the load rating of a bridge. Experimental field test data and analytical results from investigating slab-span structures should be compared to AASHTO Specifications to determine if changes to structural ratings are feasible. Results and data in the literatures indicate that load ratings may be improved using alternative rating methods.

CHAPTER 3: FIELD TESTS

3.1 FIELD BRIDGE DESCRIPTIONS

In this study, Bridge 27926 was selected as the primary structure for modeling and live load testing. Bridge 27926 was instrumented and tested the weekend of 6/5/2021 – 6/6/2021. A secondary structure, Bridge 27925, was also instrumented and tested on 6/12/2021 – 6/13/2021 because I-94 and I-694 were closed due to a reconstruction project on nearby Highway 100. This meant that no vehicular traffic was on the bridges during testing. Full closure of the structures allowed for more tests to be conducted across the width of the bridges without interruption.

The as-built plans for Bridge 27926 are shown in Figure 3.1 and Figure 3.2. The as-built plans for Bridge 27925 are shown in Figure 3.3 and Figure 3.4. In both structures, the concrete slab is reinforced by steel bars in both directions in both the top and bottom of the slab. For typical slab-span bridges with epoxy-coated reinforcing bars, the minimum clear cover to the top of the bridge slab is 3 in. and the minimum clear cover to the bottom of the slab is 1.5 in. Figure 3.5 shows the elevation view for Bridge 27909, which is typical of slab-span bridges and representative of Bridges 27925 and 27926. Bridge 27909 and Bridge 27925 were designed with identical specifications. The arrangement of a slab-span bridge is simple in that the slab rests on concrete piers supported by pilings. Additional reinforcement is shown connecting the slab and pier caps together with 90-degree hooks in Figure 3.6. The concrete barriers are also anchored to the concrete slab with reinforcing bars. Of all three structures, Bridge 27925 was in the worst condition with the most cracking. This conclusion was drawn based on the 2019 inspection reports (Dumbeck, 2019a, 2019b, 2019c), which indicate that Bridge 27925 has the lowest sufficiency rating of 68.7 while Bridge 27926 and Bridge 27909 have sufficiency ratings of 69.7 and 69.6 respectively.

3.2 PRIMARY BRIDGE IN-SITU MATERIAL PROPERTIES

A MnDOT crew obtained 12 concrete core samples from the slab of Bridge 27926 between November 5, 2020, and November 24, 2020, in accordance with American Society for Testing and Materials (ASTM) International (2020b) and AASHTO (2018) procedures. Six 1.75-in. diameter cores were obtained from the slab and barrier. Three 4-in. diameter cores and three 6-in. diameter cores were also obtained from the slab. The exact coring locations were adjusted as drilling progressed such that the cores did or did not include steel reinforcement. Cores that did not contain steel reinforcement were used to quantify concrete material properties and cores that did purposefully contain steel reinforcement were dismantled so that the segment of steel reinforcement could be used to quantify steel material properties. The following in-situ material properties were quantified:

- Compressive strength (f'_c) of the slab and barrier concrete
- Modulus of elasticity (E_c) of the slab concrete
- Yield strength (f_y) of the steel reinforcement in the slab

- Modulus of elasticity (E_s) of the steel reinforcement in the slab

The 1.75-in. and 4-in. diameter cores were collected to obtain concrete material properties for the slab and barrier. Three of the 1.75-in. diameter cores did not hit rebar. Only one of the 4-in. diameter cores did not hit rebar and met the length-to-diameter (*L*/*D*) ratio requirements of ASTM C42 (2018) to conduct the modulus of elasticity test. Rebar spacing differed enough from the as-built plans that it was not practical to obtain more 4-in. samples that did not contain rebar. The 1.75-in. and 4-in. diameter cores were cut to a height between 1.0 and 2.1 times the diameter (*D*) and tested to characterize the compressive strength in accordance with ASTM C39 (2020a). Samples tested for compressive strength with an *L/D* ratio less than 1.75 were adjusted with the correction factors given in ASTM C42 (2018). In addition, the concrete modulus of elasticity was determined in accordance with ASTM C469 (2014) using three separate trials on the single 4-in. diameter core that did not contain rebar. A photo of the sample tested for modulus of elasticity is shown in Appendix B. Results from the compressive strength and modulus of elasticity testing are shown in Table 3.1. The design compressive strength of the concrete slab was 4000 psi. However, generally the properties specified in the plans do not always match the actual material properties in the field since concrete gains strength over time, often with a lower bound of 20% strength gain (French et al., 2010; Russian et al., 2020; Wood, 1992). For Bridge 27926, the in-situ compressive strength of the slab and barrier concretes were 9480 psi and 11025 psi, respectively. Both values were significantly higher than the design value, even considering a 20% strength increase over time (equal to 4800 psi).

Concrete with a design compressive strength of 4000 psi would be expected to have a modulus of elasticity of approximately 3600 ksi using the equation from the AASHTO LRFD Bridge Design Specifications (2020) below.

$$E_c = 33{,}000 K_1 w_c^{1.5} \left(f_c^{'}\right)^{0.5} \tag{3.1}$$

Where E_c is the concrete modulus of elasticity (ksi), K_1 is the correction factor for the source of aggregate (taken as 1.0), w_c is the unit weight of concrete (kcf), which was taken as 145 lb/ft^3, and f'_c is the compressive strength of concrete (ksi). The measured material properties for concrete compressive strength were more than twice the design values. However, the measured value for modulus of elasticity was 3725 ksi, which was only 2.4% higher than the expected value based on the design material properties and AASHTO Equation C5.4.2.4-2 (2017).

The 6-in. diameter cores were collected to obtain rebar samples for characterizing steel properties. Four epoxy-coated rebar samples ranging in length from 4 to 5.5 in. were obtained from the three 6-in. cores. Three of the reinforcement samples were No. 7 bars and one was a No. 5 bar. The No. 7 samples were machined to 0.5-in. diameter test coupons and the No. 5 sample was machined to a 0.35-in. diameter test coupon per ASTM 370 (2019). A photo showing a sample reinforcement bar fixed in the tension-testing machine and a figure depicting the final coupon specimen dimensions are included in Appendix B. The coupons were tested in tension to determine the yield strength per the 0.2% offset method and the modulus of elasticity per ASTM 370. The data from testing the No. 5 bar were excluded from the results due to a malfunctioning sensor. Table 3.2 and Figure 3.7 show results from the tensile tests conducted on the three No. 7 steel reinforcement specimens. The extensometer was removed prematurely while testing specimen C2; thus, data beyond the linear region were not captured for determining the yield strength of this specimen. The steel reinforcing design yield strength was 60 ksi and the design modulus of elasticity was 29000 ksi. However, results in Table 3.2 indicated that the measured in-situ reinforcing steel yield strength was 80.4 ksi and the modulus of elasticity was 29,800 ksi.

3.3 FIELD TEST INSTRUMENTATION

Field testing plans for Bridge 27926 and 27925 were developed considering previous diagnostic testing studies. The instrumentation locations were selected based on the expected results from a preliminary elastic finite element model and influence line analysis. Overall instrumentation plans for Bridge 27926 and Bridge 27925 are presented in Figure 3.8 and Figure 3.9, respectively. The instrumentation suite included the following sensors that captured the following behavioral data: accelerometers to capture acceleration, linear variable differential transformers (LVDTs) to capture displacement, uniaxial tiltmeters to capture rotation, and strain gauges with a 1-ft gauge length extension to capture changes in strain.

3.3.1 Acceleration

Based on initial finite element models, expected frequencies in Bridge 27926 ranged from 23 to 27 Hz for the first set of three modes and 31 to 33 Hz for the second set of three modes. Twelve PCB 333B30 accelerometers with a range of ±50 g and an effective frequency range from 0.5 to 3000 Hz were sampled by a National Instruments NI-9234 IEPE 4-Channel Input Module, connected into a NI CDAQ-9179 CompactDAQ 14-slot Chassis. The input module was capable of a 51.2 kHz sampling rate. During field testing, the accelerometers were sampled at a rate of 25,600 Hz, which was roughly 1,000 times the expected frequencies; this high sample rate allowed data to be decimated after collection, thus reducing noise, and still be significantly higher frequency than the structural modes of interest. The identified modal frequencies and mode shapes were used to validate the finite element modeling technique and to gather information on the bridge stiffness and boundary conditions. The accelerometers were affixed to the underside of the slab using an epoxy adhesive and plastic mounting tabs, which allowed the accelerometers to be easily removed after testing was completed. During dynamic tests on Bridge 27926, accelerometer 69544 malfunctioned and did not provide useful output. A PCB Piezotronics model 086D50 impact hammer (measurement range ±5000 lbf) was used to excite the bridge; instrumentation in the hammer collected the force delivered to the slab when generating a dynamic response. The bridge was excited ten times directly above each sensor while gathering acceleration data. The accelerometer locations shown in Figure 3.8 for Bridge 27926 were selected to capture the three primary mode shapes (shapes one through three) identified using the initial finite element model. A more detailed drawing showing only the accelerometers is provided in Figure 3.10 for Bridge 27926 and Figure 3.11 for Bridge 27925. Figure 3.12 shows an accelerometer affixed to the bottom of the slab on Bridge 27926.

3.3.2 Rotation

Uniaxial tiltmeters from Bridge Diagnostics, Inc. (BDI) (model T500-005) were placed in six locations focused on the Northwest corner of Bridge 27926. The locations are shown in Figure 3.13. An example of a tiltmeter affixed to the bottom of the slab is shown in Figure 3.14. The tiltmeters had a range of ±5°. The data obtained from the tiltmeters were used to validate results from the FEMs and to corroborate displacement data. The tiltmeters were placed to measure rotations in the direction of traffic near the West abutment and the West side of the West pier. Additionally, two tiltmeters were placed at midspan of the West span measuring rotation perpendicular to the direction of traffic; one sensor was placed directly under the barrier and one sensor was placed several feet away from the barrier (transversely) to characterize the influence of the barriers on deck rotation. No tiltmeters were placed on Bridge 27925, which was the secondary structure.

3.3.3 Displacement

Fifteen BDI LVDTs (model LVDT-01-020) were placed at various locations on Bridge 27926 as shown in Figure 3.8. A more detailed drawing showing only the displacement sensors is provided in Figure 3.15. These sensors were placed at midspan of the East and West spans near and away from the barrier, with five sensors on the West span at variable spacing to capture displacement directly beneath the truck positions and 10 sensors at 3-ft 10-in. spacing on the East span to characterize the transverse load distribution and the effects of the barriers. The LVDT sensors could capture up to 2 in. of displacement, but the expected displacements based on initial finite element models only ranged from 0.01 to 0.07 in., which was within the resolution of the LVDTs. The LVDTs were set up on camera-style tripods beneath the bridge as shown in Figure 3.16. The displacement data were used to validate the FEM and corroborate load distribution data obtained from strain measurements. The literature indicates that displacement sensors could be the best option for validating the finite element model (Azizinamini et al., 1994; Azizinamini & Choobineh, 1995; Huria et al., 1993; Shahrooz et al., 1994).

A parametric study using Ansys Static Structural software was conducted to determine how the load distribution varied when using strain versus displacement data. The results of the study indicated that the displacement data collected transversely across a loaded span (same array as strain gauges) should exhibit the same load distribution behavior as that expected when using strain data. The parametric study is discussed in more depth in Appendix C.

3.3.4 Strain

The instrumentation plan also included 15 BDI ST350 strain gauges. The strain gauges had a ±4000 με range and were installed with a gauge length of 12 in. as shown in Figure 3.17. Aluminum strain gauge extensions were used to minimize the effects of local cracking in the concrete. The 12-in. extension length was shown to be adequate in the literature (Jones et al., 2012). Use of a strain gauge extension meant that the recorded strains were amplified by the integer multiple of the gauge length. The standard gauge length was 3 in., which meant that the magnitude of each strain measurement was divided by four to determine the correct averaged strain. Additionally, BDI specified that a factor of 1.1

should be applied to the magnitude of each strain measurement to account for the extension effect. The strain gauges were placed according to the instrumentation plan with slight variations to avoid spalled and cracked areas. Locations were marked using tape measures, chalk lines, and marker pens. The gauges and extensions were mounted to the bridge using aluminum mounting tabs, Loctite 410 instant adhesive, and Loctite 7452 accelerator. These sensors were used to determine the transverse load distribution in the structure. Results and methods in the literature show that the equivalent strip width can be obtained from strain data (Freeman & Vasconcelos, 2018; Hays et al., 1986; Jáuregui et al., 2010; Jones et al., 2012; Sessions, 1985; Zokaie et al., 1991a) or from displacement data (Crabtree et al., 2021) for slab-span bridges.

3.4 FIELD TEST LOADING

Separate testing plans were developed for each bridge. The detailed plans showing the order and location of each test are provided in Appendix D. The typical live load testing procedure included taking measurements without trucks on the bridge as a set of zero-reading measurements, followed by several static truck tests in which trucks were parked at a specific location while data were collected. This process was repeated until all static tests were complete.

3.4.1 Primary Bridge 27926

A total of 53 static truck tests were conducted on Bridge 27926, including tests when trucks were positioned 1 ft away from the barrier, 4.5 ft away from the barrier, 8 ft away from the barrier, and at the centerline of the structure as shown in Figure 3.18 and Figure 3.19. Exact truck positions from each test are detailed in Appendix E and photographs from testing and instrumentation are shown in Appendix F. Truck dimensions and axle weights are shown in Table 3.3. Of the 53 tests, 41 were single truck tests (Figure 3.20), three tests included two trucks side-by-side (Figure 3.21), and nine tests included two trucks back-to-back (Figure 3.22). Dynamic truck testing included four tests where one truck crossed the bridge at the posted speed limit. Dynamic impact hammer testing was conducted at 12 locations, and 10 impact hammer strikes were imparted on the slab at each of the locations.

3.4.2 Secondary Bridge 27925

A total of 36 static truck tests were conducted on Bridge 27925, including tests 1 ft from the barrier, 7 ft from the barrier, 15 ft from the barrier, 23 ft from the barrier, and at centerline as shown in Figure 3.23, Figure 3.24, and Figure 3.25. Exact truck positions from each test are detailed in Appendix G and photographs from testing and instrumentation are shown in Appendix H. Truck dimensions and axle weights are shown in Table 3.4. Of the 36 tests, 23 were single truck tests, eight were two trucks back-to-back, and five were two trucks side-by-side. Dynamic impact hammer testing was conducted at 13 locations, and 10 impact hammer strikes were imparted on the slab at each of the locations.

3.5 FIELD TEST DATA PROCESSING

3.5.1 Static Data Processing

Data taken from the field test on Bridge 27926 was separated into “zero-reading measurement” files and “test” files. The zero-reading measurement files contained data measured from the instrumentation suite without a load placed on the bridge. Throughout the day, the air temperature and the slab temperature increased, which resulted in a general increase in strain observed in zero-reading measurement file data. Zero-reading measurements were taken prior to positioning the first truck on the bridge in the morning, periodically throughout the course of the testing day, and at the end of testing. Readings from each instrument at each zero plotted against temperature are shown in Appendix I. To account for temperature variation while analyzing the test data, the average value taken from the zero-reading measurement file just before or after a static test was used to plot a linear line between the points. The zero-reading measurements assigned to each individual truck test were selected using a time-based linear interpolation between the zero-readings immediately before and after any given truck load test.

During any single truck test, individual sensor readings changed slightly over the course of the minute-long test due to sensor drift or continued movement of the bridge toward equilibrium with a truck parked on top. This behavior was eliminated from the field data by removing the gradient, which resulted in an average initial sensor value that was representative of the immediate change in response due to the application of the truck loading. Two examples of sensor drift and the corrected value, from a strain gauge and an LVDT, are shown in Figure 3.26. The field data that were processed for sensor drift and corrected for temperature effects were used to validate the computer modeling techniques and determine equivalent widths.

3.5.2 Dynamic Data Processing

Because the input (impact hammer force) and output (acceleration) were measured, the data could be evaluated using an input-output system identification technique. Cross-correlation of the data was conducted using the input at one sensor and the responses at the other sensors. The cross-correlations were analyzed using the eigensystem realization algorithm (ERA) (Juang & Pappa, 1985) in MATLAB. The ERA returns identified natural frequencies and structural mode shapes. Mode shapes and frequencies were selected from the field data considering the energy-based modal assurance criterion (EMAC) values (Allemang, 2003; Pastor et al., 2012). EMAC values greater than 0.7 were selected because an EMAC close to unity indicates perfect consistency between time and space. The EMAC values were used to select mode shapes from the field data for comparison to the FEM.

Table 3.1 Results from concrete compressive strength and modulus of elasticity testing.

Core Location	Core Diameter, *D* (in.)	Core Length, *L* (in.)	*L/D*	Compressive Strength, f'_c (psi)	Correction Factor	Adjusted Compressive Strength, f'_c (psi)	Modulus of Elasticity, E_c (ksi)
Slab	4.00	5.14	1.29	10460	0.93	9770	----
	3.99	4.61	1.16	10380	0.91	9540	----
	4.00	7.90	1.97	9150	n/a	9150	3600
							3800
							3770
					Average:	*9480*	*3725*
Barrier	1.73	3.44	1.99	12370	n/a	12370	----
	1.73	3.53	2.04	9680	n/a	9680	----
					Average:	*11025*	----

Table 3.2 Results from steel reinforcement tensile testing.

Steel Location	Specimen Name in Figure 3.7	Reinforcement Size (No.)	Coupon Diameter (in.)	Yield Strength, f_y (psi)	Modulus of Elasticity, E_s (ksi)
Slab	C2	7	0.5	n/a	29500
	C3-1	7	0.5	83300	29700
	C3-2	7	0.5	77400	30200
			Average:	*80400*	*29800*

Table 3.3: MnDOT truck axle spacing and weight from the Bridge 27926 field test.

Truck Number	Distance from Front Axle to First Tandem (in.)	Distance Between Tandem Axles (in.)	Width (in.)	Front Axle Weight (kips)	First Tandem Weight (kips)	Rear Tandem Weight (kips)	Total Weight (kips)
215556	187	54	96	15.6	17.2	16.8	49.6
214579	183	55	96	15.9	17.1	16.9	49.9

Table 3.4: MnDOT truck axle spacing and weight from the Bridge 27925 field test.

Truck Number	Distance from Front Axle to First Tandem (in.)	Distance Between Tandem Axles (in.)	Width (in.)	Front Axle Weight (kips)	First Tandem Weight (kips)	Rear Tandem Weight (kips)	Total Weight (kips)
215556	187	54	96	15.4	17.3	17.1	49.8
214579	183	55	96	15.2	17.1	16.7	49.0

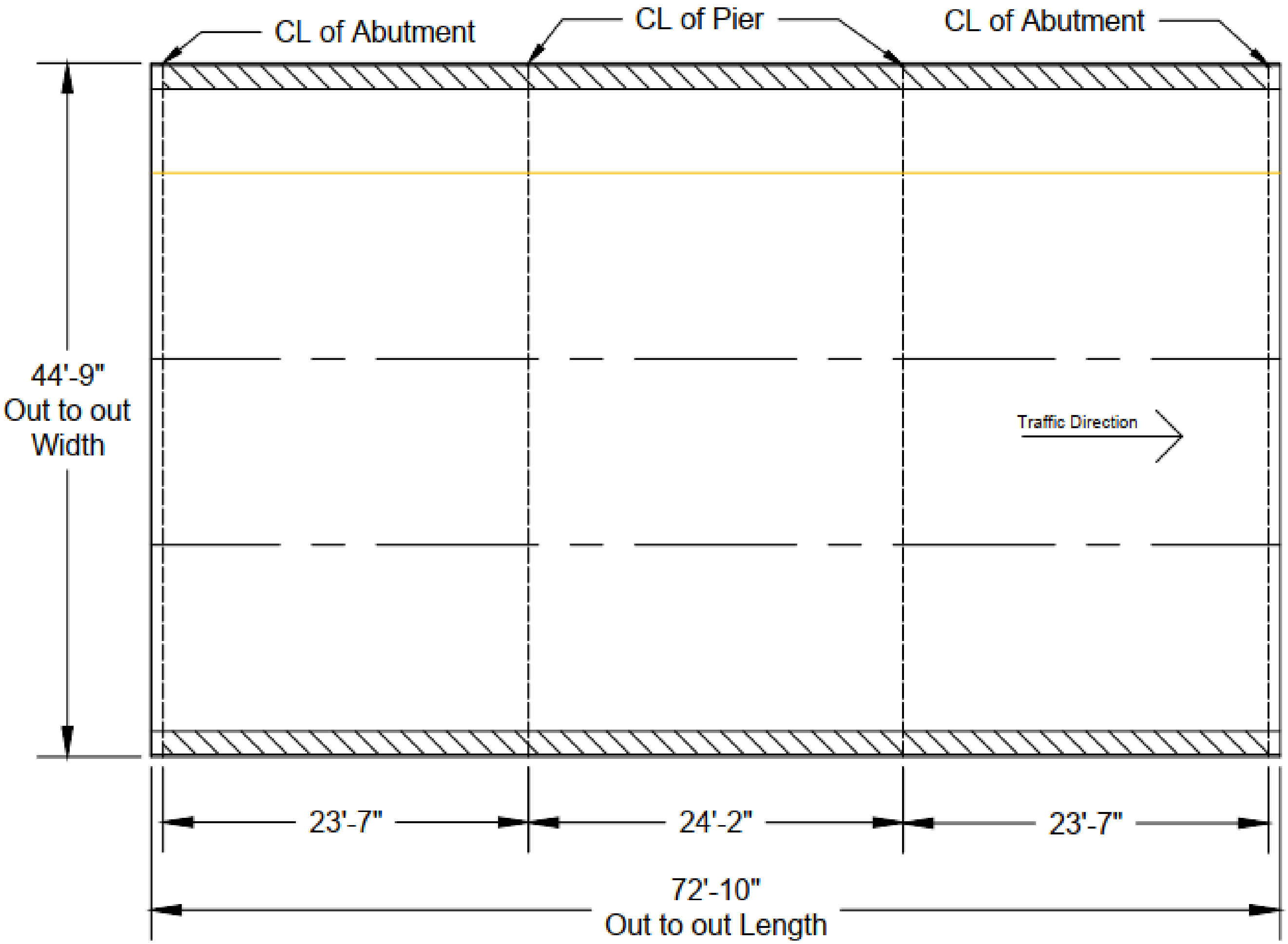

Figure 3.1: Plan view of the primary slab-span bridge (Bridge 27926).

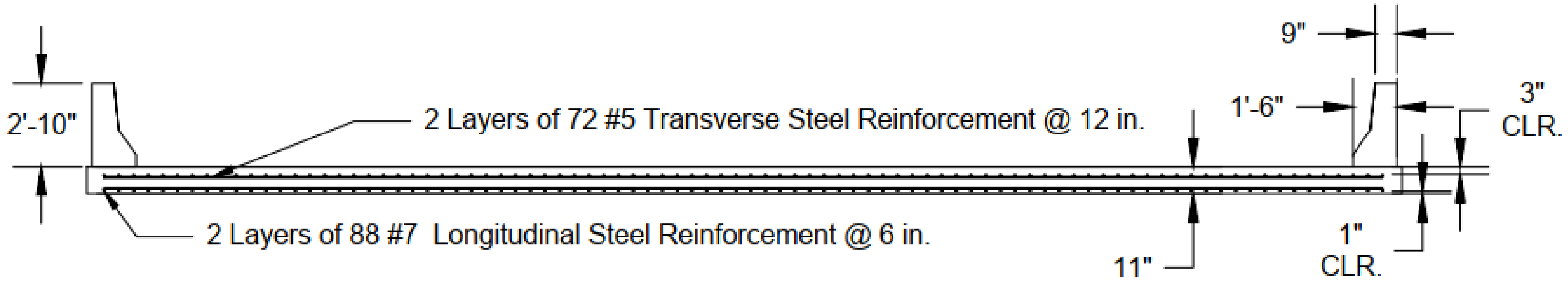

Figure 3.2: Cross-sectional view of the primary slab-span bridge (Bridge 27926).

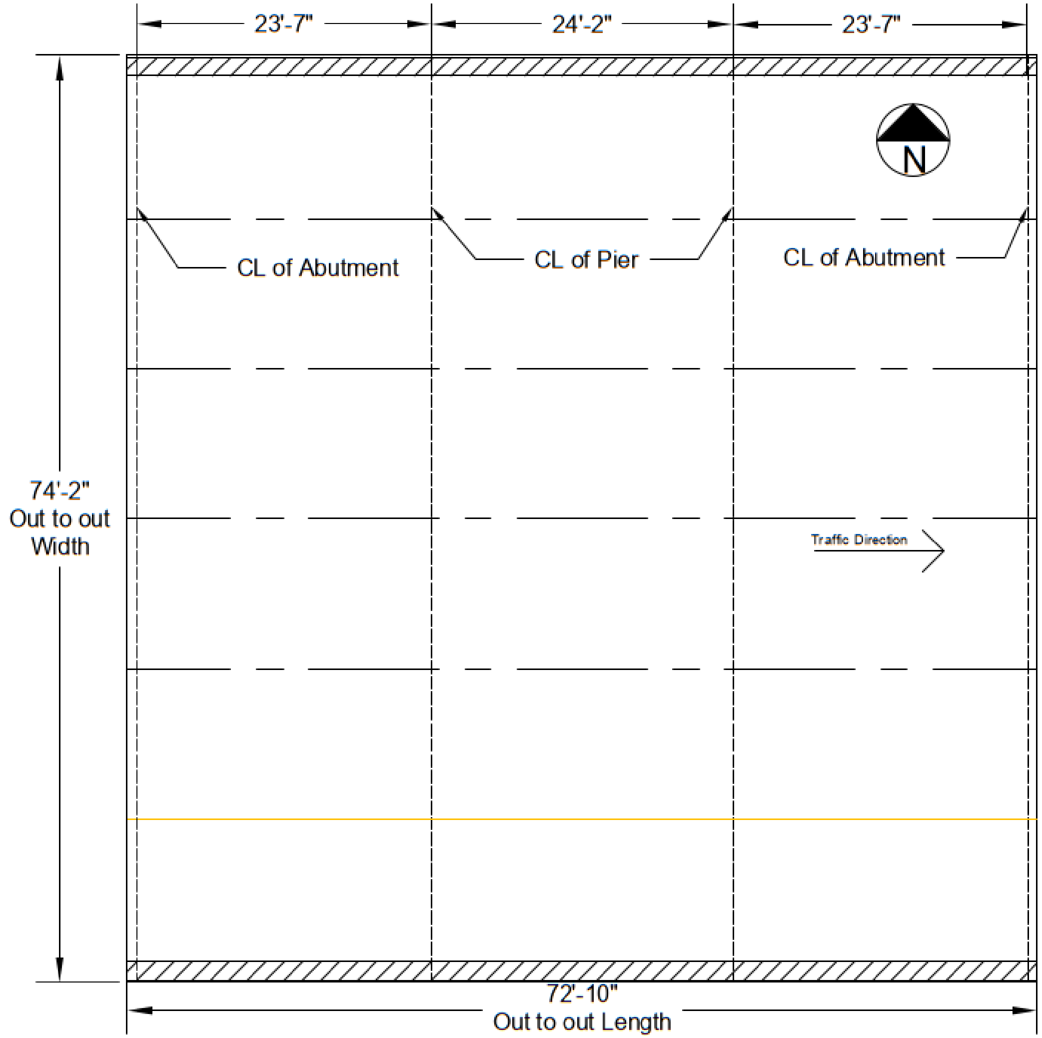

Figure 3.3: Plan view of the secondary slab-span bridge (Bridge 27925).

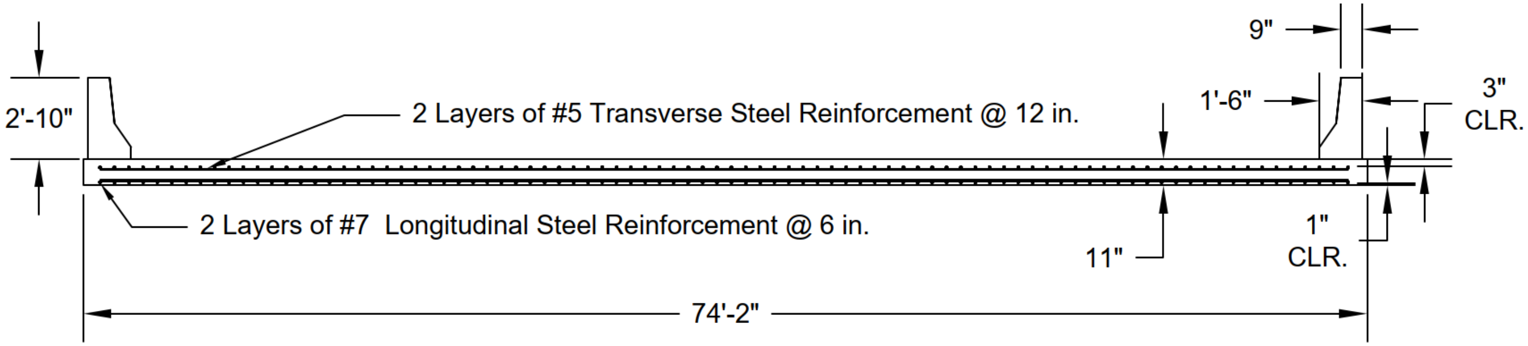

Figure 3.4: Cross-sectional view of the secondary slab-span bridge (Bridge 27925).

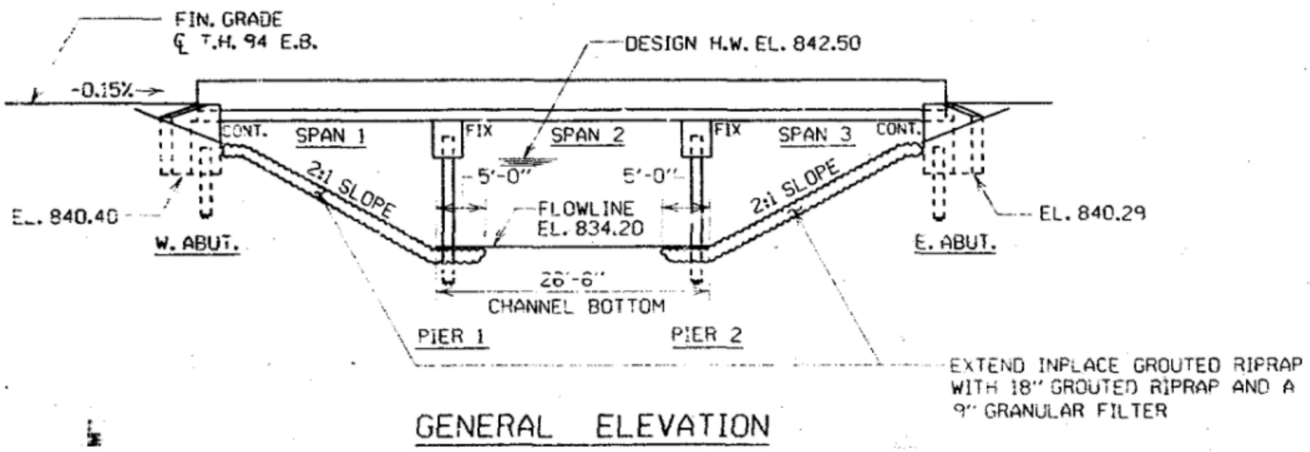

Figure 3.5 General elevation of Bridge 27909 reprinted from MnDOT (1988).

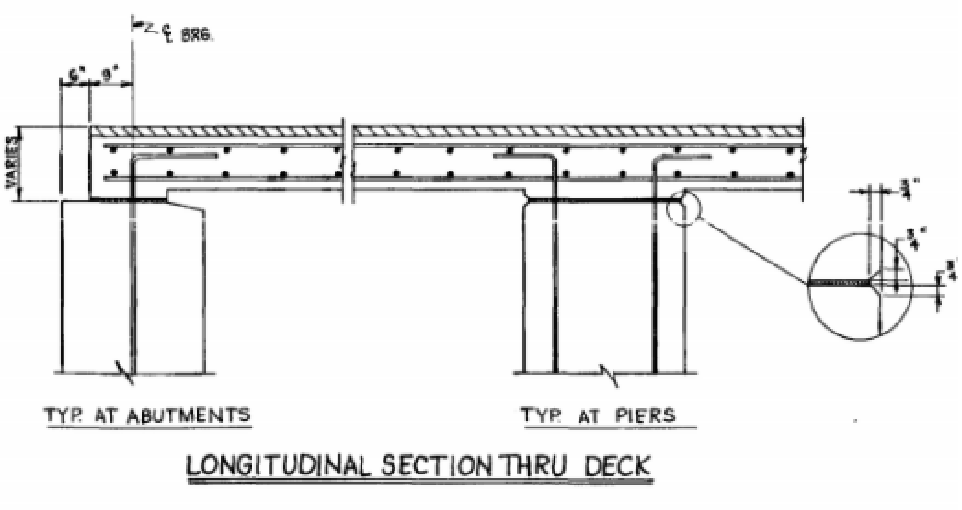

Figure 3.6 Longitudinal section of Bridge 27926 showing top and bottom reinforcement reprinted from MnDOT (1980).

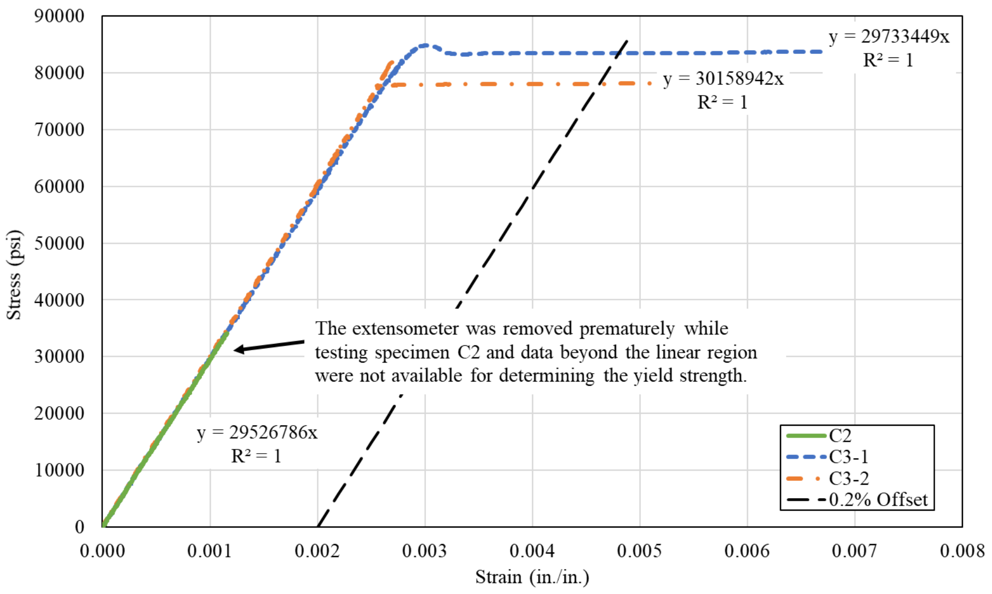

The extensometer was removed prematurely while testing specimen C2 and data beyond the linear region were not available for determining the yield strength.

Figure 3.7 Stress vs. strain data from the No. 7 reinforcement bar tests used to determine the modulus of elasticity (best-fit equations and coefficient of determination) and yield strength (0.2% offset).

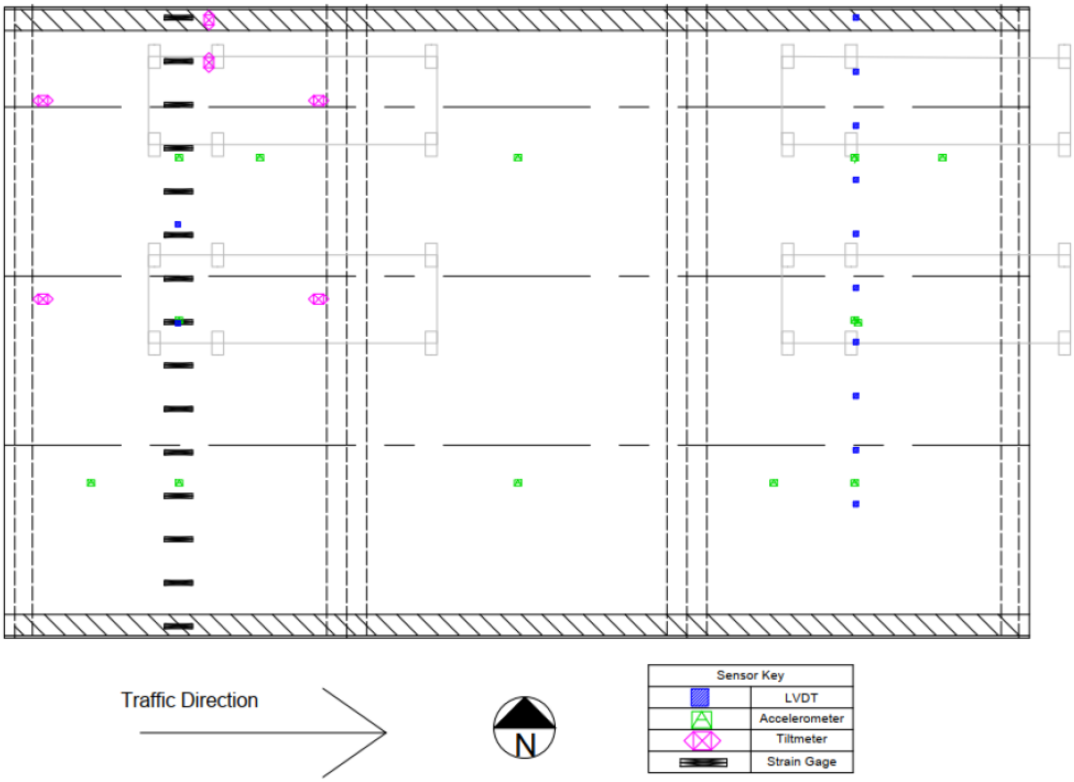

Figure 3.8: All sensor locations on Bridge 27926.

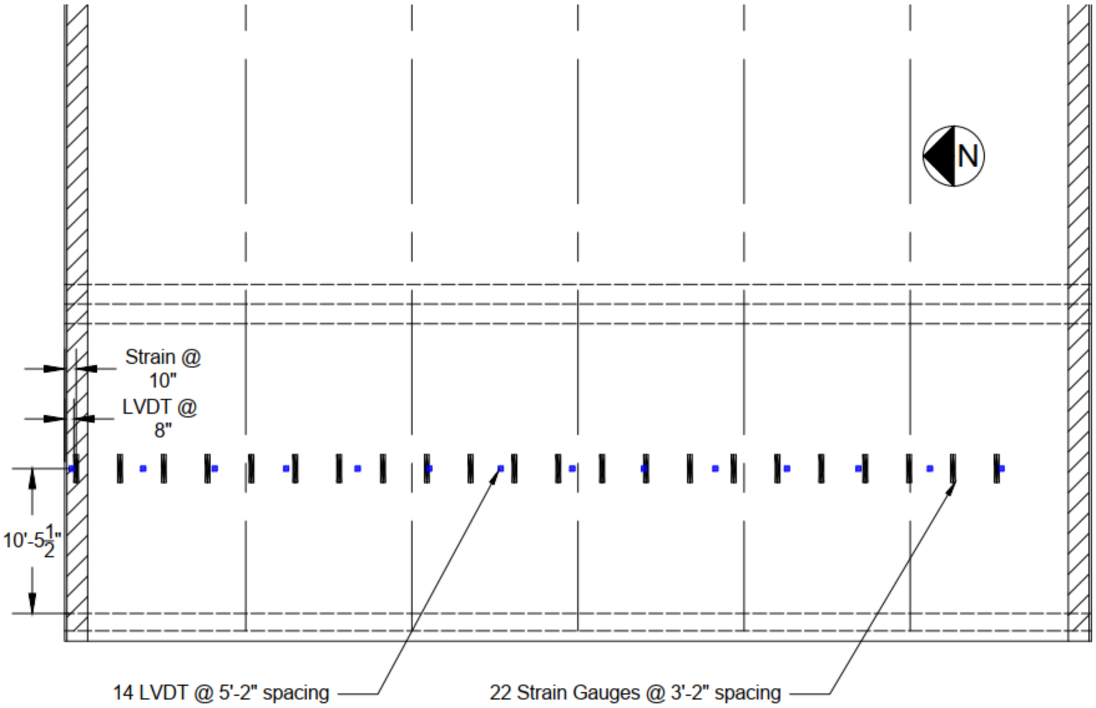

Figure 3.9: Strain and displacement sensor locations on the West span of Bridge 27925.

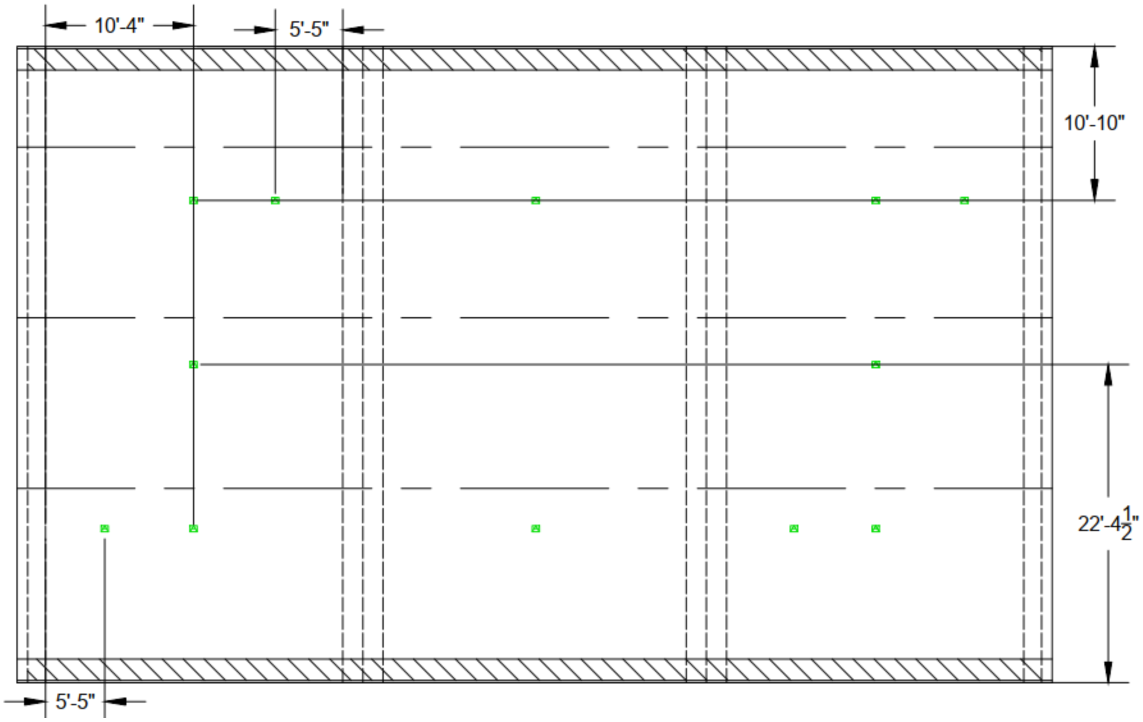

Figure 3.10: Accelerometer locations on Bridge 27926.

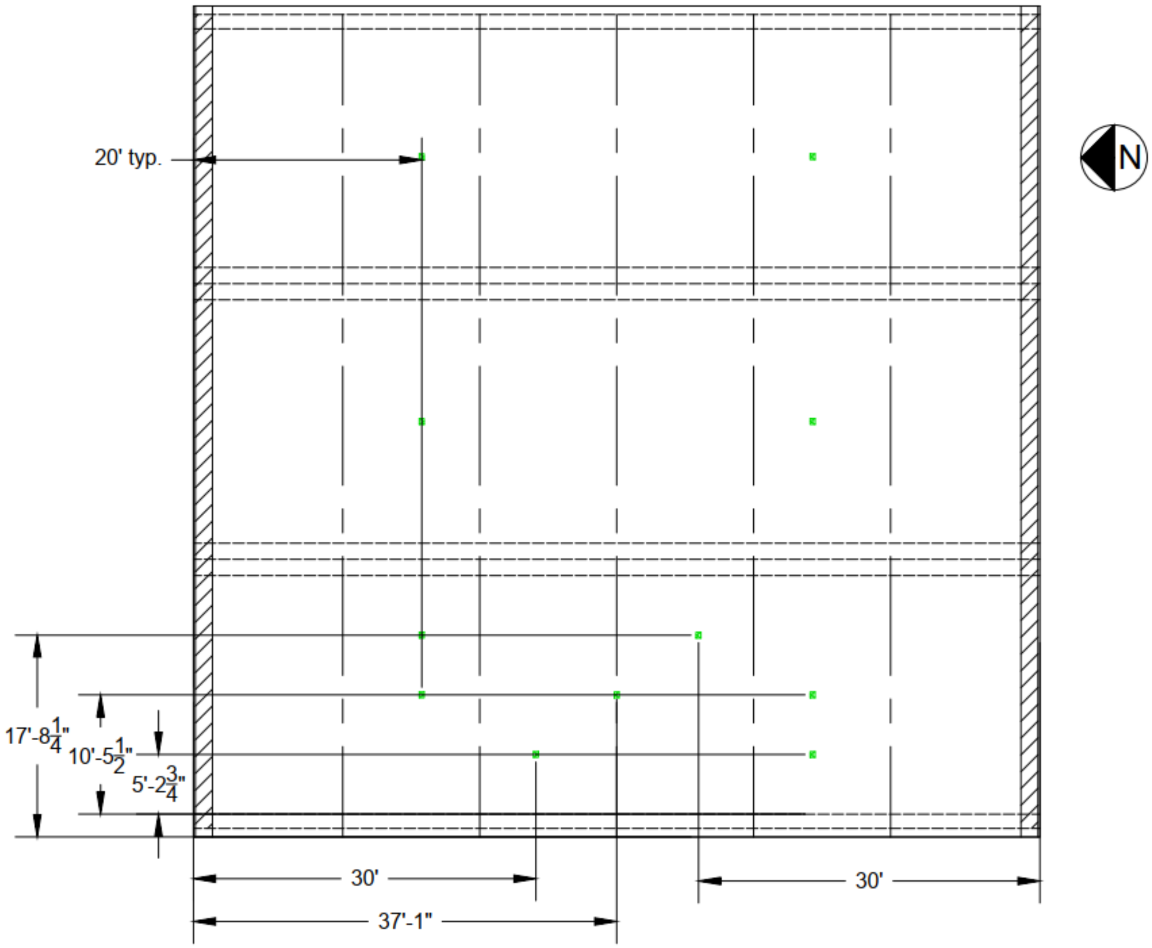

Figure 3.11: Accelerometer locations on Bridge 27925.

Figure 3.12: Accelerometer affixed to the slab of Bridge 27926 during dynamic testing.

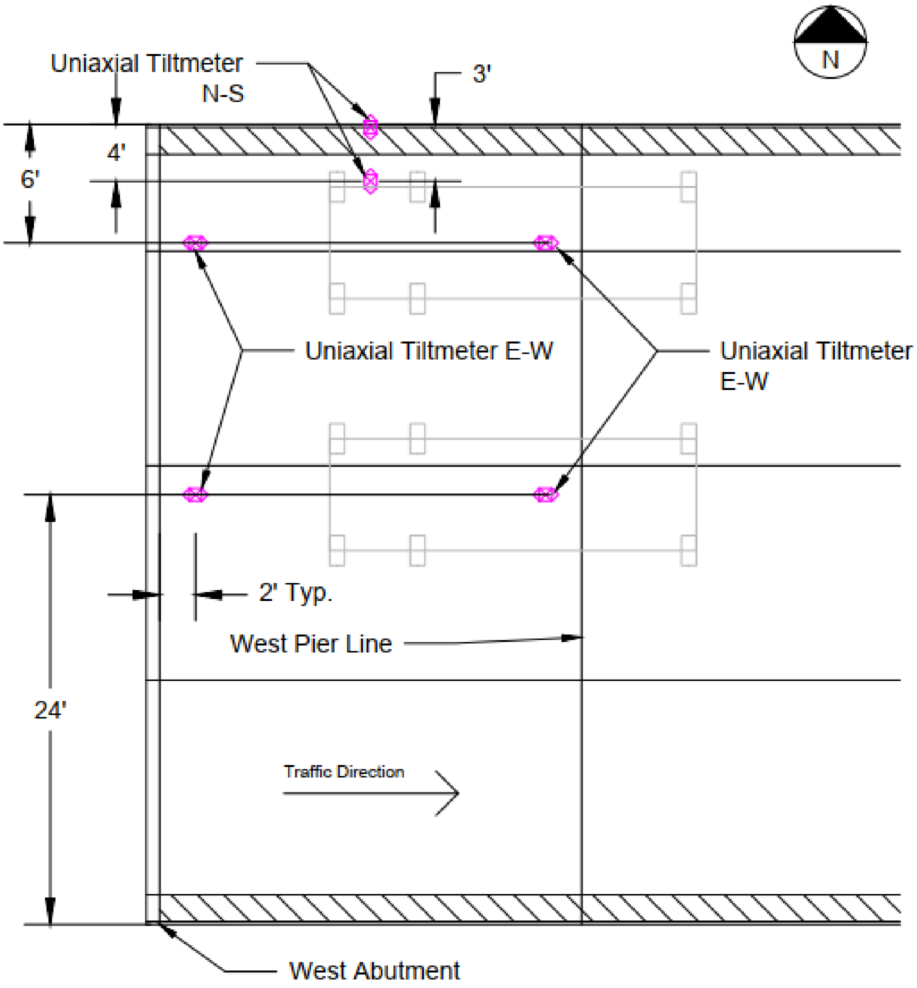

Figure 3.13: Tiltmeter locations on Bridge 27926.

Figure 3.14: Tiltmeter affixed to the slab of Bridge 27926 during field testing.

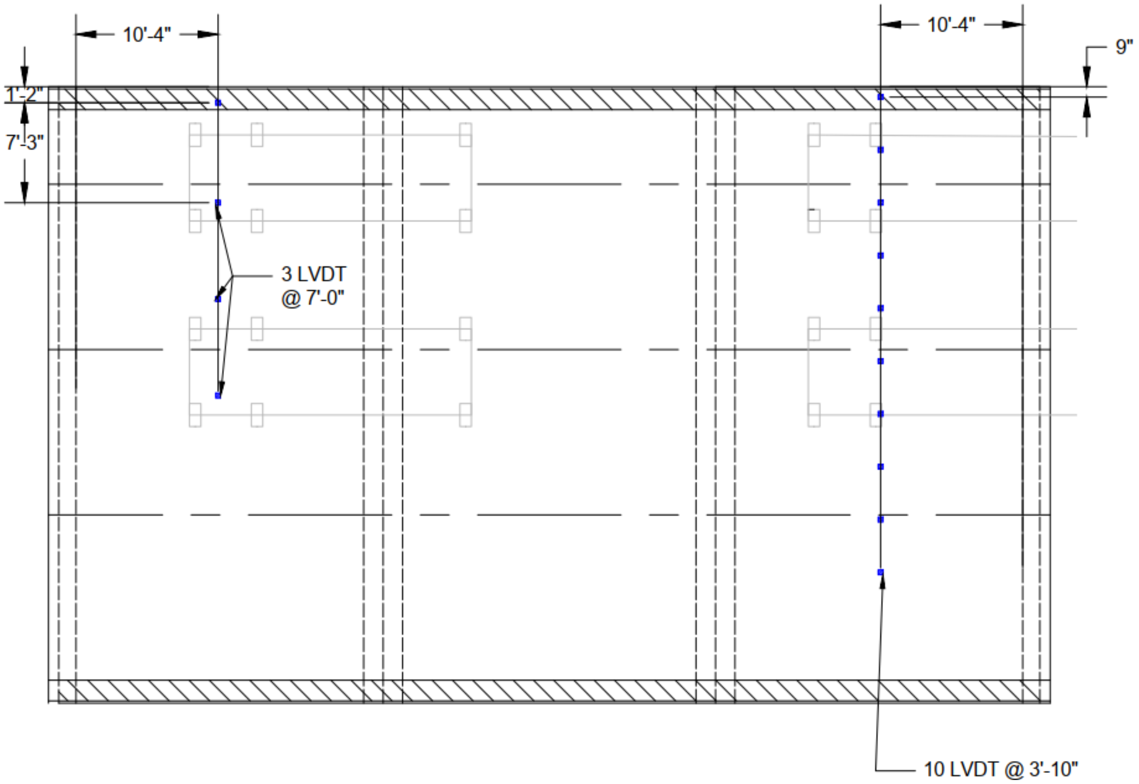

Figure 3.15: LVDT locations on Bridge 27926

Figure 3.16: LVDTs set up under Bridge 27926 during live load testing.

Figure 3.17: Strain gauges installed under Bridge 27926 during live load testing.

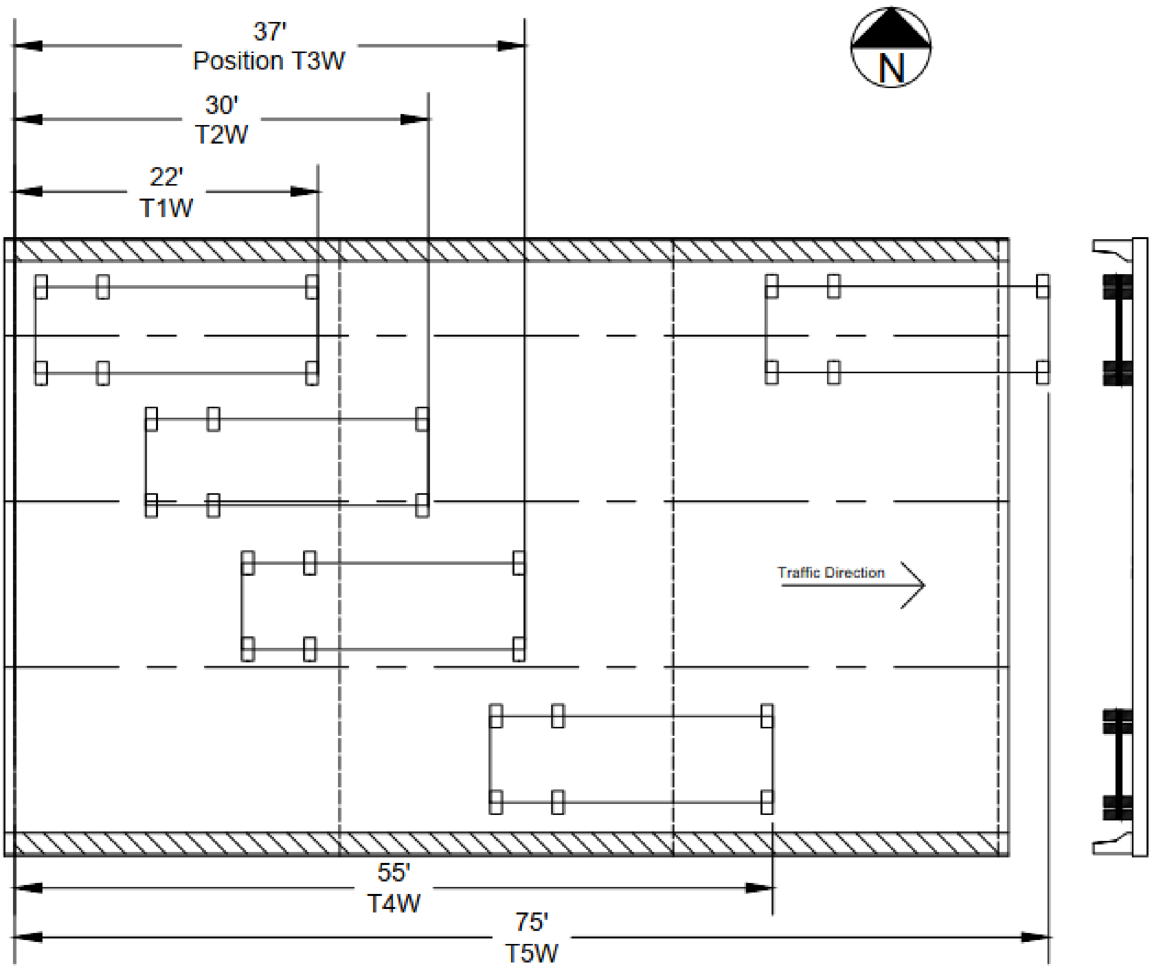

Figure 3.18: Truck positions along the length of Bridge 27926.

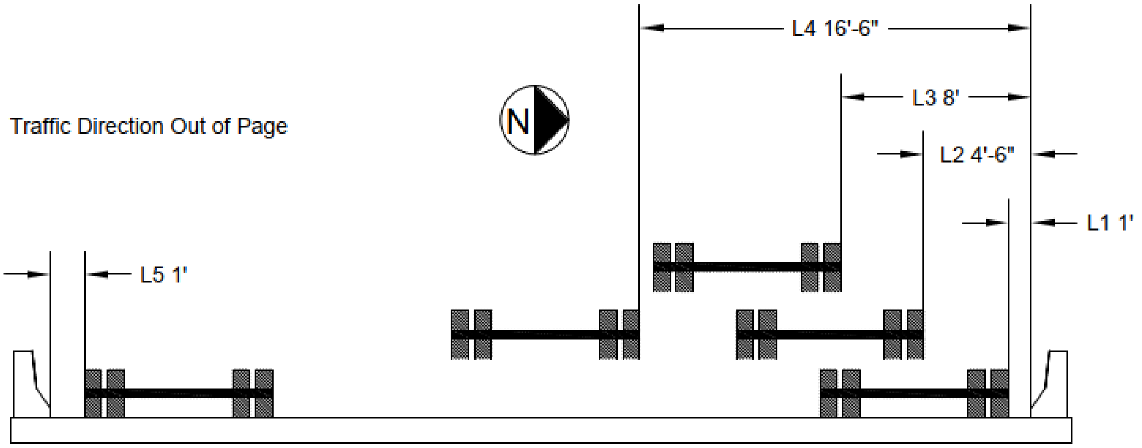

Figure 3.19: Truck test lane positions across the width of Bridge 27926.

Figure 3.20: Single truck test.

Figure 3.21: Side-by-side truck test.

Figure 3.22: Back-to-back truck test.

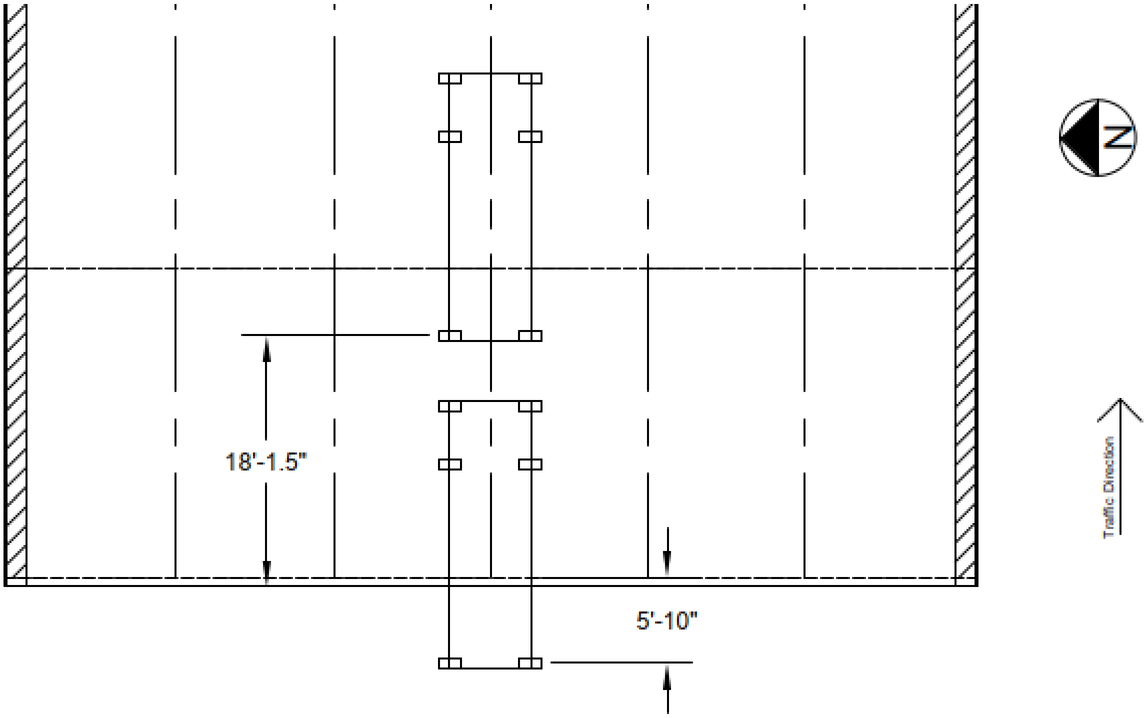

Figure 3.23: Truck positions along the length for back-to-back tests on Bridge 27925 with trucks facing West.

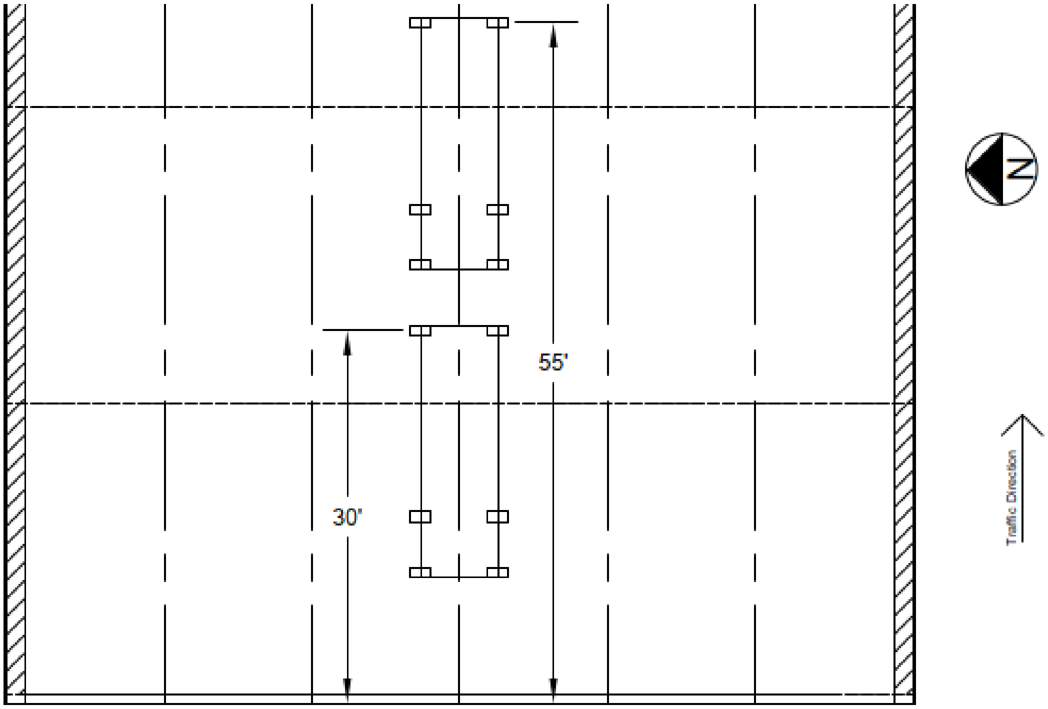

Figure 3.24: Truck positions along the length for back-to-back tests on Bridge 27925 with trucks facing East.

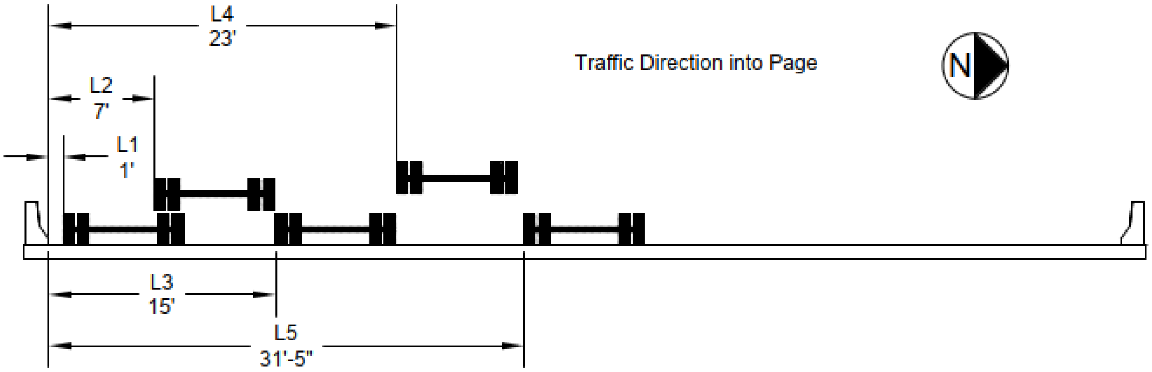

Figure 3.25: Truck test lane positions across the width of Bridge 27925.

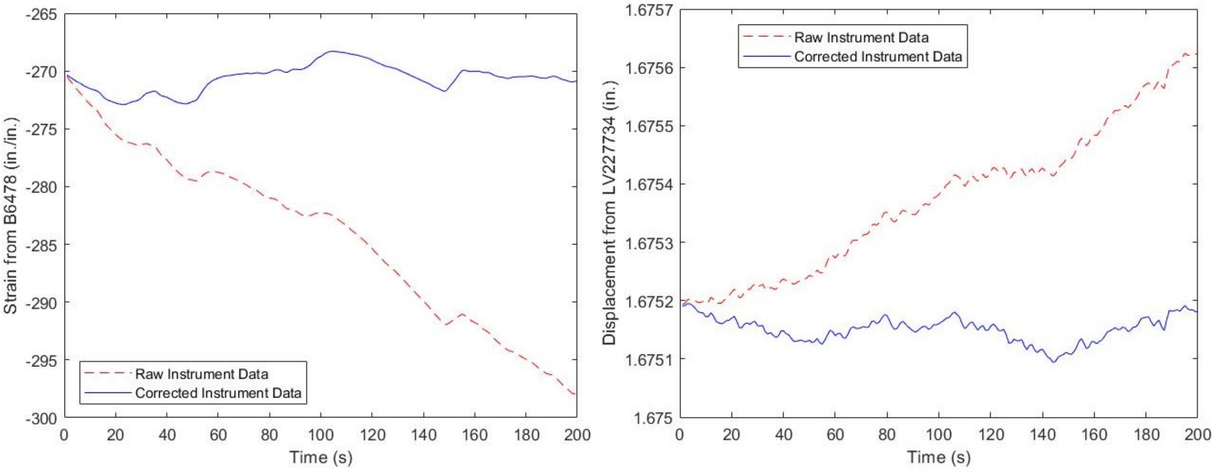

(a) **(b)**

Figure 3.26: Drift observed and corrected in a (a) strain gauge and (b) displacement sensor during a test with no truck load applied on Bridge 27926.

CHAPTER 4: COMPUTATIONAL MODELS

4.1 THREE-DIMENSIONAL FINITE ELEMENT MODEL

A detailed FEM was created in Ansys using the static structural package. The modeled geometry is based on the as-built plans for Bridge 27926 that are shown in Figure 3.1 and Figure 3.2. The model described in the following sections is visualized in Figure 4.1. Section 4.1.1 describes the final, updated model for generating results under the loading described in Section 4.1.2. Section 4.1.3 describes the processes that were applied in developing this final model, the validation of which is shown in Section 4.1.4.

4.1.1 FEM Geometry and Elements

During field visits, the layout and condition of the primary structure was observed. The slab depth and barrier type were confirmed to match the bridge plans. The steel reinforcing size and grade were also confirmed from samples obtained during coring. A crack survey was conducted on Bridge 27926 to characterize the condition of the underside of the concrete slab. Crack widths of 2, 6, and 12 in. were determined in the field by measuring the extent of spalling; the location and size of these cracks are shown in Figure 4.2.

Inelastic material properties were specified for the FEM. These included isotropic elasticity properties and Menetrey-Willam properties for nonlinear concrete material behavior, including compressive and tensile strengths. The modeled concrete f'_c was 9.48 ksi, concrete E was 3725 ksi, concrete Poisson's ratio was 0.2, and concrete tensile strength was 0.216 ksi. The steel reinforcement was bonded to the surrounding concrete throughout the model. The steel isotropic elasticity and isotropic multilinear hardening were modeled using properties obtained from field samples. A stress-strain plot highlighting the points used to define the multilinear hardening properties is shown in Figure 4.3.

The concrete barriers were modeled as fully connected via a surface-to-surface bond between the barrier and the concrete slab. The connections to the slab consisted of 5-in. by 10-in. patches at the locations where the concentration of steel reinforcement between the barrier and slab was the highest according to the bridge plans, which is visually depicted in Figure 4.4. The barrier geometry matched the as-built plans considering both dimensions and deflection joints. Reducing the surface area of the connection between the barriers and the slab and including the deflection joints at midspan of each span and at each pier resulted in increased transverse displacement and strain profiles near the edge of the slab compared to results generated when the barriers were fully bonded without deflection joints, especially when load was transversely placed 1 ft from the barrier.

Boundary conditions restraining all displacement degrees of freedom were applied at the two abutments and two piers. Additionally, rotations were free at the supports to match the rotation data collected in the field. This amount of fixity was corroborated through analysis of the modal frequencies collected in the field compared to a simple elastic model with fixed supports and rotations allowed at the supports. The supports are visualized in Figure 4.5(a) for the abutment connections and Figure 4.5(b) for the pier connections. The supports were fully connected using general body to ground connections in Ansys Static Structural.

The crack survey conducted on Bridge 27926 was used to define the FEM mesh geometry. The final meshing reflected observed cracks and spalling in the direction of traffic in all three spans of the structure. The bottom of the slab was split into “longitudinal strips” of slab that retained the measured material properties and strips of slab with a modulus of elasticity near zero to simulate cracks. The cracks were assumed to extend 6 in. up into the slab because that is approximately the distance from the bottom of the slab to the lowest fiber of the top mat of reinforcing steel and near the neutral axis of the slab.

The slab was modeled with 6-in. hexahedral elements. The steel reinforcing was modeled with 6-in. elements to align with the nodes of the slab elements. The cracks were modeled with either 3-in. by 6-in. or 2-in. by 6-in. hexahedral elements. The wearing course was modeled with 12-in. by 1-in. elements, which was selected to reduce the number of elements in the model and improve computation time. The barriers were modeled with 5-in. hexahedral elements because the shape of the barriers did not allow for easy meshing using 6-in. elements.

4.1.2 FEM Loading

Load was applied to the FEM through 10-in. by 20-in. wheel patches (AASHTO, 2020) that were configured to match the axle geometry of the MnDOT dump trucks used during field testing. The load applied to each patch corresponded with a portion of the weight of the MnDOT dump trucks used during field testing. The front axle wheel patches had 15.4 kips applied over the combined area and the tandem axles had 34.6 kips applied over the combined area. The FEM loading locations matched truck positions used in the field as described in Section 3.4 to streamline model validation. Modeling focused on the following truck positions (shown in detail in Appendix E for Bridge 27926):

- L1T2W near the barrier with the rear axles of the truck at midspan of an end span and the front axles in the center span, which aligned with strain data collected from the field
- L1T5W near the barrier with the rear axles at midspan of an end span and the front axles off the bridge, which aligned with displacement data collected in the field
- L4T2W at centerline of the bridge with the rear axles of the truck at midspan of an end span and the front axles in the center span, which aligned with strain data collected from the field

L4T5W at the centerline of the bridge with the rear axles at midspan of an end span and the front axles off the bridge, which aligned with displacement data collected in the field

4.1.3 FEM Development and Updating

Upon completion of the field testing, a preliminary inelastic FEM was updated to the final model described in Section 4.1.1 using the field data. The shape and magnitude of the transverse displacement and strain curves were used for validation instead of matching strain or displacement data at individual points. FEM results were computed under bridge self-weight only and under bridge self-weight plus the truck loading. To ensure consistency with field data, which only captured the change in response due to the truck loading, the presented FEM results are the results with self-weight plus truck loading minus the results with self-weight only. In addition to strain and displacement, rotations in the direction of traffic near the supports and the identified mode shapes and frequencies were used to validate the FEM results. The following items were considered during the FEM updating process after field testing:

- Impacts of barriers
- Connections and stiffness
- Support boundary conditions

4.1.3.1 Impacts of Barriers

In Figure 4.7 through Figure 4.10, the results from three preliminary FEMs are shown as blue, green, and red lines and data from the truck tests are shown as black lines. These three models were as follows:

- Elastic Model – Only elastic material properties were used for all materials, and the bridge had no distress or cracking
- Cracked (2 in.) – Inelastic properties were included, and 2-in. wide longitudinal cracks were included matching the crack survey, to examine the effects of inelastic modeling and minor cracking
- Cracked (24 in.) – Inelastic properties were included, and 24-in. wide longitudinal cracks were included to examine possible effects of extreme cracking

All three models were considered either with a fully bonded barrier (called “Full Geometry” in the figures) or no barrier at all (called “without Barriers” in the figures) to examine the impacts of including barriers.

Peak strain for a truck near the barrier, shown in Figure 4.7, ranged from 21 με for the elastic model with barriers to 53 με for the inelastic model with 2-in. cracks without barriers. The peak strains for the truck near the centerline, shown in Figure 4.8, ranged from 26 με for the fully elastic model without barriers to 47 με for the inelastic model with 24-in. cracks and full geometry. When the load was placed near the barrier, the strains were 68.6% larger in the elastic model, 129.0% larger in the inelastic model with 2-in. cracks, and 20.0% larger in the inelastic model with 24-in. cracks with the barriers removed. However, the presence of the barrier appeared to have little effect on the peak strain when the load was positioned near the centerline of the bridge. When the load was placed near the centerline, the strains were 3.5% smaller in the elastic model, 1.8% larger in the inelastic model with 2-in. cracks, and 8.7% smaller in the inelastic model with 24-in. cracks with the barriers removed.

The peak FEM displacement was more affected by the presence of a concrete barrier under both loading scenarios. Peak displacement for a truck near the barrier, shown in Figure 4.9, ranged from 0.015 in. for the fully elastic model with barriers to 0.049 in. downward for the inelastic model with 24-in. cracks without barriers. The displacement for the truck near the centerline, shown in Figure 4.10, ranged from 0.017 in. for the fully elastic model with full geometry to 0.033 in. downward for the inelastic model with 24-in. cracks and full geometry. When the load was placed near the barrier, the magnitude of the displacements were 91.2% larger in the elastic model, 145.2% larger in the inelastic model with 2-in. cracks, and 96.4% larger in the inelastic model with 24-in. cracks with the barriers removed. When the load was placed near the centerline, the displacements were 15.9% larger in the elastic model, 8.5% larger in the inelastic model with 2-in. cracks, and 6.2% smaller in the inelastic model with 24-in. cracks with the barriers removed. These differences illustrate the stiffness that is added when the barrier is included in the model.

Data from the field included a peak strain of 36.7 με for a 50-kip truck parked near the barrier and 43 με for a 50-kip truck parked near the centerline. Displacement data from the field show the peak displacement was 0.020 in. downward when a truck was parked near the barrier or near the centerline. These values are within the expected range of strains and displacements from the preliminary FEM results.

Comparing the FEM results to the field data provided insight into which modeling technique best represented the actual response of the bridge. When considering the strain response to load applied near the barrier, the magnitude of the field data was between results from the elastic FEM without barriers and the inelastic model with 2 in. cracks with barriers. However, the shape of the field strain data was most like the inelastic model with 24 in. cracks and no barriers. For load near the centerline, the shape of the strain plot from the field data was most like the inelastic model with 24 in. cracks both with and without barriers. When considering the displacement response to load applied near the barrier, the shape of the data fit best with the FEM with barriers because the magnitude of the displacement decreased closer to the edge of the slab. Furthermore, both cracked FEMs with barriers fit well with the field displacement data for a load near the barrier as the field data indicate displacement in the upward direction toward the centerline. For the displacement response to load near the centerline, the shapes of the FEM results and field data were all similar, but the response from the elastic model without barriers most closely matched the magnitude of the field data displacement. Overall, the shape of the response from models with barriers matched the field data best. It is possible that the barriers impact behavior most near the edge of the slab while longitudinal cracks impact the behavior most near the transverse centerline.

4.1.3.2 Connections and Stiffness

The barrier-to-slab connection was assumed to be fully bonded along the length of the bridge in the preliminary FEM models, and the five deflection joints at midspan of each span and at each pier were neglected. However, as described in Section 4.1.1, the barrier deflection joints were included in the final FEM and updates to the barrier-to-slab connection were made such that the barrier was fully connected to the slab using 5-in. by 10-in. patches at the locations where the concentration of steel reinforcement between the barrier and slab was the highest according to the bridge plans. Reducing the surface area of the connection between the barriers and the slab and adding the deflection joints resulted in increased transverse displacement and strain profiles near the edge of the slab, especially when load was transversely placed 1 ft from the barrier. The stiffness of the slab was further reduced by lowering the elastic modulus of the slab concrete from 3725 to 3000 ksi (approximately 20% reduction) while still utilizing the f'_c determined from field samples. This modulus reduction was used to account for the presence of longitudinal cracks not explicitly modeled, which are described in the bridge inspection reports (Dumbeck, 2019a, 2019b, 2019c). This resulted in greater magnitude strains and displacements when the load was transversely placed near the centerline, which better matched bridge behavior characterized using field data.

4.1.3.3 Support Boundary Conditions

The mode shapes and natural frequencies obtained from field modal identification and initial elastic FEM were compared to determine support boundary conditions that should be applied to the final model. The mode shapes determined from field data were compared to mode shapes from the FEM based on locations of peak displacement response and zero-crossings (the point where a modal displacement profile switches between positive and negative) to evaluate the fixity of the support boundary conditions used in the model. The expected frequencies from analysis were between 20 and 30 Hz. The dynamic results from field testing indicated that the primary structure exhibited discernable frequencies beyond the expected range, which were not entirely captured by the sensor layout. The range of frequencies identified in the model was adjusted to include higher frequency mode shapes matching those observed in the field data.

Rotations at all supports were assumed to be fixed in the direction of traffic in the initial models. The bridge displacement behavior with fixed rotations over the supports fit the field data poorly. The FEM technique was updated such that rotations were allowed at the supports, which fit the displacement behavior observed using field data. This modeling decision was corroborated through analysis of the modal frequencies collected in the field and comparison to initial elastic model results that incorporated either fixed supports or supports that allowed rotation.

4.1.4 FEM Validation Results

FEM results were compared to field test data with trucks transversely positioned 1 ft from the barrier and at the bridge cross-sectional centerline at midspan of the two end spans. Results from a FEM that incorporated the updates were compared to results from previous versions of the FEM to observe the impact of changing different parameters. The different parameters for each model update are listed below.

- Model 1: initial baseline model including as-built geometry, inelastic material properties discussed in Section 4.1.1, measured material properties as shown in Table 3.1 and Table 3.2, rotations free at the supports, and crack patterns based on results from the crack survey (Figure 4.2).

- Model 2: same as Model 1 with barrier connections changed from fully bonded to 5-in. x 10-in. patches at the locations where the concentration of steel reinforcement between the barrier and slab was the highest according to the bridge plans.
- Model 3: same as Model 2 with rotations in the direction of traffic fixed at all supports.
- Model 4: same as Model 2 with 8-in. crack depth and concrete slab modulus of elasticity of 3000 ksi (reduced from 3725 ksi).
- Model 5: same as Model 1 with concrete barrier modulus of elasticity of 1000 ksi (reduced from 3725 ksi).
- Final Model: same as Model 2 with concrete slab modulus of elasticity of 3000 ksi (reduced from 3725 ksi).

The iteration process is visualized in Figure 4.11 through Figure 4.15. These figures depict the six examples of the FEM with differing parameters. Only the varied parameters with the most obvious affects were included. Two sets of field data (Field Data 1 or 2) were plotted for each location and for each data type because two truck tests were conducted at each position. Behavior from each model was visually compared to the field data and the behavior was numerically compared to the field data using a modal assurance criterion (MAC) that was generated using Equation 4.1 for strain and Equation 4.2 for displacement. Results are shown in Table 4.2. MAC values are typically used for comparing modes by normalizing the magnitudes to identify consistencies in the overall shape of the modal displacement. The same idea was applied to the strain and displacement profiles from the field-tested structure.

$$c = \frac{\left(\varepsilon_f \cdot \varepsilon_m\right)^2}{\left(\left(\varepsilon_f \cdot \varepsilon_f\right) \cdot \left(\varepsilon_m \cdot \varepsilon_m\right)\right)} \tag{4.1}$$

$$c = \frac{\left(\Delta_f \cdot \Delta_m\right)^2}{\left((\Delta_f \cdot \Delta_f) \cdot (\Delta_m \cdot \Delta_m)\right)} \tag{4.2}$$

Where *c* is the criterion value varying from 0 to 1, with 1 describing perfect correlation between modes *f* and *m*; ε_f is a vector containing field test strain data across the transverse profile of the bridge; ε_m is a vector containing FEM strain results across the transverse profile of the bridge that correspond to each value in the field test vector; Δ_f is a vector containing field test displacement data across the transverse profile of the bridge; and Δ_m is a vector containing FEM displacement results across the transverse profile of the bridge that correspond to each value in the field test vector.

Results in Figure 4.11 show that the magnitude of strain and displacement increased at the edge of the slab when the connected surface area between the barrier and slab was reduced, while the results near the centerline were largely unchanged. The new profiles obtained with the reduced connection were visually a better fit for the data. Results in Figure 4.12 show that the magnitude of the displacement was reduced by fixing rotations at the supports in the direction of traffic. From this comparison, the model with rotations allowed at the supports in the direction of traffic was shown to be a better fit for the field test data. Results in Figure 4.13 show that increasing the modeled crack depth from 6 in. to 8 in. as well as lowering the modulus of elasticity from 3725 ksi to 3600 ksi caused irregularities at the locations of the cracks. Overall, the strains were increased throughout the result profiles. Results in Figure 4.14 show the increased magnitude in displacement near the barrier when the modulus of elasticity in the barrier was reduced to 1000 ksi. Figure 4.15 shows results from the final model with slab modulus of elasticity of 3000 ksi and the connected surface area between the slab and barrier reduced compared to a model with the modulus of elasticity in the barriers of 1000 ksi and full barrier connectivity. The reduced modulus in the barriers provided displacement results that had a greater magnitude than those observed in the field while the model with a barrier modulus of elasticity of 3725 ksi provided a better fit. Ultimately, validation of the modeling technique led to the final model that was outlined in Section 4.1.1.

4.2 PLATE MODEL

4.2.1 Plate Model Geometry and Elements

A simplified plate model was constructed for the primary and secondary structures. The modeling technique used the as-built plans to determine the slab geometry including span lengths, thickness (slab and topping), and support locations. Steel reinforcement was neglected. The model of Bridge 27926 was 44-ft 9-in. wide and 72-ft 10-in. long while the model of Bridge 27925 was 74-ft 2-in. wide and 72-ft 10-in. long. Both models had a slab depth of 13 in. that accounted for the 11-in. slab depth and 2-in. topping thickness, and the mesh size was 5 in. throughout for both the slab and barriers.

The ends of the slab were fixed at the outside edge of the abutments as shown in Figure 4.16(a) along the entire length of the support from edge of slab to edge of slab. The pier fixity location was representative of where steel reinforcement connects the pier to the slab (two connections, 10 in. from the edges of the pier) as shown in Figure 4.16(b) along the entire width of the slab from edge of slab to edge of slab.

4.2.1.1 Barriers

The barriers in the plate models were represented as beam elements following the edge line of the outer edge of the slab and along the entire length of the bridge, crossing all three spans and all five supports. The barrier height was 13 in., and the width was 18 in. The height was selected to align with the distance from the base of the barrier to the bottom of the deflection joint; however, 2 in. were left off the barrier height since the slab thickness included the 2 in. topping height, which does not exist at the barrier location. Cross sections of the as-built barrier and plate model barrier are compared in Figure 4.17. The plate model barrier width was representative of the actual width of the base of the barriers. The barriers were then offset 9 in. toward the center of the slab (respective of the side of the bridge for each barrier) and 13 in. upward from the centroid of the slab. The offset was used because the plate model assumed the slab and beam elements to be on the same plane with their depths measured from the same location, and an offset placed the rectangular barrier in the correct geometric location.

4.2.1.2 Orthotropic Material Properties

The plate models used elastic concrete properties in the slab and barriers. The concrete modulus of elasticity was adjusted in the transverse direction in the models of the primary and secondary structures (orthotropic material properties). The adjustment reflected the observed cracks and spalling in the direction of traffic (Figure 4.2). The modulus was reduced to 22% of the base modulus of elasticity (measured value of 3725 ksi for Bridge 27926 and design value of 3600 ksi for Bridge 27925), which was approximately equal to the ratio of the cracked moment of inertia to the gross moment of inertia of a one-foot strip of slab in the transverse direction. After this reduction, the plate model results for Bridge 27925 still did not match the magnitude of the strain and displacement data observed in the field. To accommodate this, the modulus of elasticity of the Bridge 27925 plate model was also reduced in the longitudinal direction by 38.5%, which was approximately equal to the ratio of the cracked moment of inertia to the gross moment of inertia of a one-foot strip of slab in the longitudinal direction; results collected after making this change proved to be a better representation of the field data and fit better with the observed condition of the bridge. Bridge inspection reports for the two structures indicate that Bridge 27925 has approximately 2% more spalling and cracking per surface area for element 38 (reinforced concrete slab) in condition state (CS) 3 than does Bridge 27926 (Dumbeck, 2019b, 2019c). The concrete modulus of elasticity values and section properties are shown in Table 4.1.

4.2.2 Plate Model Loading

The plate model loading was identical to the FEM loading, which consisted of 10-in. by 20-in. patches configured to match the axle geometry of the MnDOT dump trucks used during field. The load applied to each patch corresponded with a portion of the weight of the MnDOT dump trucks used during field testing. The front axle wheel patches had 15.4 kips applied over the combined area and the tandem axles had 34.6 kips applied over the combined area. The FEM loading locations matched truck positions used in the field as described in Section 3.4 to streamline model validation. Modeling focused on the following truck positions (shown in detail in Appendix E for Bridge 27926):

- L1T2W near the barrier with the rear axles of the truck at midspan of an end span and the front axles in the center span, which aligned with strain data collected from the field
- L1T5W near the barrier with the rear axles at midspan of an end span and the front axles off the bridge, which aligned with displacement data collected in the field
- L4T2W at centerline of the bridge with the rear axles of the truck at midspan of an end span and the front axles in the center span, which aligned with strain data collected from the field
- L4T5W at the centerline of the bridge with the rear axles at midspan of an end span and the front axles off the bridge, which aligned with displacement data collected in the field

Additionally, L4T2W and another set of wheel patches mirrored 4 ft to one side was used as the multilane position.

Modeling for Bridge 27925 used the same method with detailed truck positions shown in Appendix G. The front axle of truck number 215556 was 15.4 kips and the rear axle of truck 215556 was 34.5 kips. The front axle of truck 214579 was 15.2 kips and the rear axle of truck 214579 was 33.8 kips. All load cases described below aligned with both displacement and strain data collected from the field:

- L1T1W near the barrier with the rear axles of the truck at midspan of an end span and the front axles in the center span
- L1T4W near centerline barrier with the rear axles at midspan of an end span and the front axles off the bridge
- L1T5W at centerline of the bridge with the rear axles of the truck at midspan of an end span and the front axles in the center span
- L1T1BB near the barrier with two back-to-back trucks with the rear axles at midspan of an end span and the front axles off the bridge
- L1T2BB about one truck width away from the barrier with two back-to-back trucks with the rear axles at midspan of an end span and the front axles off the bridge
- L1T3BB near the centerline of the bridge with two back-to-back trucks with the rear axles at midspan of an end span and the front axles off the bridge
- L1T4BB near the centerline of the bridge with two back-to-back trucks with the rear axles at midspan of an end span and the front axles off the bridge
- L1T5BB at the centerline of the bridge with two back-to-back trucks with the rear axles at midspan of an end span and the front axles off the bridge
- L1T1SS near the barrier with two side-by-side trucks spaced 4 ft apart the rear axles at midspan of an end span and the front axles off the bridge
- L1T4SS at the centerline of the bridge with two side-by-side trucks spaced 4 ft apart with the rear axles at midspan of an end span and the front axles off the bridge

4.2.3 Plate Model Validation Results

The final FEM results showed that the barriers added some stiffness to the structure to resist the applied truck loading. The barrier stiffness in the plate model was updated until the analytical displacement results had a MAC value greater than 0.95 when compared to the field data, resulting in the model described in the Section 4.2.1. A MAC value close to unity indicates that the compared points exhibit the same shape behavior. The recommended plate modeling technique used the in-situ barrier material properties and dimensions that were expected to resist bending in the slab. The barriers were modeled as a rectangle of width equal to the base width of the barriers and height equal to the height from the base of the barrier to the bottom of the deflection joint.

Incorporation of these parameters into the plate model for Bridge 27926 resulted in strains and displacements that were deemed acceptable when compared to the field measured values. Table 4.2 shows the MAC values for the final models compared to two repeat field tests at corresponding test locations. The MAC strain values from the FEM were affected by the presence of cracks in the model, due to this phenomenon the displacement data were the primary focus for MAC evaluation. Results in Table 4.2 show that the plate model exhibited excellent similarity to the field test data. Figure 4.18 shows plots of the model results and field data that were used to obtain the MAC values. Additional validation is shown in Table 4.3, where equivalent widths from the plate model are within 2% and 7% of those obtained from field strain and field displacement data, respectively.

A plate model for Bridge 27925 was created after validating the modeling technique with Bridge 27926 field data. Similar plots comparing the plate model results and field data for Bridge 27925 are shown in Figure 4.19 and Figure 4.20 for a set of analyzed truck positions. The strain and displacement profiles from the Bridge 27925 plate model were similar to those generated using field data. The similarity is shown further in Table 4.4, where displacement equivalent widths from the plate model are within 15% of those obtained from field data. However, the magnitude of strain values obtained from the Bridge 27925 plate model were smaller than those observed during field testing. Recording high values of strain (observed outliers) near concentrated loads while testing concrete specimens is common. The outlier data points from the field tests were kept in the equivalent width analysis since they would result in a more conservative value of *E*. Thus, the equivalent width results from the Bridge 27925 plate model were up to 52% more than those calculated using field data for single truck loading scenarios.

4.3 FINAL VALIDATION

The strain values from the FEM of Bridge 27926 were affected by the presence of cracks in the model. For example, full FEM behavior in Figure 4.18(b) shows large, distinct gaps in the results at the modeled crack locations (e.g., approximately 225 or 300 in. from the edge of slab), which was corroborated by the low MAC values for FEM strain shown in Table 4.2. Furthermore, behavior in Figure 4.18(a) shows that the plate model strain results follow the field data across the width while the FEM strain results drop toward zero at the edge of the slab. This was likely because a crack was modeled at the edge of the slab in the FEM, which impacted the MAC value at that location. However, transverse displacement profiles from the end span of the bridge generated with FEM results were not directly affected by the presence of cracks in the model as shown in Figure 4.18(c) and (d). Thus, the displacement data were used for final FEM validation. Including cracks in the FEM achieved displacement results most like those observed in the field.

Though the FEM strain and displacement results were disparately impacted by the modeled cracks, the plate model results were similar in magnitude and MAC value when compared to field strain and displacements. The plate model results and the field test data had MAC values greater than 0.83 for strain and greater than 0.95 for displacement. The magnitude of the field strain and displacement data for the truck positions and repeat tests was similar to the plate model results as shown in Figure 4.18(b). The transverse strain and displacement behavior were accurately captured using the plate model, which was also easy to develop and required less computational power than the FEM.

Table 4.1: Material and section properties used in the plate models of Bridge 27926 and Bridge 27925.

Plate Model	E_c (ksi)	E_l (ksi)	E_t (ksi)	E_v (ksi)	I_g (in.^{4})	I_{crl} (in.^{4})	I_{crt} (in.^{4})	I_{crl} / I_g (%)	I_{crt} / I_g (%)
Bridge 27926	3725	3725	807	3725	2197	843	476	38.4	21.7
Bridge 27925	3600	1300	780	3600	2197	846	475	38.5	21.6

Note: E_c is the base concrete modulus of elasticity, which was measured for Bridge 27926 and taken as the design value for Bridge 27925; E_l is the modulus of elasticity used in the longitudinal direction (traffic direction); E_t is the modulus of elasticity used in the transverse direction (perpendicular to traffic direction); E_v is the modulus of elasticity used in the vertical direction, I_g is the gross moment of inertia of a 13 in. tall by 12 in. wide slab section; I_{crl} is the cracked moment of inertia in the longitudinal direction; and I_{crt} is the cracked moment of inertia in the transverse direction.

Table 4.2: MAC values comparing plate model and FEM strain and displacement results for Bridge 27926 to corresponding field test data obtained from two repeat truck tests at each position (load near the barrier and load away from the barrier).

Truck Test No.	Plate				FEM			
	Load 1 ft from Barrier		Load at Centerline		Load 1 ft from Barrier		Load at Centerline	
	ε	Δ	ε	Δ	ε	Δ	ε	Δ
1	0.9299	0.9607	0.9494	0.9877	0.7090	0.9833	0.7145	0.9949
2	0.9340	0.9499	0.8583	0.9781	0.7411	0.9788	0.6486	0.9907
3	0.9436	—	0.9366	—	0.7590	—	0.6871	—
Avg.	0.9360	0.9553	0.9148	0.9829	0.7364	0.9811	0.6834	0.9928

Table 4.3: Comparison of equivalent widths from the plate model and field data for Bridge 27926.

Data Source	Equivalent Width (E) in. for Different Truck Positions			
	L1T2W	L1T5W	L4T2W	L4T5W
Plate Δ	—	199	—	236
Field Δ	—	214	—	222
Plate Δ / Field Δ	—	0.93	—	1.06
Plate ε	189	—	229	—
Field ε	186	—	224	—
Plate ε / Field ε	1.02	—	1.02	—

Table 4.4: Comparison of equivalent widths from the plate model and field data for Bridge 27925.

Data Source	Equivalent Width (E) in. for Different Truck Positions									
	L1T1W	L4T1W	L5T1W	L1BB	L2BB	L3BB	L4BB	L5BB	Multilane 1	Multilane 2
Plate Δ	205	261	270	206	237	255	264	259	311	353
Field Δ	228	307	259	219	245	293	303	269	—	—
Plate Δ / Field Δ	0.90	0.85	1.04	0.94	0.97	0.87	0.87	0.96	—	—
Plate ε	204	273	278	209	304	325	336	336	321	358
Field ε	192	180	204	174	224	166	178	262	—	—
Plate ε / Field ε	1.06	1.52	1.36	1.20	1.36	1.96	1.88	1.28	—	—

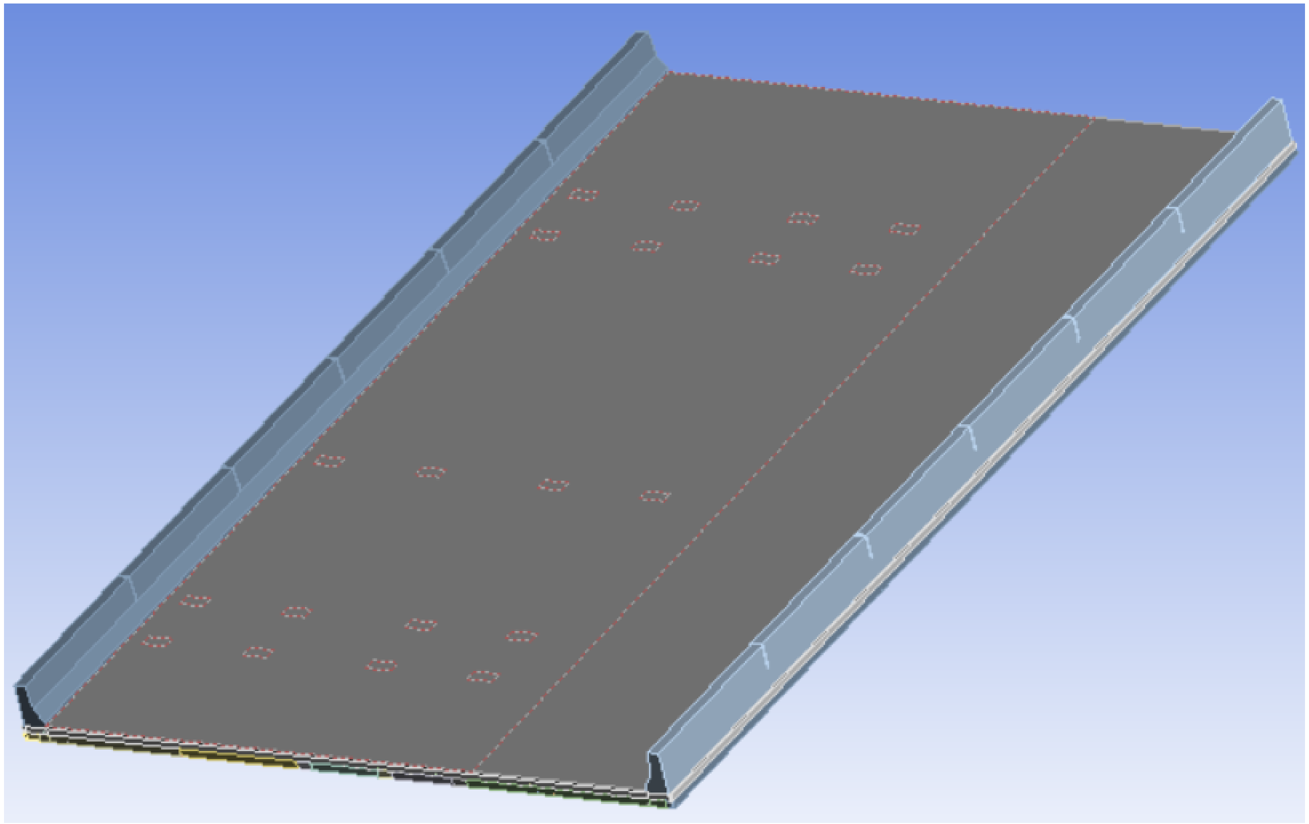

Figure 4.1: Isometric view of the FEM from Ansys.

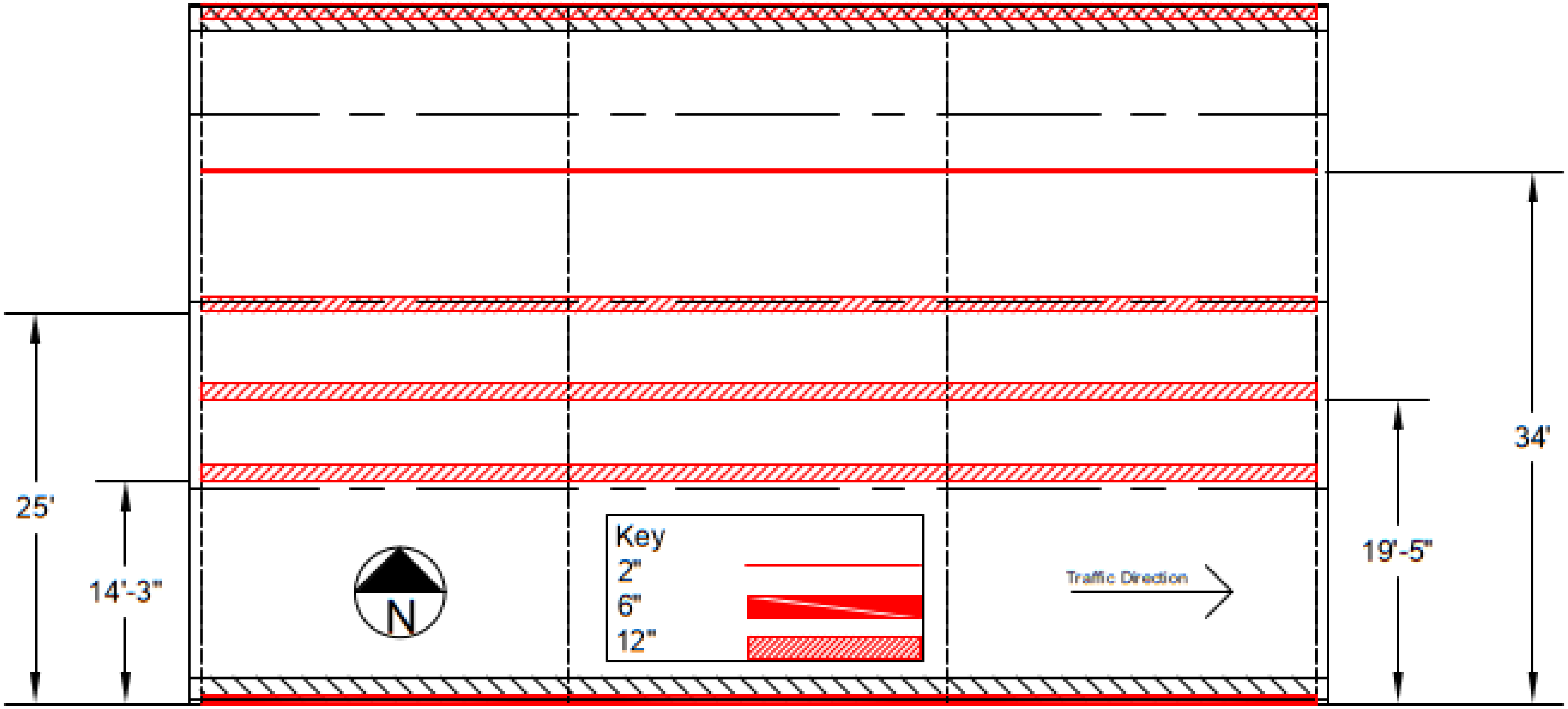

Figure 4.2: Crack survey data from Bridge 27926 used to define the FEM mesh geometry.

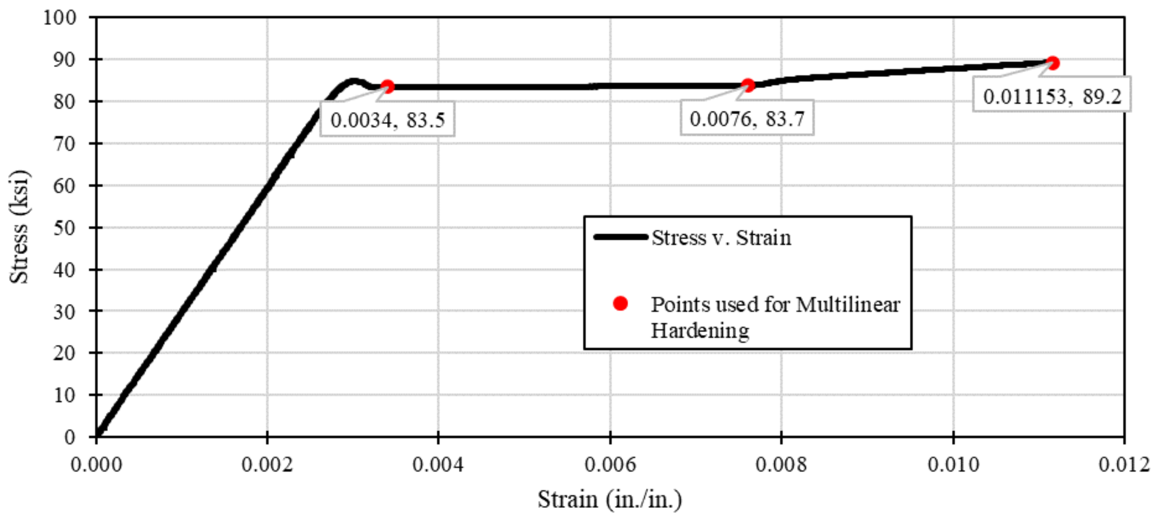

Figure 4.3: Multilinear hardening points used for FEM steel reinforcing properties.

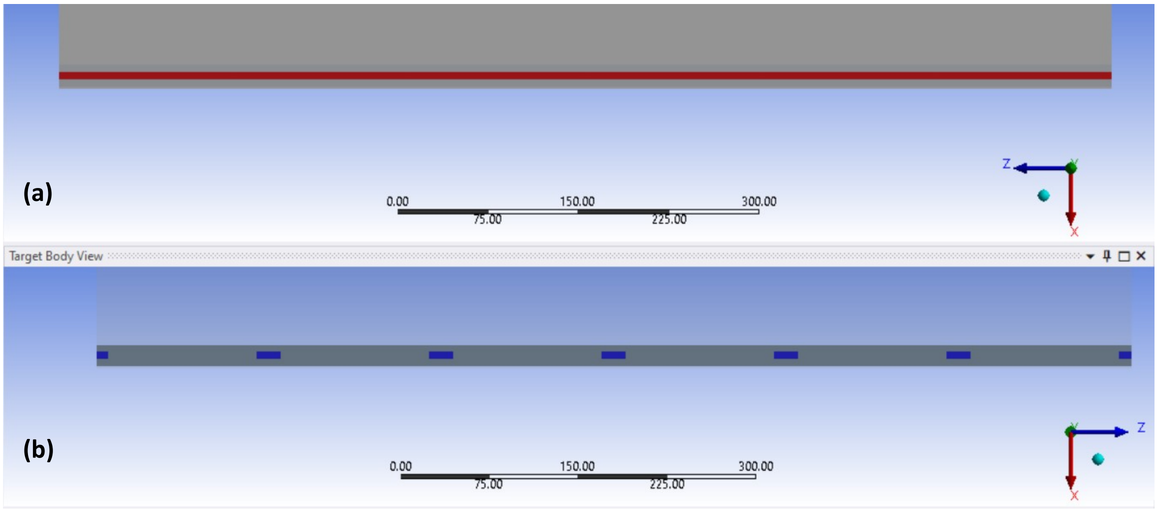

Figure 4.4: (a) Top-down view of the edge of FEM slab with a red area indicating the location of the barrier and a (b) top-down view of the barrier with blue areas indicating the highest concentration of reinforcement between the slab and barrier as well as the locations of connection between the slab and barrier in the FEM.

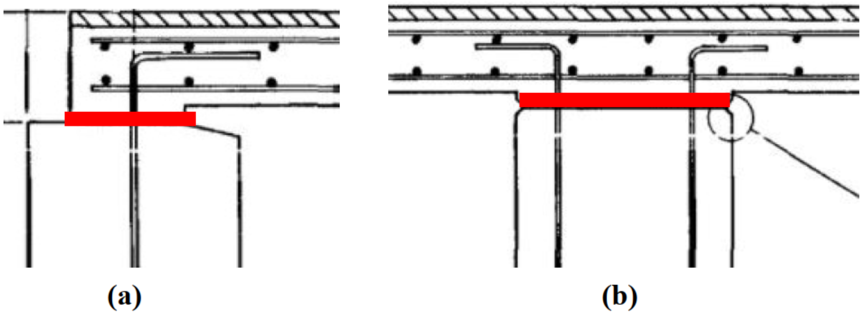

Figure 4.5: Location of the full-width support condition at the (a) abutment and (b) intermediate pier in the validated FEM. The connection locations are highlighted with red rectangles.

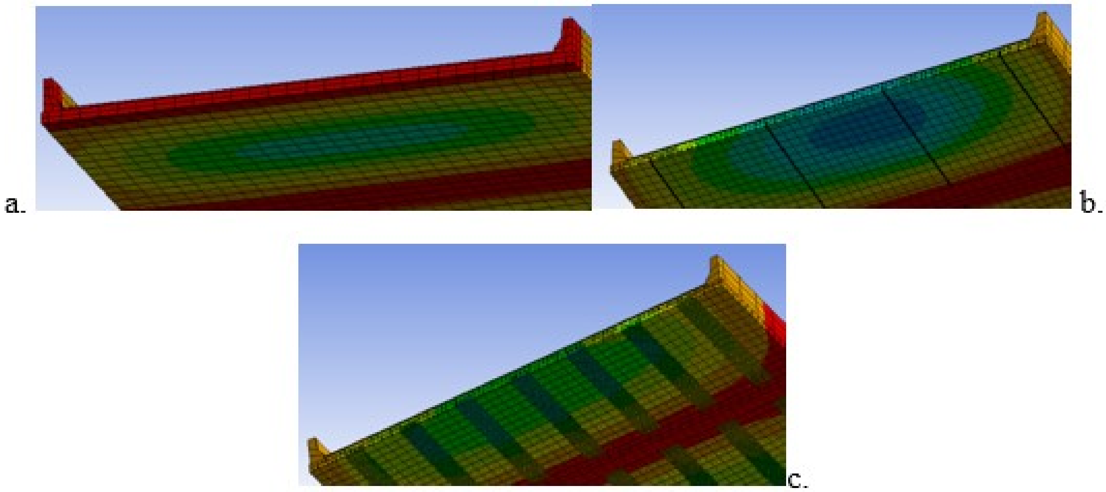

Figure 4.6: Isometric view of the underside of the slab showing (a) conventional elastic model, (b) cracked model with four 2 in. cracks per span (shown with thick black lines), and (c) cracked model with seven 24 in, cracks per span (shown with thick black lines).

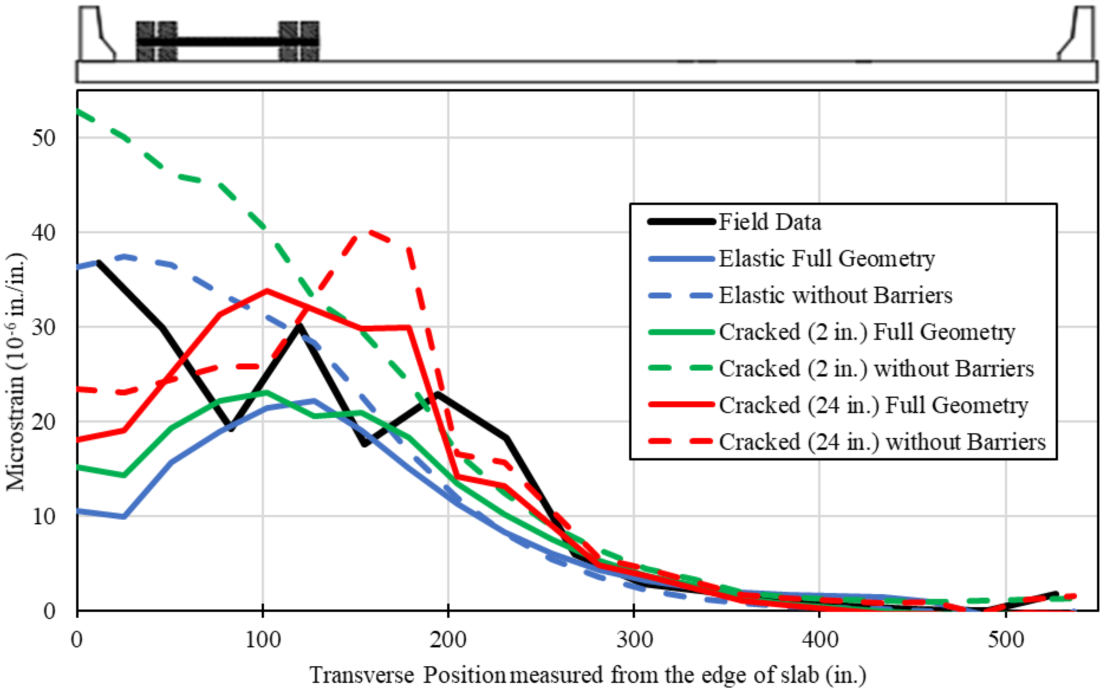

Figure 4.7: Strain generated by a 50-kip truck transversely positioned 1 ft from the barrier with the rear axle at midspan.

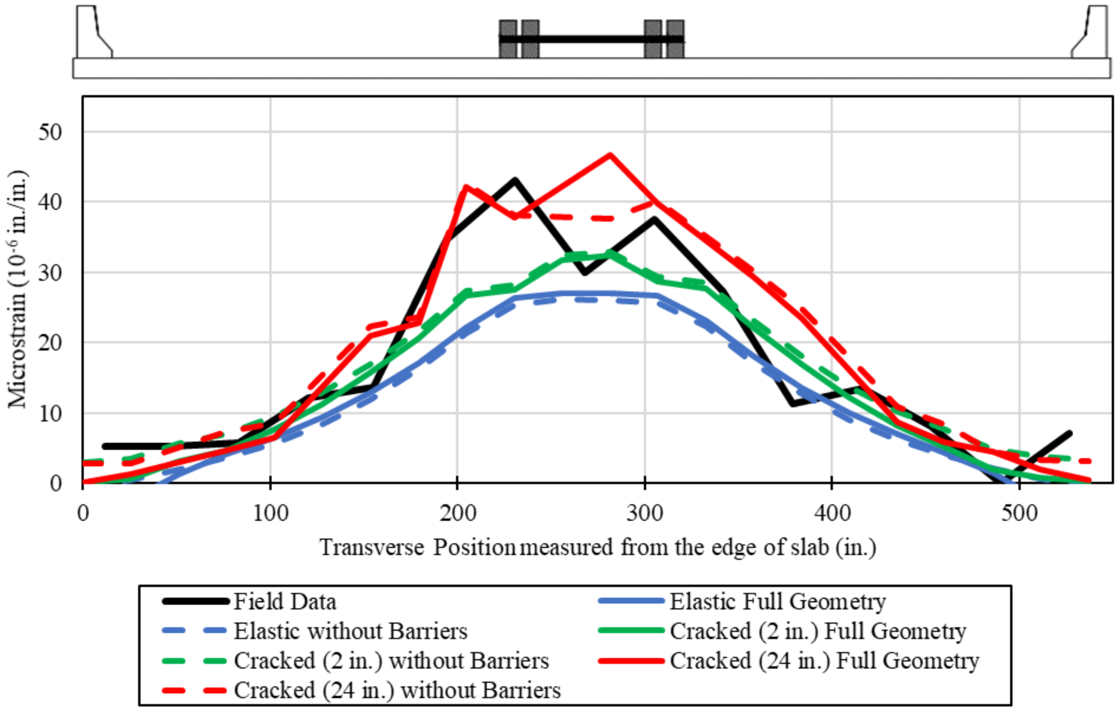

Figure 4.8: Strain generated by a 50-kip truck transversely positioned near the centerline of the structure with the rear axle at midspan.

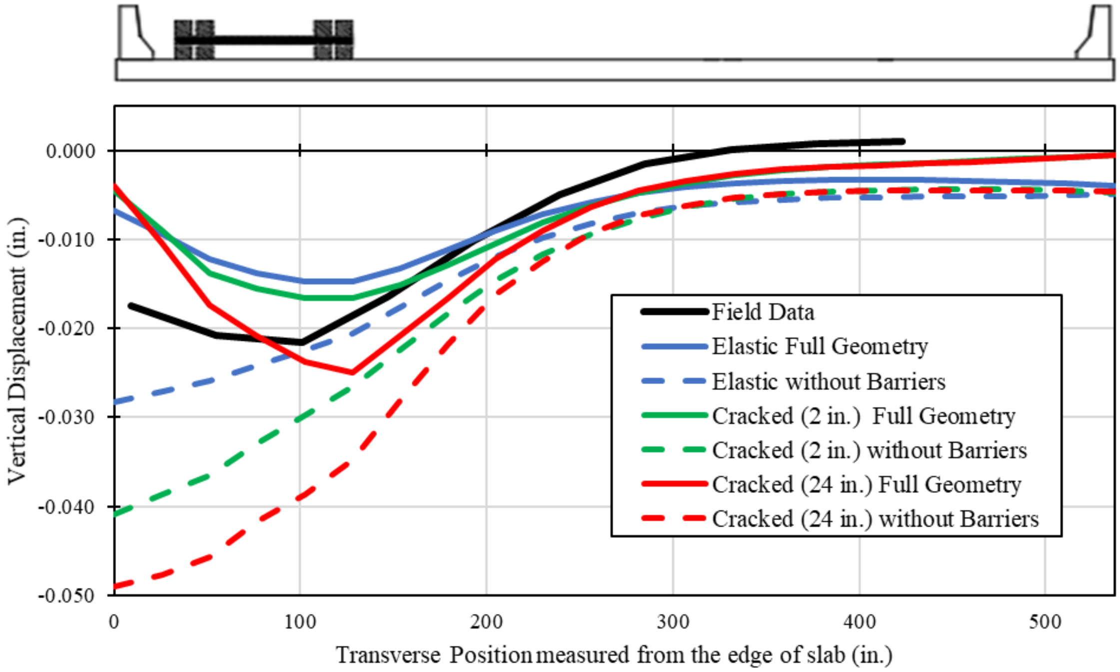

Figure 4.9: Vertical displacement generated by a 50-kip truck transversely positioned 1 ft from the barrier with the rear axle at midspan.

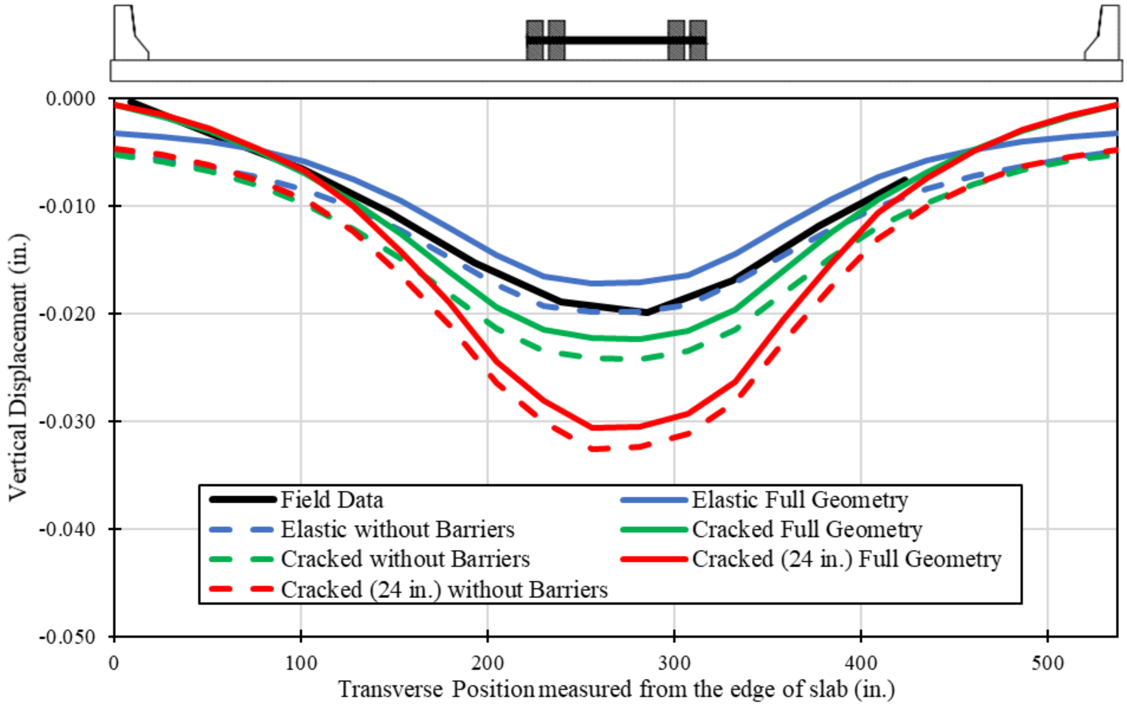

Figure 4.10: Vertical displacement generated by a 50-kip truck transversely positioned near the centerline of the structure with the rear axle at midspan.

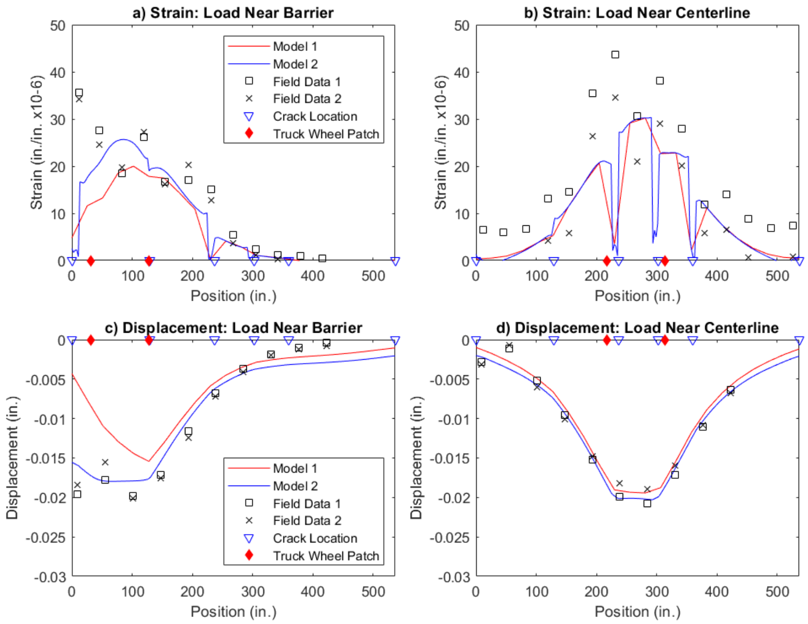

Figure 4.11: A comparison of Model 1 results, Model 2 results, and field data obtained from two repeat truck tests at each position for (a) strain measured with load near the barrier, (b) strain measured with load near the centerline, (c) displacement measured with load near the barrier, and (d) displacement measured with load near the centerline.

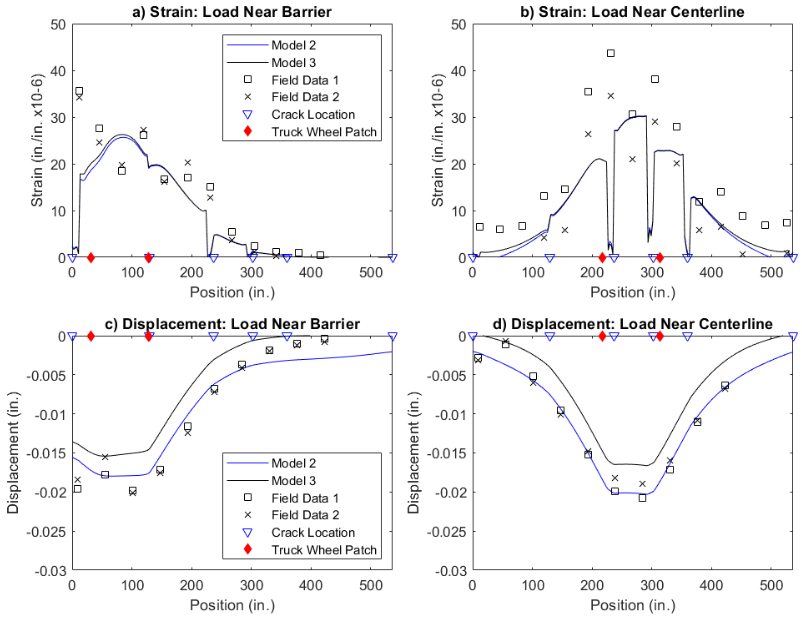

Figure 4.12: A comparison of Model 2 results, Model 3 results, and field data obtained from two repeat truck tests at each position for (a) strain measured with load near the barrier, (b) strain measured with load near the centerline, (c) displacement measured with load near the barrier, and (d) displacement measured with load near the centerline.

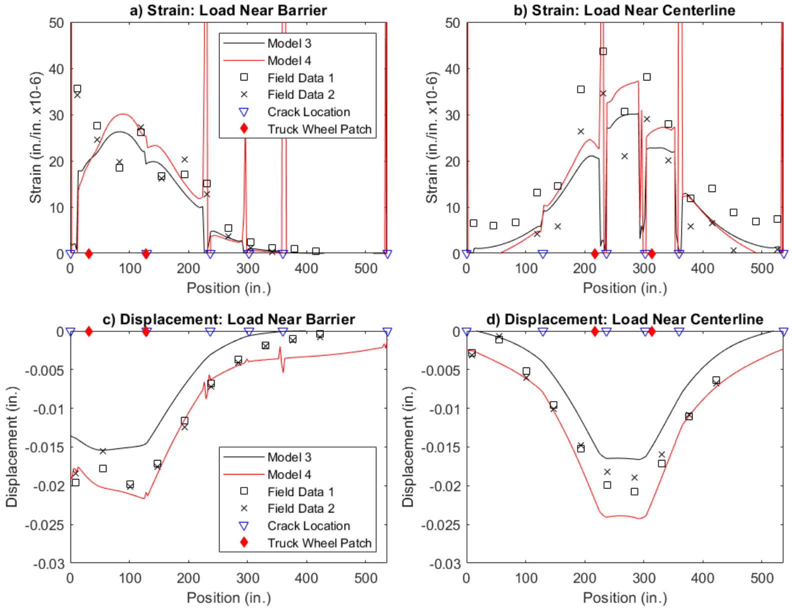

Figure 4.13: A comparison of Model 3 results, Model 4 results, and field data obtained from two repeat truck tests at each position for (a) strain measured with load near the barrier, (b) strain measured with load near the centerline, (c) displacement measured with load near the barrier, and (d) displacement measured with load near the centerline.

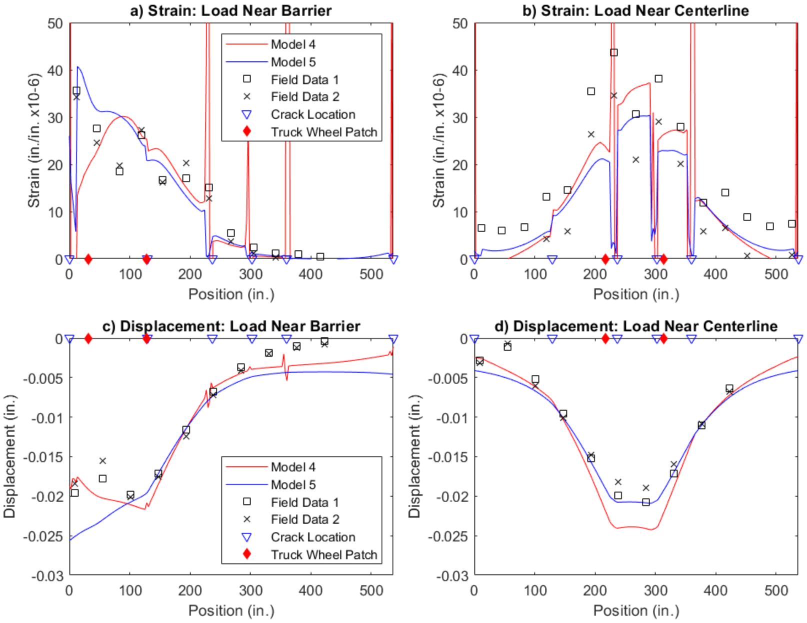

Figure 4.14: A comparison of Model 4 results, Model 5 results, and field data obtained from two repeat truck tests at each position for (a) strain measured with load near the barrier, (b) strain measured with load near the centerline, (c) displacement measured with load near the barrier, and (d) displacement measured with load near the centerline.

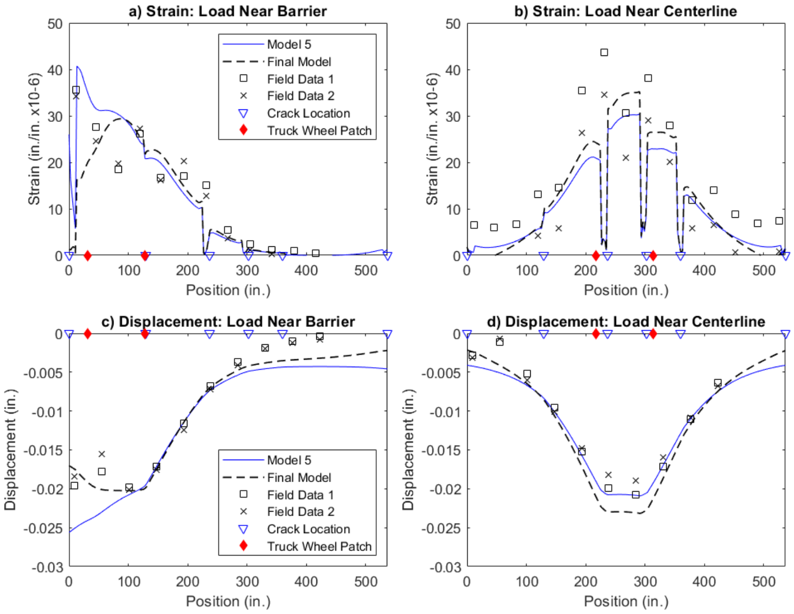

Figure 4.15: A comparison of Model 5 results, Final Model results, and field data obtained from two repeat truck tests at each position for (a) strain measured with load near the barrier, (b) strain measured with load near the centerline, (c) displacement measured with load near the barrier, and (d) displacement measured with load near the centerline.

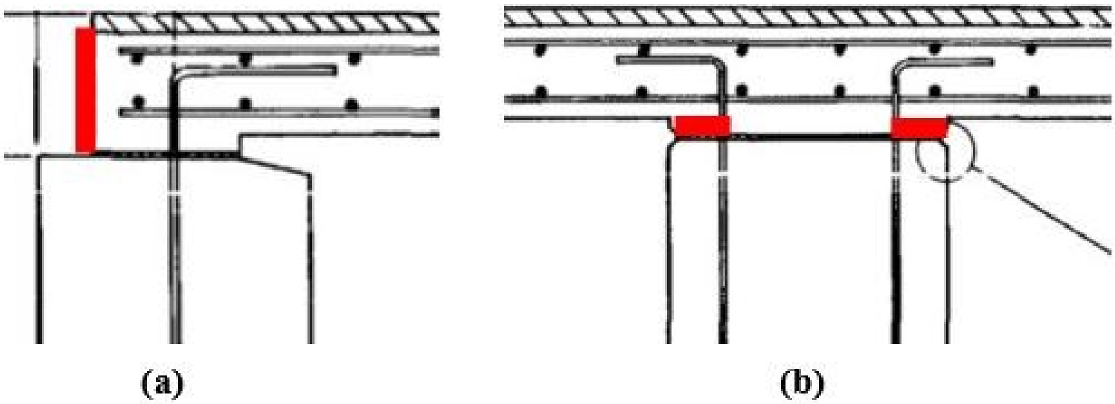

Figure 4.16: Location of the (a) fixed support condition at the outside edge of the abutment and (b) dual 10-in. wide pinned connections at each edge of the intermediate pier in the validated plate model. The connection locations are highlighted with red rectangles.

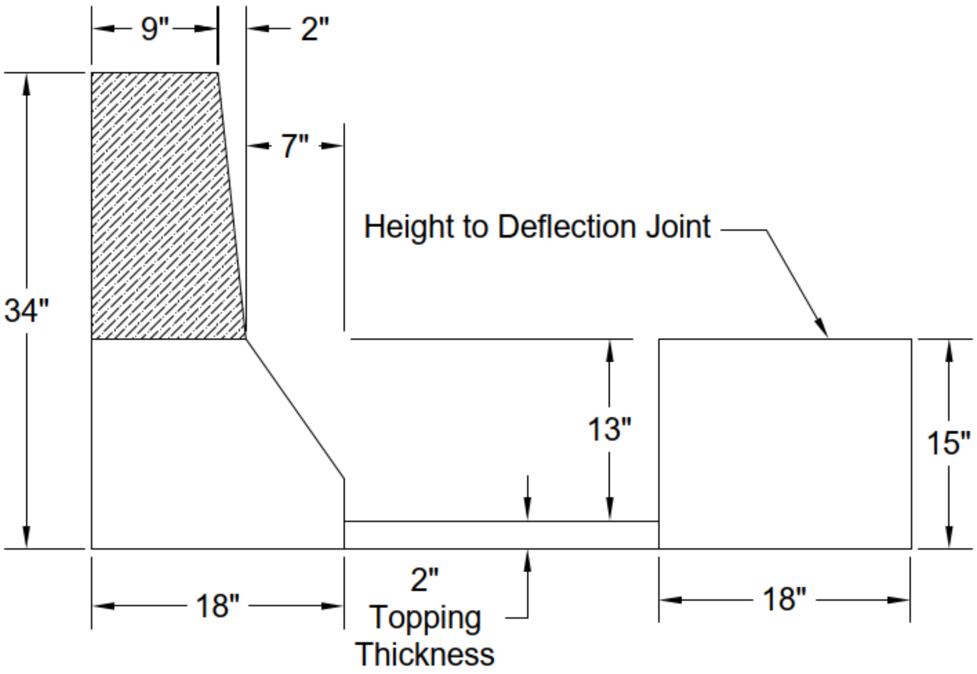

(a) (b)

Figure 4.17: Geometry of the (a) FEM Type J railing and (b) plate model rectangular beam-element barrier.

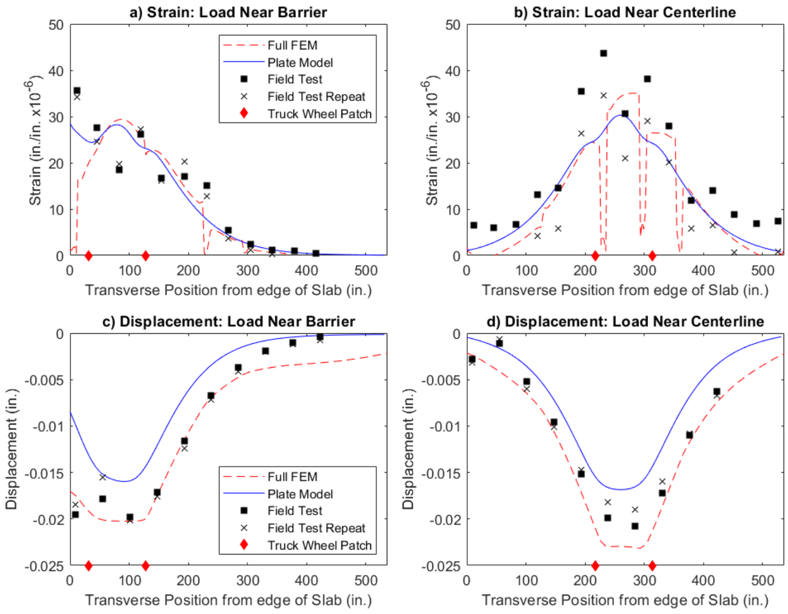

Figure 4.18: A comparison of plate model and FEM results to field data obtained from two repeat truck tests on Bridge 27926 for (a) strain measured with load near the barrier, (b) strain measured with load near the centerline, (c) displacement measured with load near the barrier, and (d) displacement measured with load near the centerline.

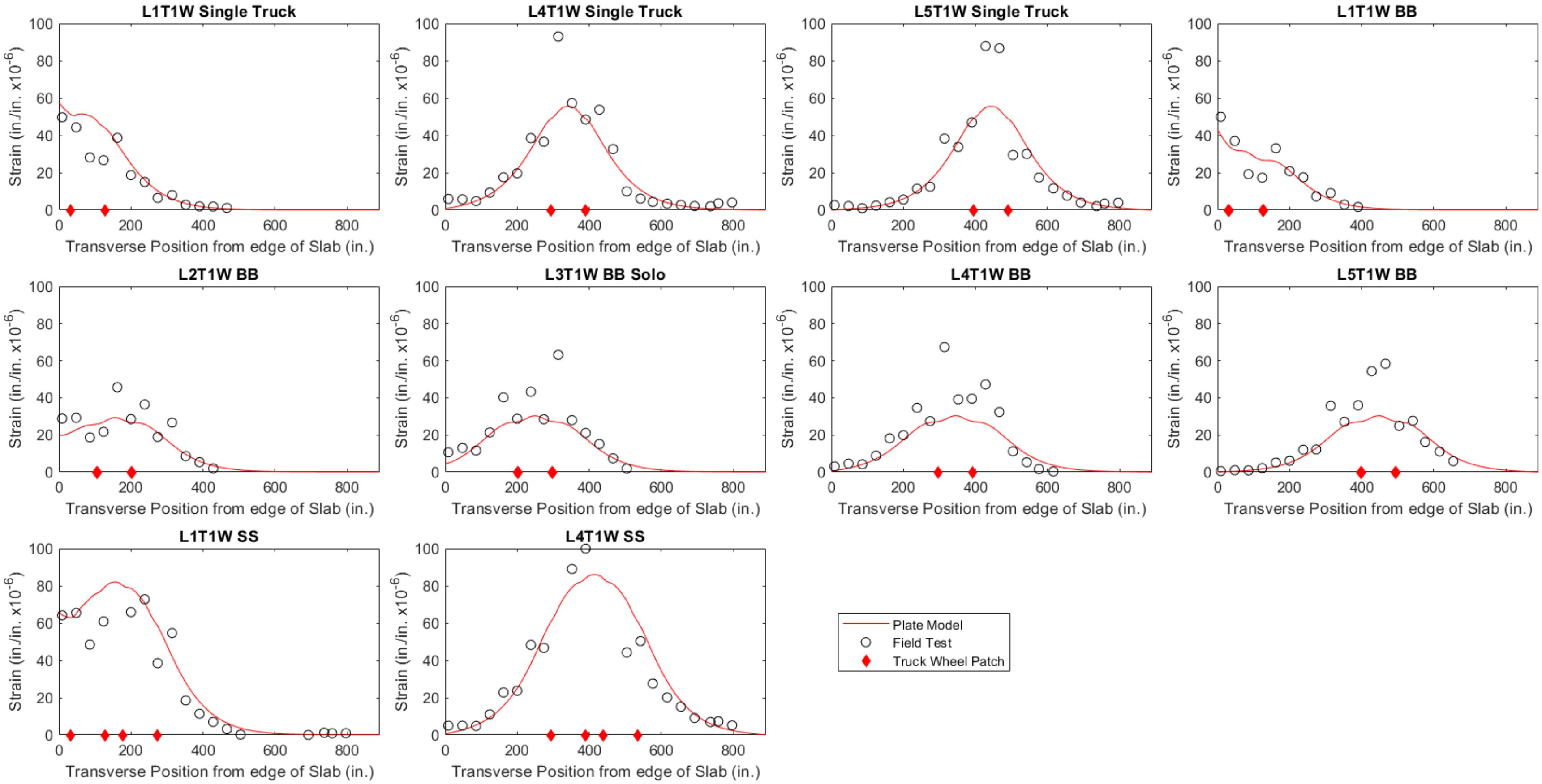

Figure 4.19: Strain results from the Bridge 27925 plate model using orthotropic elasticity properties with a reduced modulus in the x-direction (transverse) and y-direction (longitudinal).

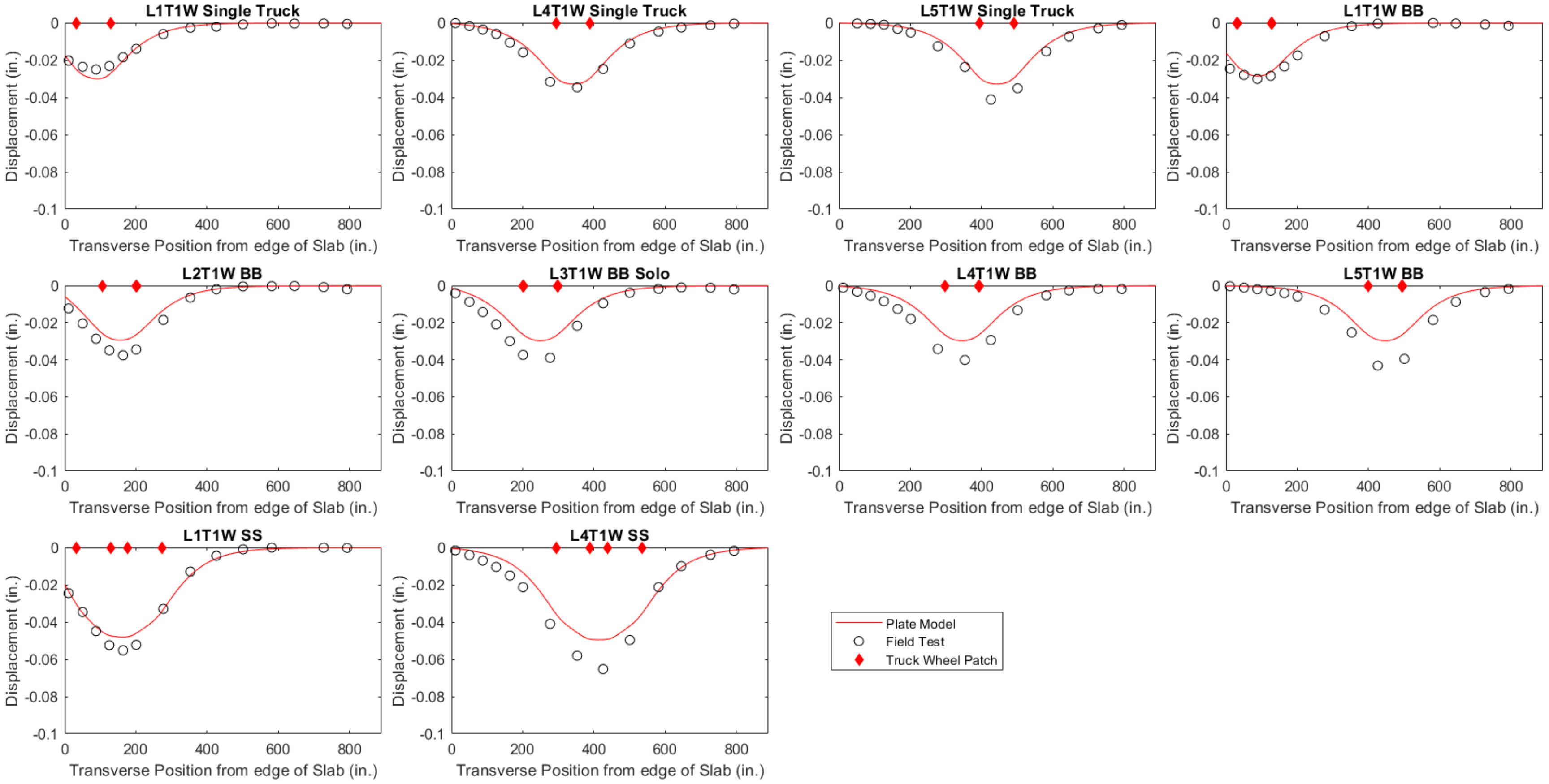

Figure 4.20: Displacement results from the Bridge 27925 plate model using orthotropic elasticity properties with a reduced modulus in the x-direction (transverse) and y-direction (longitudinal).

CHAPTER 5: RESULTS

The updated and validated FEM and plate model were used in combination with field data to determine the load distribution in the primary structure (Bridge 27926). The validated plate model and field data were also used to determine the load distribution in the secondary structure (Bridge 27925). Load distribution is presented in terms of the equivalent width and a live load distribution factor. LLDFs were generated using field data, FEM results, and plate model results. These LLDF values are compared to similar values obtained using the AASHTO LRFD (2020) equations. Finally, the current AASHTO LRFD (2020), AASHTO MBE (2018c), and AASHTO Standard Specifications (2002) flexural operating load ratings for Bridge 27926 were obtained from AASHTOWare and are compared to those calculated using the field data, validated FEM results, and plate model results.

5.1 EQUIVALENT WIDTH CALCULATION METHODS

The load distribution in a slab-span bridge is related to the equivalent width (*E*). In the literature, strain data are typically used to obtain equivalent widths from field testing, but displacement data can also be used and are less sensitive to localized cracking. For example, Crabtree et al. (2021) used the displacement at the location of interest divided by the sum of displacements across the span to determine equivalent widths in slab-span bridges. In this report, a parametric study considering aspect ratios (bridge width-to-span length) ranging from one to two, geometry, and material properties was conducted to confirm that displacement data could be used for equivalent width calculations. Results from the parametric study (Appendix C) indicated that the equivalent width was similar when leveraging strain or displacement data. Thus, the equivalent width was calculated using both strain and displacement data from the field tests, FEM results, and plate model results; the equivalent width was calculated using the area method described by Jones et al. (2012) as shown mathematically in Equation 5.1.

$$E = \frac{A_\varepsilon - A_t}{R_{max}} + w_t \qquad 5.1$$

Where E is the equivalent width (in.), A_ε is the area under the strain or displacement curve taken across the width of the bridge (in.), A_t is the area under the strain or displacement curve between the truck wheel patches (in.), R_{max} is the maximum strain or displacement sensor reading, and w_t is the width of the truck (in.).

Figure 5.1(a) shows an example cross-sectional strain profile that can be split into the area between the truck tire patches (A2) as well as the areas under the curve to the left (A1) and right (A3) of the axle. The area between the truck tire patches (A2) is defined by the known axle width (96 in. in this study) and the maximum sensor reading, which is strain in this case. In this study, the trapezoidal method was used to approximate the A1 and A3 areas that incorporate a curved line. The area of A1 and A3 are added together and divided by the maximum sensor reading (strain in this figure) to yield the equivalent total width of A1 and A3 together. The combined equivalent width of A1 and A3 was added to the width of the truck to determine the total equivalent width (*E*) of slab that is carrying the load.

An example of the area method from this study is shown in Figure 5.2 with strain data from a 50-kip, 96-in. wide truck transversely located at the centerline of a cross section that was near midspan of an end span on Bridge 27926. Figure 5.2(a) shows the areas A1 and A3 in red and blue, respectively; the maximum strain reading was approximately 40 με. The areas highlighted in Figure 5.2(a) were added together for a total A1+A3 area, divided by the maximum strain reading to determine the width beyond the truck axle, and added to the truck axle width to obtain the total equivalent width, *E*. This process was repeated for each truck test; detailed strain and displacement area method result plots are provided in Appendix J for Bridge 27926 and in Appendix K for Bridge 27925. Each *E* value was categorized as a single lane truck test (one truck) or multilane truck test (two side-by-side trucks). These two categories were subdivided into exterior strips (truck at edge of roadway and near the barrier) and interior strips (truck not near the edge of the roadway and away from the barrier). In this study, multilane *E* values derived from computational results or field data were divided by two to account for the fact that two side-by-side trucks were used to generate the sensor data.

The AASHTO LRFD (2020) and Standard Specifications (2002) provide equations for determining the equivalent width for non-skewed slab-type bridges. AASHTO LRFD equivalent width values can be obtained from Equation 5.2 for single (interior) lane loaded cases, Equation 5.3 for exterior strips (carrying one wheel path), and Equation 5.4 for multilane loaded cases. Equivalent width values calculated using the AASHTO Standard Specifications for a single wheel path can be obtained from Equation 5.5. For comparison to computational results or field data, the values derived from Equation 5.3 or Equation 5.5 were multiplied by two to account for the fact that truck axles include two wheel paths per lane. The values obtained for equivalent width from these equations for Bridge 27926 are shown in Table 5.1 using the geometry shown in Figure 3.1 and Figure 3.2.

$$E = 10 + 5\sqrt{L_1 W_1} \qquad 5.2$$

$$E = D + 12 + \frac{E_{min}}{4} \qquad 5.3$$

$$E = 84 + 1.44\sqrt{L_1 W_1} \leq 12\frac{W}{N_L} \qquad 5.4$$

$$b_{eff} = 4 + 0.06S \qquad 5.5$$

Where *E* is the equivalent width (in.), L_1 is the span length (ft) less than or equal to 60 ft; W_1 is the bridge width (ft) less than or equal to 30 ft for single lane loading and 60 ft for multilane loading; *W* is the actual bridge width (ft); N_L is the number of lanes taken as the road width divided by 12 ft/lane; *D* is the distance from edge to inside of barrier (in.); E_{min} is the minimum value obtained from Equation 5.2 or 5.4 (in.); b_{eff} is the distribution width for one wheel path (ft); and S is the span length (ft).

5.2 EQUIVALENT WIDTH AND LIVE LOAD DISTRIBUTION FACTORS

Equivalent width values were calculated with Equation 5.1 using both strain and displacement from the FEM results, plate model results, and field data. The results of the equivalent width analyses, LLDFs, and an AASHTO comparison are presented in Table 5.2, Table 5.3, and Table 5.4 for Bridge 27926 and Table 5.5, Table 5.6, and Table 5.7 for Bridge 27925. Single lane FEM and plate model results were generated with trucks transversely positioned either at 1 ft from the barrier or at the cross-sectional centerline, which correspond to similar loading scenarios used during field testing. In the field, trucks were located at these positions more than one time to gather individual responses and an average response. Therefore, field results shown in Table 5.2 and Table 5.5 correspond to both the minimum equivalent width from a single truck test (most conservative) and the average equivalent width considering all the repeat truck tests. The field testing values for multilane *E* shown in Table 5.2 and Table 5.5 were generated using data gathered when two side-by-side trucks positioned 1 ft apart were on the bridge; thus, the computed values were divided by two for comparison with the AASHTO LRFD multilane *E*, which represents the equivalent width per loaded lane. The FEM and plate model multilane equivalent widths were generated using 4-ft spacing between two side-by-side trucks, which is consistent with AASHTO LRFD requirements for spacing.

The AASHTO LRFD *E* was conservative (smaller) compared to FEM, plate model, and field results, except when compared to minimum *E* values from field tests for multilane loading; the minimum multilane *E* obtained from the field strain data was approximately 1 ft less than the LRFD value. This discrepancy is likely because the two trucks were positioned only 1 ft apart during the field tests whereas results from the FEM, plate model, and AASHTO all assumed the standard transverse truck spacing of 4 ft. Because the *E* calculation is dependent on the combined width of the trucks, the multilane *E* from field tests could be 5 in. wider than the value reported in Table 5.2 and Table 5.5 to account for the additional spacing that was not provided between the two side-by-side trucks. If this 5 in. were included, most values of *E* obtained from field testing are greater than AASHTO LRFD values for Bridge 27926. Table 5.3 and Table 5.6 show the increase in equivalent width when using strain or displacement data from the FEM (Bridge 27926 only), plate model, or field compared to the AASHTO LRFD Bridge Design Specifications (2020).

The field tests for single truck conditions show conservatism in the AASHTO equivalent width equations for Bridge 27926. The extent of conservatism was as low as 11% and as high as 57% for interior strips and strain data. The range was smaller using displacement data (43% to 55%). The conservatism was as low as 31% and as high as 44% for exterior strips and strain data. The range was 59% to 65% for displacement data. The model results show similar increases in equivalent width compared to AASHTO. Larger increases were exhibited in the interior strips of the FEM using displacement data and plate model using strain and displacement data (84%, 60%, and 65%, respectively). A 93% increase in exterior strip equivalent width was exhibited in the FEM using displacement data.

Equivalent width values are converted to a LLDF to determine the portion of the live load from one lane of traffic that is estimated to be carried by a 1-ft strip of slab. For slab-span bridges, the LLDF is equal to the inverse of the equivalent width, *E*, converted to feet as shown in Equation 5.6.

$$\mathrm{LLDF} = {}^{12}/_{E} \qquad 5.6$$

The LLDFs calculated using equivalent width values from the AASHTO LRFD Bridge Design Specifications (2020), FEM results, plate model results, and field data are presented in Table 5.4 and Table 5.7 for Bridge 27926 and Bridge 27925, respectively.

The plate model was the simplest and most efficient method for determining load distribution in the slab-span structures. The plate model also provided *E* (and therefore LLDF) values that were similar to those generated using results from the detailed FEM and field test data, but the plate model did not require rigorous or laborious input. Field tests require instrumentation, personnel, and possible road closures. Field testing is beneficial because it provides confidence in the behavior of the structure under known loading conditions. Field testing coupled with a detailed finite element model can be used to extrapolate behavior from loading conditions that are not practical in the field. However, full FEMs require significant time to input and develop the model as well as more computational time to run. In this study, the magnitude and shape of the FEM results were representative of the data collected from the field and provided further corroboration for the plate modeling technique.

5.3 FLEXURAL LOAD RATING FACTORS

Flexural load ratings are expressed as a rating factor. Flexural operating rating (OR) factors correspond to the maximum permissible live load to which a bridge may be subjected. Equation 5.7 and Equation 5.8 show the equations used to calculate rating factors in accordance with the LFR and LRFR methods, respectively.

$$\mathrm{RF} = \frac{C_M - A_1 D}{A_2 L(1 + IM)} \qquad 5.7$$

$$\mathrm{RF} = \frac{C_S - \gamma_{DC} DC - \gamma_{DW} DW \pm \gamma_P P}{\gamma_L LL(1 + IM)} \qquad 5.8$$

Where RF is the rating factor; C_M is the member capacity; *D* is the dead load effects on the member; A_1 is the factor for the dead loads; A_2 is the factor for the live loads; *L* is the live load effects on the member; *IM* is the dynamic load allowance used with the live load effect; C_S is the structural capacity; *DC* is the dead load effect of structural components and attachments; γ_{DC} is the load factor for structural components and attachments; *DW* is the dead load effect of wearing surfaces and utilities; γ_{DW} is the load factor for wearing surfaces and utilities; *P* is the permanent loading other than dead loads; γ_P is the load factor for permanent loads other than dead loads; *LL* is the live load effect; and γ_L is the evaluation live load factor (AASHTO, 2018).

The live load demand used in the LRFR methodology consists of the AASHTO HL-93 design load from the AASHTO LRFD Bridge Design Specifications (2020), which includes both the HS20 truck and a distributed lane load. The live load demand used in the LFR method includes either the HS20 truck load or the distributed lane load from the AASHTO Standard Specifications (2002). Once the load effect being evaluated is selected, the capacity of the structure is also determined. To compute the member rating in the LRFR and LFR methods, the rating factor is multiplied by the weight of the truck used to determine the live load effects (AASHTO, 2018). The bridge rating should be checked for each component and the overall bridge rating is typically controlled by the component with the lowest rating factor.

5.3.1 Effect of Material Properties on Flexural Capacity

The flexural capacity of a bridge component directly affects the rating factor. The flexural capacity of a one-foot strip of slab was calculated using the equivalent rectangular stress block approximation to determine how use of the design material properties versus in-situ measured material properties affected the slab capacity. The slab capacity was determined based on the design process outlined in the MnDOT LRFD Design Manual (2020a). The flexural resistance was calculated using Equations 5.9 through 5.12.

$$a = \frac{A_s f_y}{0.85 f'_c d} \tag{5.9}$$

$$c = \frac{a}{\beta_1} \tag{5.10}$$

$$\phi = min(\, 0.75 + 0.15(\frac{d}{c} - 1), 0.9) \tag{5.11}$$

$$M_r = \phi A_s f_y (d - \frac{a}{2}) \tag{5.12}$$

Where a is the depth of the equivalent rectangular stress block (in.), A_s is the area of tension reinforcement (in.^{2}), f_y is the yield strength of reinforcement (ksi), f'_c is the compressive strength of concrete (ksi), d is the effective depth of the member defined as the distance between the extreme compression fiber and the centroid of the tension reinforcement (in.), c is the distance from the extreme compression fiber to the neutral axis (in.), ϕ is the resistance factor, and M_r is the factored flexural resistance (capacity) (kip-in.). The value of M_r using design material properties for a one-foot strip of slab was 36 kip-ft and the value of M_r using measured material properties was 51 kip-ft. Using measured material properties over design material properties results in a 41% increase in moment capacity of a 1-ft strip of the structure.

5.3.2 AASHTOWare Operating Rating Factors for Primary Bridge 27926

AASHTOWare was used to calculate flexural OR factors for Bridge 27926 based on the AASHTO MBE (2018), design material properties, and using both the HS20 truck for LFR analysis and the HL-93 design load for LRFR analysis. The slab-span bridges crossing Shingle Creek are currently rated with Equation 5.7 (LFR method), which yields an OR factor for Bridge 27926 of 1.542, which is the equivalent to a HS-30.6 truck compared to the HS20 design truck (Dumbeck, 2019c). However, rating Bridge 27926 with Equation 5.8 (LRFR method), which is used to rate new bridges, results in a lower rating factor (below unity) as shown in Table 5.8. Additionally, separate LRFR load ratings were generated with the AASHTO LRFD distribution factors for comparison using the following material properties:

1. Design: analysis using the design concrete compressive strength, concrete elastic modulus, steel yield strength, and steel elastic modulus.
2. Measured*: analysis using the measured concrete elastic modulus, steel yield strength, and steel elastic modulus with the design concrete compressive strength. The measured concrete compressive strength was excluded from this analysis as it was significantly higher than the design strength, even considering additional strength gain over time as documented in the literature (French et al., 2010; Russian et al., 2020; Wood, 1992; Azizinamini & Choobineh, 1995). Further sampling would be required to verify that this was not anomalous.
3. Measured**: analysis using the measured concrete compressive strength, concrete elastic modulus, steel yield strength, and steel elastic modulus.

The measured material properties were presented in Table 3.1 and Table 3.2. Using the design and measured material properties during separate analyses was done to observe the resulting impact on the LRFR load rating. The flexural OR factors from AASHTOWare corresponding to the different equivalent widths (Table 5.1) and material properties are shown in Table 5.8 for Bridge 27926. The single lane and multilane rating factors reported in Table 5.8 were the lowest rating factors considering each span of the bridge.

The load rating results in Table 5.8 indicate that Bridge 27926 has a flexural operating rating factor less than unity when using AASHTO LRFD load distribution factors and design material properties, which indicates capacity lower than demand. Switching to the measured material properties for concrete and steel reinforcement (excluding concrete compressive strength) resulted in a 44% increase in load rating (via an increase in capacity), while using all the measured material properties resulted in a 58% increase in load rating.

5.3.3 AASHTOWare Operating Rating Factors for OSOW Trucks

Three oversize overweight truck configurations that are not allowed to cross the Shingle Creek bridges were provided by MnDOT. These vehicles currently must take a detour around the Shingle Creek bridges but could be allowed to cross if the OR factor is increased above unity for the structures. The axle weights and configurations for the Standard C+, Maximum, and Op2 trucks are shown in Table 5.9 and Figure 5.3.

These truck configurations were defined in AASHTOWare to obtain OR factors. The LLDFs shown in Table 5.4 and Table 5.7 for Bridge 27926 and 27925, respectively, calculated from the AASHTO LRFD Bridge Design Specifications (2020) using computational model results and field data were input in AASHTOWare for separate analyses. The AASHTOWare analyses used design material properties for both structures. The AASHTOWare load rating results for the HL-93 loading and the three OSOW trucks are presented in Table 5.10. The Bridge 27926 OR values for single lane interior strips are summarized below:

- ORs from field testing were 1.20 using either strain or displacement data for the Maximum axle configuration, 1.23 using either strain or displacement data for the OP2 axle configuration, and 1.44 using either strain or displacement data for the Standard C+ axle configuration.

- ORs using the plate model were 1.25 using strain or 1.28 using displacement results for the Maximum axle configuration, 1.28 using strain or 1.31 using displacement results for the OP2 axle configuration, and 1.50 using strain or 1.53 using displacement results for the Standard C+ axle configuration.

The Bridge 27925 OR values for single lane interior strips are summarized below:

- ORs from field testing were 1.09 using strain or 1.19 using displacement data for the Maximum axle configuration, 0.995 using strain or 1.09 using displacement data for the OP2 axle configuration, and 1.04 using strain or 1.12 using displacement data for the Standard C+ axle configuration.

- ORs using the plate model were 1.19 using strain or 1.18 using displacement results for the Maximum axle configuration, 1.09 using strain or 1.08 using displacement results for the OP2 axle configuration, and 1.12 using either strain or displacement results for the Standard C+ axle configuration.

Each type of rating load generated an OR greater than or equal to unity for Bridge 27926 and Bridge 27925 using rating factors from the plate model and design material properties for single lane interior strips (except for two values of 0.995 for Bridge 27925 and the Op2 truck configuration, which are very near unity). A single lane interior strip was considered because it corresponds to an OSOW truck crossing the bridge away from the barrier near a driving lane. Results from the plate modeling technique were considered because it was the easiest to implement and results showed similar behavior when compared to field test data. When LLDFs for exterior strips or multilane conditions were analyzed, the Maximum and OP2 axle configurations had ORs less than unity, which would indicate that those two trucks could not cross the slab-span bridges even if the rating factors had increased.

5.3.4 Summary of Flexural Operating Rating Factors

The ORs obtained from field test data, plate model results, and FEM results presented in Table 5.10 (using design material properties) are compared to the corresponding AASHTO LRFD ORs as a ratio in Table 5.11. The overall change in OR factor is proportional for each truck with the same LLDF; therefore, the ratio indicating increase or decrease in OR factor for the three OSOW is the same as the corresponding ratio of change for the HL-93 load. For example, the HL-93 loading and each of the three OSOW trucks analyzed all have a ratio of field OR to LRFD OR equal to 1.55 for interior lane loading on Bridge 27926. The field, plate, and FEM ORs are all greater than the AASHTO LRFD ORs for interior and exterior lanes for both structures. The field strain ORs for Bridge 27926 and 27925 are less than the AASHTO LRFD ORs for multilane loading (OR ratio of 0.98), which is due to the decreased truck spacing during field tests mentioned in Section 5.2. Since the plate modeling technique was the easiest to implement, use of the plate model multilane ORs is the most conservative (lowest) increase in OR. The multilane OR ratio using plate model strain data had an increase of 24% and 20% for Bridge 27926 and Bridge 27925, respectively. Similar magnitude multilane rating factor increases have been observed in the literature. Davids et al. (2013) observed a 25.5% increase in multilane rating factors for modeled slab-span bridges, and Jones et al. (2012) observed a 30% increase in multilane rating factors for field tested slab-span bridges. However, that level increase does not mean that the individual OR for each of the OSOW trucks is greater than unity for the multilane loading condition. Individual ORs calculated using plate model strain results for the OSOW trucks were greater than unity considering interior or exterior lane loading conditions.

Table 5.1: Equivalent width (E) from AASHTO LRFD (2020) and AASHTO Standard (STD) Specifications (2002).

AASHTO Method	Equivalent Width (E) (in.)	
	Bridge 27926	Bridge 27925
LRFD Single Interior Lane Loaded (Eq. 5.2)	143	143
LRFD Exterior Strip × 2 wheel paths per lane (Eq. 5.3)	129	135
LRFD Multilane Loaded (Eq. 5.4)	131	144
STD Single Wheel Path × 2 wheel paths per lane (Eq. 5.5)	130	130

Table 5.2: Equivalent width (E) values from the AASHTO LRFD Bridge Design Specifications, FEM results, plate model results, and field data considering both strain (ε) and displacement (Δ) for Bridge 27926.

Lane Loading	Equivalent Width (E) (in.)								
	LRFD	FEM		Plate		Field			
		ε	Δ	ε	Δ	Min. ε	Avg. ε	Min. Δ	Avg. Δ
Single Exterior	129	174	249	189	199	170	186	206	214
Single Interior	143	202	263	229	236	159	224	204	222
Multilane	131	150	179	164	161	117[*]	129[*]	142[*]	142[*]

[*] The starred values would be 122, 134, 147, and 147 in., respectively, if the additional 5 in. multilane spacing were included.

Table 5.3: Ratios comparing equivalent width (E) values calculated using the AASHTO LRFD Bridge Design Specifications (2020) to those from FEM results, plate model results, and field data considering both strain (ε) and displacement (Δ) for Bridge 27926.

Lane Loading	FEM E / LRFD E		Plate E / LRFD E		Field E / LRFD E			
	ε	Δ	ε	Δ	Min. ε	Avg. ε	Min. Δ	Avg. Δ
Single Exterior	1.35	1.93	1.46	1.54	1.31	1.44	1.59	1.65
Single Interior	1.41	1.84	1.60	1.65	1.11	1.57	1.43	1.55
Multilane	1.15	1.36	1.25	1.23	0.89	0.98	1.08	1.08

Table 5.4: Live load distribution factors (LLDFs) from the AASHTO LRFD Bridge Design Specifications (2020), FEM results, plate model results, and field data considering both strain (*ε*) and displacement (Δ) for Bridge 27926.

Lane Loading	LRFD	FEM		Plate		Field			
		ε	Δ	*ε*	Δ	Min. *ε*	Avg. *ε*	Min. Δ	Avg. Δ
Single Exterior	0.093	0.069	0.048	0.063	0.060	0.071	0.058	0.065	0.056
Single Interior	0.084	0.046	0.046	0.052	0.051	0.075	0.059	0.054	0.054
Multilane	0.092	0.080	0.067	0.073	0.075	0.103	0.085	0.093	0.085

Table 5.5: Equivalent width (*E*) values from the AASHTO LRFD Bridge Design Specifications, plate model results, and field data considering both strain (*ε*) and displacement (Δ) for Bridge 27925.

Lane Loading	Equivalent Width *E* (in.)						
	LRFD	Plate		Field			
		ε	Δ	Min. ε	Avg. ε	Min. Δ	Avg. Δ
Single Exterior	135	206	205	174	206	161	222
Single Interior	143	275	265	125	205	208	270
Multilane	144	170	166	111[*]	135[*]	97[*]	150[*]

[*] The starred values would be 116, 140, 102, and 155 in., respectively, if the additional 5 in. multilane spacing were included.

Table 5.6: Ratios comparing equivalent width (*E)* values calculated using the AASHTO LRFD Bridge Design Specifications (2020) to those from plate model results and field data considering both strain (*ε*) and displacement (Δ) for Bridge 27925.

Lane Loading	Plate *E* / LRFD *E*		Field *E* / LRFD *E*			
	ε	Δ	Min. *ε*	Avg. *ε*	Min. Δ	Avg. Δ
Single Exterior	1.53	1.52	1.29	1.53	1.19	1.64
Single Interior	1.92	1.85	0.87	1.43	1.45	1.89
Multilane	1.18	1.15	0.77	0.94	0.67	1.04

Table 5.7: Live load distribution factors (LLDFs) from the AASHTO LRFD Bridge Design Specifications (2020), plate model results, and field data considering both strain (*ε*) and displacement (Δ) for Bridge 27925.

Lane Loading	LRFD	Plate		Field			
		ε	Δ	Min. *ε*	Avg. *ε*	Min. Δ	Avg. Δ
Single Exterior	0.089	0.058	0.059	0.069	0.058	0.075	0.054
Single Interior	0.084	0.044	0.045	0.096	0.059	0.058	0.044
Multilane	0.083	0.071	0.072	0.108	0.089	0.124	0.080

Table 5.8: AASHTOWare flexural operating rating (OR) factors for Bridge 27926.

E Source (rating method)	Material Properties	Rating Load	Controlling OR (Truck+Lane)	Difference from AASHTO LRFD with Design Material Properties
AASHTO STD (LFR)	Design	HS20-44	1.542 (Axle Load)	—
AASHTO LRFD (LRFR)	Design	HL-93	0.96	0%
AASHTO LRFD (LRFR)	Measured*	HL-93	1.38	+44%
AASHTO LRFD (LRFR)	Measured**	HL-93	1.52	+58%

*The design concrete compressive strength of 4 ksi was used in addition to the measured concrete elastic modulus of 3725 ksi, steel yield strength of 80.4 ksi, and steel modulus of elasticity of 29,800 ksi.

**The measured concrete compressive strength of 9.48 ksi was used in addition to the measured concrete elastic modulus of 3725 ksi, steel yield strength of 80.4 ksi, and steel modulus of elasticity of 29,800 ksi.

Table 5.9: HL-93 and OSOW truck axle weights and configurations provided by MnDOT.

Axle Number	HL-93		Standard C+		Maximum		Op2	
	Axle Weight (kip)	Distance to next axle (ft)	Axle Weight (kip)	Distance to next axle (ft)	Axle Weight (kip)	Distance to next axle (ft)	Axle Weight (kip)	Distance to next axle (ft)
1	8	14	15	10	15	15.167	15	10
2	32	14 to 30	20	4	20	4.5	20	4
3	32	—	20	4	20	4.5	20	4
4			20	4	20	8.08	20	4
5			20	23	20	4.5	20	20
6			20	4	20	4.5	20	4
7			20	4	20	32	20	4
8			20	4	20	4.5	20	4
9			20	—	20	4.5	20	35
10					20	12.167	20	4
11					20	4.5	20	4
12					20	4.5	20	4
13					20	—	20	—

Table 5.10: Bridge 27926 and 27925 AASHTOWare flexural operating rating (OR) factors for interior and exterior strips considering both strain (ε) and displacement (Δ) for the AASHTO LRFD HL-93 loading and three OSOW trucks using the material properties in AASHTOWare specified by MnDOT.

LLDF Source	Lane Loading	OR Factors Separated by Rating Load and Data Type							
		HL-93		Maximum		Op2		Standard C+	
		ε	Δ	ε	Δ	ε	Δ	ε	Δ
Bridge 27926									
LRFD	Interior	1.04	—	0.78	—	0.79	—	0.93	—
	Exterior	0.94	—	0.70	—	0.72	—	0.84	—
	Multilane	0.96	—	0.72	—	0.73	—	0.86	—
Field	Interior	1.61	1.61	1.20	1.20	1.23	1.23	1.44	1.44
	Exterior	1.34	1.56	1.00	1.16	1.02	1.19	1.20	1.39
	Multilane	0.94	1.02	0.70	0.77	0.72	0.78	0.84	0.92
Plate	Interior	1.67	1.71	1.25	1.28	1.28	1.31	1.50	1.53
	Exterior	1.38	1.45	1.03	1.08	1.06	1.11	1.24	1.30
	Multilane	1.19	1.16	0.89	0.87	0.91	0.89	1.07	1.04
FEM	Interior	1.89	1.89	1.41	1.41	1.45	1.45	1.69	1.69
	Exterior	1.26	1.81	0.94	1.36	0.97	1.39	1.13	1.62
	Multilane	1.09	1.30	0.81	0.97	0.83	0.99	0.97	1.16
Bridge 27925									
LRFD	Interior	1.04	—	0.78	—	0.79	—	0.93	—
	Exterior	1.04	—	0.78	—	0.79	—	0.93	—
	Multilane	1.00	—	0.75	—	0.77	—	0.89	—
Field	Interior	1.32	1.40	1.09	1.19	0.995	1.09	1.04	1.12
	Exterior	1.32	1.34	1.09	1.12	1.00	1.03	1.05	1.07
	Multilane	0.98	1.09	0.73	0.81	0.75	0.83	0.88	0.91
Plate	Interior	1.40	1.39	1.19	1.18	1.09	1.08	1.12	1.12
	Exterior	1.32	1.32	1.09	1.09	1.00	0.995	1.05	1.04
	Multilane	1.21	1.20	0.92	0.90	0.91	0.92	0.94	0.94

Table 5.11: Ratios of field, plate, and FEM operating rating (OR) factors to AASHTO LRFD OR factors for Bridge 27926 and 27925; the ratios are independent of rating load type.

LLDF Source	Lane Loading	Field, Plate, or FEM OR / AASHTO OR	
		ε	Δ
Bridge 27926			
Field	Interior	1.55	1.55
	Exterior	1.43	1.66
	Multilane	0.98	1.07
Plate	Interior	1.61	1.65
	Exterior	1.48	1.55
	Multilane	1.24	1.21
FEM	Interior	1.83	1.83
	Exterior	1.35	1.94
	Multilane	1.13	1.35
Bridge 27925			
Field	Interior	1.27	1.35
	Exterior	1.27	1.29
	Multilane	0.98	1.08
Plate	Interior	1.35	1.34
	Exterior	1.27	1.27
	Multilane	1.20	1.20

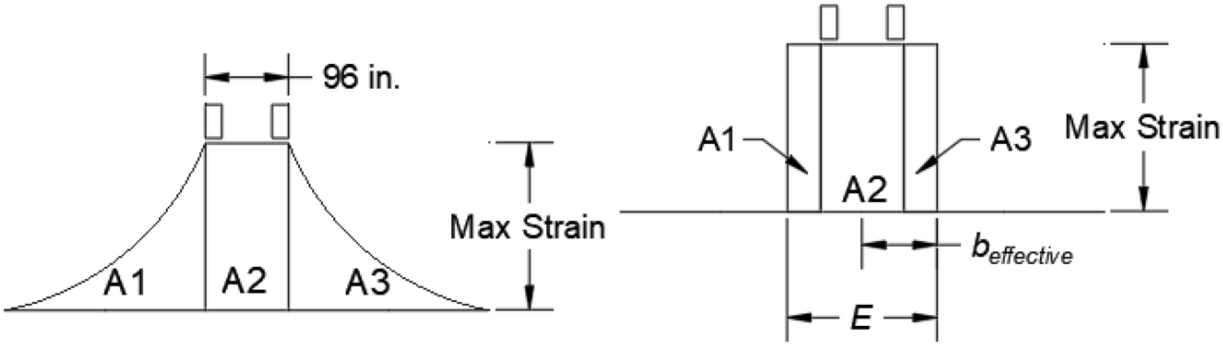

(a) **(b)**

Figure 5.1: Visualization of the area method for calculating equivalent width (*E*) that uses (a) the cross-sectional strain profile and (b) the equivalent rectangular area determined while keeping the maximum sensor reading (strain) constant.

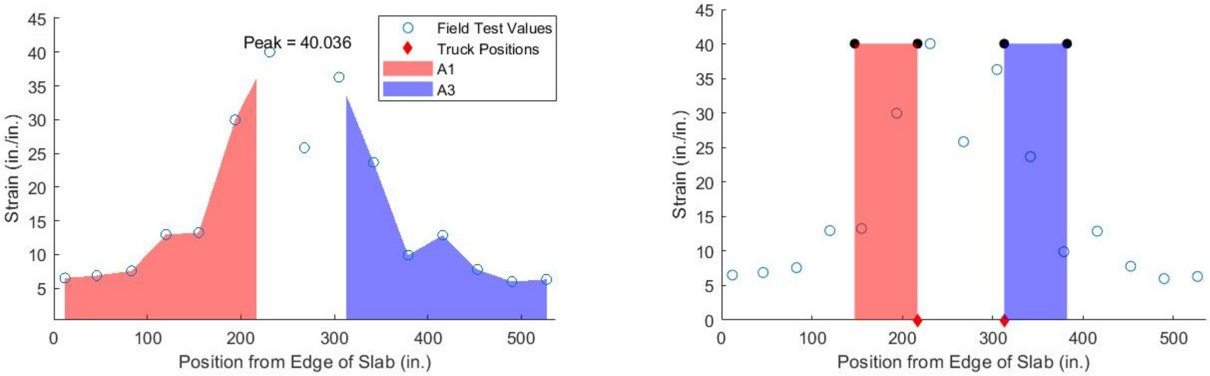

(a) **(b)**

Figure 5.2: Equivalent width visualization using strain data gathered when a truck was positioned at the centerline of an end span on Bridge 27926; (a) shows the cross-sectional strain profile and (b) shows the equivalent areas determined while keeping the maximum strain sensor reading constant.

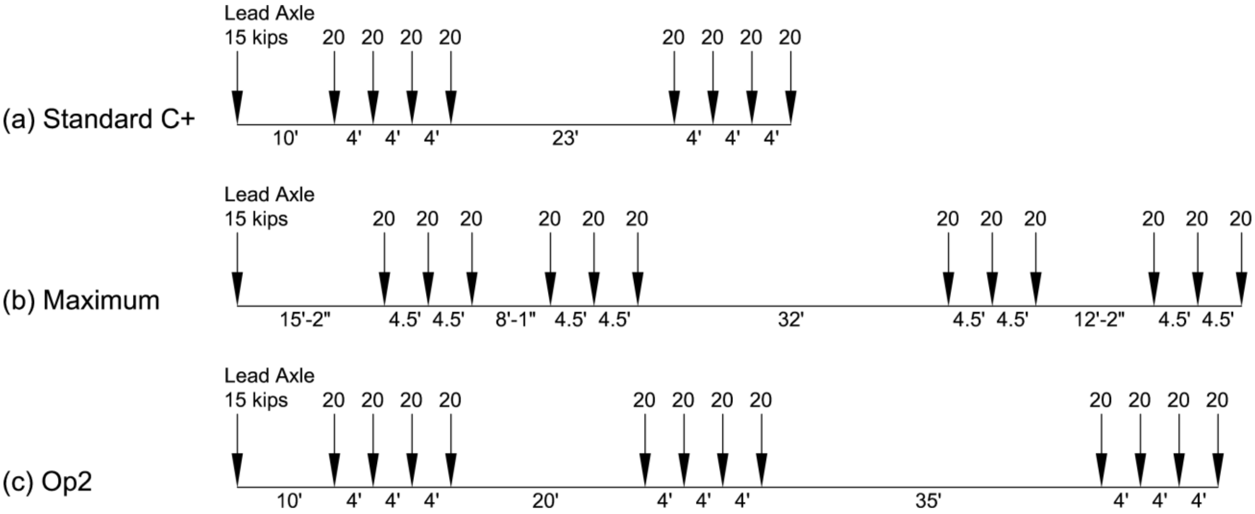

Figure 5.3: Axle weights (kips) and spacings (ft-in.) for the (a) Standard C+, (b) Maximum, and (c) Op2 OSOW configurations.

CHAPTER 6: CONCLUSIONS, GUIDANCE, AND RECOMMENDATIONS

Equivalent width results from field data and computational model results indicated conservatism in the AASHTO Specification equations. This has been corroborated by numerous studies in the literature (Amer et al., 1999; Azizinamini et al., 1994a; Azizinamini & Choobineh, 1995; Chung C. Fu; Maged Elhelbawey; M. A. Sahin; David R. Schelling, 1996; Davids et al., 2013; Dorton et al., 1976; Hays et al., 1986; Huria et al., 1993; Jáuregui et al., 2010; E. Lantsoght, 2019; Mabsout et al., 2004; Peiris et al., 2019; Saraf, 1998; Shahrooz et al., 1994; Sherman et al., 2020; Zokaie et al., 1991b). This result was expected and prompted the study. Operating rating factors obtained from the *E* calculation methods, modeling techniques, and field testing described in previous chapters were greater than those generated using LLDFs calculated with the AASHTO LRFD Bridge Design Specifications, except for the LLDFs obtained from the multilane field tests. The results of this study have also shown that the design material properties for concrete compressive strength, steel reinforcing modulus of elasticity, and steel reinforcing yield strength were not representative of the in-situ material properties for the primary bridge. Increasing select material property values in AASHTOWare from those specified during design to those measured from field samples provided a 44% increase in load rating related to the slab-span capacity. Since the measured concrete compressive strength (9.48 ksi) was significantly higher than the design value (4 ksi), more field samples should be obtained and tested before using the measured concrete compressive strength to calculate the load rating. However, FEM results indicated that load distribution was marginally affected by changing material properties from design to measured.

The contribution of barriers to load distribution in the Shingle Creek bridges was investigated. Through the parametric study shown in Appendix C, computational model results, and field test data, it was determined that the barriers behaved as rectangular beam elements with (1) a cross-sectional area approximately equal to the width at the barrier base times a height from the base to the deflection joint and (2) an elastic modulus equal to the modulus measured from field samples (the design modulus was approximately 3.5% less than the modulus observed in field samples). Effects of barriers were largely confined to exterior design strips; changing barrier parameters had little effect on the behavior of the interior design strips for Bridge 27926.

Additional studies using the plate model recommendations and field data collected from Bridge 27925 were conducted to determine if the same conditions could be applied to structures with different aspect ratios. The width-to-length aspect ratio of the end spans of Bridge 27926 was 1.9 while the corresponding aspect ratio for Bridge 27925 was 3.1. For Bridge 27926, decreasing either the longitudinal or the transverse modulus of elasticity by an amount related to the ratio of the cracked moment of inertia to the gross moment of inertia increased the equivalent width; only the transverse modulus of elasticity value was reduced to match displacement data gathered during field testing. However, both the longitudinal and transverse modulus of elasticity were reduced in the plate model of Bridge 27925 to match strain profiles, displacement profiles, and equivalent width values generated with field data. In addition to the different aspect ratios, this distinction between the plate models of the two bridges could have also been required due to the slightly worse (2%) condition state of the reinforced concrete slab of Bridge 27925.

Use of the LLDFs from the plate model and design material properties resulted in an operating rating factor that was greater than that generated using AASHTO LRFD LLDFs for the HL-93 multilane loading by 24% for Bridge 27926 and 20% for Bridge 27925. However, that level of increase did not mean that the individual OR for each of the OSOW trucks was greater than unity for the multilane loading condition. Individual ORs calculated using plate model strain results for the OSOW trucks were greater than unity considering interior or exterior lane loading conditions.

Based on these considerations, it is recommended that load rating of the Shingle Creek slab-span structures be conducted using LLDFs obtained from a plate model constructed as described in Chapter 4. The plate modeling technique is simple to deploy and efficient considering time to build and run; use of design material properties is recommended because they are readily available and do not require destructive field sampling. If the three OSOW trucks are routed across the Shingle Creek bridges, it is recommended that the vehicles cross near the transverse centerline of the structure and without other vehicles present (single interior lane loading). This recommendation is based on equivalent width and live load distribution factor results for interior single-lane loading scenarios considering strain and displacement results from the plate model. This recommendation does not consider the peak load demand that may occur if the bridge is loaded with the OSOW trucks.

6.1 LOAD RATING PROCESS

This section outlines the steps to calculate load ratings for slab-span bridges based on a linear elastic plate model. Furthermore, details for Bridge 27926 are included as an example.

- Create the geometry of the plate in the finite element software following the as-built plans for the slab thickness and span lengths.
    - For Bridge 27926, the slab thickness was 13 in., the two end spans were each 23 ft 7 in., and the middle span was 24 ft 2 in.
- Provide boundary conditions for the slab at the support locations. Pinned connections are provided at the interior supports where the vertical reinforcement passed from the pier to the slab. Fixed connections are provided at the ends of the slab. All boundary conditions are applied across the entire width (i.e., transverse direction) of the bridge.
    - For Bridge 27926, two pinned connections were provided at each pier 10 in. from either edge of the pier and along the entire transverse length of the pier. The ends of the slab were fixed along the entire transverse length of the slab.
- Approximate the barriers as a rectangle with a height equal to the distance from the top of the roadway to the deflection joint and width equal to the width of the base of the barrier.
    - For Bridge 27926, a beam element with height of 13 in. and width of 18 in. was modeled along the centerline of the actual barrier location (11 in. from the edge of the slab in the direction of traffic).

- Use design material properties from as-built plans for concrete modulus of elasticity unless material samples from the structure are available for testing. Use Poisson's ratio equal to 0.2.
    - For Bridge 27926, the measured concrete modulus of elasticity of 3725 ksi was used in the plate model.
- Select axle loads based on one of the following: the truck used for field testing, the design vehicle, or the rating vehicle. Select loading locations that will produce maximum moments in the structure. Transversely, consider single-lane interior, single-lane exterior, and multilane conditions. Longitudinally, consider the locations desired for rating, such as midspan for positive moment or over a support for negative moment.
    - For Bridge 27926, axle weights and spacings from the 50-kip MnDOT dump truck used during field testing (Table 3.3) were input as the plate model loading. The trucks were transversely positioned 1 ft from the barrier for single lane exterior, at the bridge centerline for single lane interior, and two side-by-side trucks were positioned at the centerline and spaced 4 ft apart for multilane conditions. Longitudinally, the truck was positioned to generate peak positive moment; the centerline of the rear tandem was 12 ft from the expansion joint where vehicles access the structure, and the front axle of the vehicle was oriented toward the middle span of the bridge.
- Evaluate the plate model for the given truck loading and collect strain and/or displacement results across the transverse width of the slab at the rating location(s). Self-weight (dead load) of the bridge need not be applied because the model is linear elastic and results are only needed for live load effects.
    - For Bridge 27926, strain and displacement results were collected at 100 points along a transverse cross section at the centerline of the rear tandem axles near midspan of an end span (i.e., 12 ft from the expansion joint).
- Calculate equivalent width following Section 5.1. Either strain or displacement results may be used (if using displacement, the user must account for negative values). Equation 6.1 is used for the equivalent width calculation.

$$E = \frac{A_\varepsilon - A_t}{R_{max}} + w_t \tag{6.1}$$

Where E is the equivalent width (in.), A_ε is the area under the strain or displacement curve taken across the width of the bridge (in.), A_t is the area under the strain or displacement curve between a single truck's wheel patches for single-lane cases or between the wheel patches of two trucks including the area between the trucks for multilane cases (in.), R_{max} is the maximum strain or displacement sensor reading, and w_t is the width of the truck (in.). Multilane equivalent width values should be divided by two to account for the use of two side-by-side trucks in the model loading.

- For Bridge 27926, both strain and displacement results were used with similar outcomes. The areas and maximum sensor readings varied based on the truck loading location. The truck axle width was 96 in.

- Obtain LLDF values by calculating the inverse of the equivalent width, *E*, converted to feet.
    - Table 6.1 shows the LLDF values for input into AASHTOWare for Bridge 27926 and Bridge 27925.
- Input LLDF values in AASHTOWare for single-lane exterior, single-lane interior, and multilane conditions. Use AASHTOWare to determine the equivalent OR for each lane loading scenario; determine the controlling OR.
    - Table 6.1 shows the LLDF values for input into AASHTOWare and the OR values output from AASHTOWare for Bridge 27926 and Bridge 27925.

Table 6.1: Bridge 27926 and 27925 live load distribution factors (LLDFs) from the plate model results used to generate flexural operating rating (OR) factors in AASHTOWare for interior and exterior strips considering both strain (ε) and displacement (Δ) for the AASHTO LRFD HL-93 loading and three OSOW trucks. The LLDFs and OR factors were generated using the material properties in AASHTOWare specified by MnDOT.

Lane Loading	Plate LLDF		OR Factors Separated by Rating Load and Data Type							
			HL-93		Maximum		Op2		Standard C+	
	ε	Δ	ε	Δ	ε	Δ	ε	Δ	ε	Δ
Bridge 27926										
Interior	0.063	0.060	1.67	1.71	1.25	1.28	1.28	1.31	1.50	1.53
Exterior	0.052	0.051	1.38	1.45	1.03	1.08	1.06	1.11	1.24	1.30
Multilane	0.073	0.075	1.19	1.16	0.89	0.87	0.91	0.89	1.07	1.04
Bridge 27925										
Interior	0.058	0.059	1.40	1.39	1.19	1.18	1.09	1.08	1.12	1.12
Exterior	0.044	0.045	1.32	1.32	1.09	1.09	1.00	0.995	1.05	1.04
Multilane	0.071	0.072	1.21	1.20	0.92	0.90	0.91	0.92	0.94	0.94

REFERENCES

AASHTO. (1973). *Standard Specifications for Highway Bridges*. Washington, DC: American Association of State Highway and Transportation Officials.

AASHTO. (1992). *Standard Specifications for Highway Bridges* (15th ed.). Washington, DC: American Association of State Highway and Transportation Officials.

AASHTO. (1994). *AASHTO LRFD Bridge Design Specifications* (1st ed.). Washington, DC: American Association of State Highway and Transportation Officials.

AASHTO. (1996). *Standard Specifications for Highway Bridges* (16th ed.). Washington, DC: American Association of State Highway and Transportation Officials.

AASHTO. (1998). *LRFD Design Specifications* (2nd ed.). Washington, DC: American Association of State Highway and Transportation Officials.

AASHTO. (2002). *Standard Specifications for Highway Bridges* (17th ed.). Washington, DC: American Association of State Highway and Transportation Officials.

AASHTO. (2003). *Manual for Condition Evaluation of Bridges* (2nd ed.). Washington, DC: American Association of State Highway and Transportation Officials.

AASHTO. (2010). *AASHTO LRFD Bridge Design Specifications*. Washington, DC: American Association of State Highway and Transportation Officials.

AASHTO. (2016). *The Manual for Bridge Evaluation with 2016 Interim Revisions* (2nd ed.). Washington, DC: American Association of State Highway and Transportation Officials.

AASHTO. (2017). *LRFD Bridge Design Specifications* (8th ed.). Washington, DC: American Association of State Highway and Transportation Officials. Retrieved from https://doi.org/10.1201/9780203946602.ch20

AASHTO. (2018a). *Manual for Bridge Evaluation 2018 Section 6: Load Rating* (3rd ed., pp. 6-1-6–193). Washington, DC: American Association of State Highway and Transportation Officials.

AASHTO. (2018b). Material Testing. In *AASHTO Manual for Bridge Evaluation 2018*. Washington, DC: American Association of State Highway and Transportation Officials.

AASHTO. (2018c). *The Manual for Bridge Evaluation* (3rd ed.). Washington, DC: American Association of State Highway and Transportation Officials.

AASHTO. (2020). *LRFD Bridge Design Specifications* (9th ed.). Washington, DC: American Association of State Highway and Transportation Officials.

Agardh, L. (1994). Impact Excitation of Concrete Highway Bridges. *Procedings from the 12th International Modal Analysis Conference*, *II*, 1329–1334.

Allemang, R. J. (2003). The modal assurance criterion — Twenty years of use and abuse. *Sound and Vibration*, *37*(8), 14–21.

Amer, A., Arockiasamy, M., & Shahawy, M. (1999). Load Distribution of Existing Solid Slab Bridges Based on Field Tests. *Journal of Bridge Engineering*, *4*(August), 189–193.

ASTM International. (2014). *ASTM C469/C469M-14, Standard Test Method for Static Modulus of Elasticity and Poisson's Ratio of Concrete*. Retrieved from https://doi.org/10.1520/C0469

ASTM International. (2018). C42/C42M -20 Standard Method of Test for Obtaining and Testing Drilled Cores and Sawed Beams of Concrete. In *AASHTO* (Vol. 1, p. 12). Retrieved from https://doi.org/10.1520/C0042_C0042M-20

ASTM International. (2019). *ASTM A370-19, Standard Test Methods and Definitions for Mechanical Testing of Steel Products.* Retrieved from https://doi.org/10.1520/A0370-14.2

ASTM International. (2020a). *ASTM C39/C39M-20, Standard Test Method for Compressive Strength of Cylindrical Concrete Specimens*. Retrieved from https://doi.org/10.1520/C0039

ASTM International. (2020b). *ASTM C42/C42M-20, Standard Test Method for Obtaining and Testing Drilled Cores and Sawed Beams of Concrete.* Retrieved from https://doi.org/10.1520/C0042

Avitabile, P. (2017). *Modal Testing: A Practitioner's Guide*. New York: John Wiley & Sons.

Azizinamini, A., & Choobineh, F. (1995). Rating Concrete Slab Bridges. *IABSE Reports*, *73*, 805–810.

Azizinamini, A., Shekar, Y., Barnhill, G., & Boothby, T. E. (1994a). Old Concrete Bridges Can They Carry Modern Traffic Loads? *Concrete International*, *16*(2), 64–69.

Azizinamini, A., Shekar, Y., Boothby, T. E., & Barnhill, G. (1994b). Old Concrete Slab Bridges. I: Experimental Investigation. *Journal of Structural Engineering (United States)*, *120*(11), 3305–3319. Retrieved from https://doi.org/10.1061/(ASCE)0733-9445(1994)120:11(3305)

Azizinamini, A., Shekar, Y., Boothby, T. E., & Barnhill, G. (1994c). Old Concrete Slab Bridges. II: Analysis. *Journal of Structural Engineering*, *11*, 3305–3319.

Bagheri, A., Alipour, M., Usmani, S., Ozbulut, O. E., & Harris, D. K. (2017). Online Systems Parameters Identification for Structural Monitoring. *Dynamics of Civil Structures, 2*(180), 243–249. https://doi.org/10.1007/978-3-319-54777-0

Chung, C. F., Elhelbawey, M., Sahin, M. A., & Schelling, D. R. (1996). Lateral Distribution Factor. *Bridge Fied Testing*, *122*(9), 1106–1109. Retrieved from https://ascelibrary.org/doi/epdf/10.1061/%28ASCE%290733-9445%281996%29122%3A9%281106%29

Conkel, D. (2019). *MnDOT State Aid Bridge Office 2019 Calendar Year — Bridge Cost Report.* St. Paul, MN: Minnesota Department of Transportation.

Crabtree, B., Ross, B. E., Cousins, T. E., & Ziehl, P. (2021). Live-Load Testing of Flat Precast Slab Bridge to Determine Joint Efficiency and Distribution Factors for Moment. *Journal of Performance of Constructed Facilities*, *35*(1), 04020134. Retrieved from https://doi.org/10.1061/(asce)cf.1943-5509.0001543

Csagoly, P. F., & Lybas, J. M. (1989). Advanced Design Method for Concrete Bridge Deck Slabs. *Concrete International*, *11*(5), 53–63.

Davids, W. G., Poulin, T. J., & Goslin, K. (2013). Finite-Element Analysis and Load Rating of Flat Slab Concrete Bridges. *Journal of Bridge Engineering*, *18*(10), 946–956. Retrieved from https://doi.org/10.1061/(asce)be.1943-5592.0000461

Densmore, D. H. (2000). *Load and Resistance Factor Design.* Retrieved from http://www.fhwa.dot.gov/bridge/062800.htm

Dorton, R. A., Holowka, M., & King, J. P. C. (1976). The Conestogo River Bridge design and testing. *Canandian Journal of Civil Engineering*. Retrieved from https://doi.org/10.1139/l77-003

Dragomiretskiy, K., & Zosso, D. (2014). Variational Mode Decomposition. *IEEE Transactions on Signal Processing*, *62*(3), 531–544. Retrieved from https://doi.org/10.1109/TSP.2013.2288675

Dumbeck, B. (2019a). *2019 Routine Bridge Inspection Report Bridge 27909*. St. Paul, MN: Minnesota Department of Transportation. Retrieved from https://www.drjtbc.org/default.aspx?pageid=2760

Dumbeck, B. (2019b). *2019 Routine Bridge Inspection Report Bridge 27925*. St. Paul, MN: Minnesota Department of Transportation.

Dumbeck, B. (2019c). *Minnesota Structure Inventory Report Bridge 27926*. St. Paul, MN: Minnesota Department of Transportation.

Fang, I. K., Worley, J. A., Burns, N. H., & Klinger, R. E. (1986). *Behavior of Ontario-Type Bridge Decks on Steel Girders.* Austin, TX: University of Texas at Austin.

Farrar, C. R., Duffey, T. A., Cornwell, P. J., & Doebling, S. W. (1999). Excitiation Methods for Bridge Structures. In *Applied Modal Analysis: Reducing Time to Market*. Retrieved from https://doi.org/10.2307/j.ctt1ffjgnb.124

Fenwick, R. C., & Dickson, A. R. (1989). Slabs Subjected to Concentrated Loading. *ACI Structural Journal*, *86*(6), 672–678. Retrieved from https://doi.org/10.14359/2703

FHWA. (2018). *National Bridge Inventory.* Washington, DC: FHWA.

Freeman, C., & Vasconcelos, B. (2018). *Solid Concrete Slab Bridges Effective Width Recommendations*. Tallahassee, FL: Florida Department of Transportation.

French, C., Shield, D. C. K., & Dereli, O. (2010). *Discrepancies in Shear Strength of Prestressed Beams with Different Specifications*. Final Report #2010-03. St. Paul, MN: Minnesota Department of Transportation.

Google. (2020). *Google Maps directions illustrating I-494 Detour*. Retrieved from https://www.google.com/maps/dir/45.1076536,-93.4671939/44.9611245,-92.7760181/@44.9742619,-93.2463576,10.63z/data=!4m2!4m1!3e0

Hardyniec, A. B., Cousins, T. E., Roberts-Williams, C. L., & Sotelino, E. D. (2009). *Dynamic Testing and Modeling of a Superelevated Skewed Highway Bridge*. Blacksburg, VA: Virginia Polytechnic Institute and State University.

Hays, C. O., Sessions, L. M., & Berry, A. J. (1986). Further Studies on Lateral Load Distribution Using a Finite Element Method. *Transportation Research Record*, *1072*, 6–14.

Hsieh, K. H., Halling, M. W., & Barr, P. J. (2006). Overview of Vibrational Structural Health Monitoring with Representative Case Studies. *Journal of Bridge Engineering*, *11*(6), 707–715. Retrieved from https://doi.org/10.1061/(asce)1084-0702(2006)11:6(707)

Huria, V., Lee, K. L., & Aktan, A. E. (1993). Nonlinear Finite Element Analysis of RC Slab Bridge. *Journal of Structural Engineering*, *119*(1), 88–107. Retrieved from https://doi.org/10.1061/(ASCE)0733-9445(1994)120:10(3081)

ISA & ICMC. (2015). *Grain Marketing: Moving Indiana's Economy.* Indianapolis, IN: Indiana Soybean Alliance and Indiana Corn Marketing Council.

Iyer, S. L. (1985). *Load Capacity of Older Continuous Concrete Slab Bridges*. Rapid City, SD: South Dakota School of Mines and Technology.

Jáuregui, D. V., Licon-lozano, A., & Kulkarni, K. (2010). Higher Level Evaluation of a Reinforced Concrete Slab Bridge. *Journal Of Bridge Engineering*, *15*(April), 172–182.

Jones, B. P., Shenton, H. W. I., Lewis, J., Wolfe, S., Faghri, A., Pletz, E., Lee, E., & Carter, M. (2012). *Effective Width of Concrete Slab Bridges in Delaware*. Newark, DE: Delaware Center for Transportation.

Juang, J. N., & Pappa, R. S. (1985). An Eigensystem Realization Algorithm for Modal Parameter Identification and Model Reduction. *Journal of Guidance, Control, and Dynamics*, *8*(5), 620–627. Retrieved from https://doi.org/10.2514/3.20031

Lantsoght, E. (2019). *Load Testing of Bridges: Current Practice and Diagnostic Load Testing*. (E. O. L. Lantsoght & D. M. Frangopol (eds.). Boca Raton, FL: CRC Press.

Mabsout, M., Tarhini, K., Jabakhanji, R., & Awwad, E. (2004). Wheel Load Distribution in Simply Supported Concrete Slab Bridges. *Journal of Bridge Engineering*, *9*(2), 147–155. Retrieved from https://doi.org/10.1061/(ASCE)1084-0702(2004)9:2(147)

MnDOT. (1980). *Bridge 27926 General Plan and Elevation* (State Proj). St. Paul, MN: Minnesota Department of Transportation.

MnDOT. (1988). *Bridge 27909 General Plan and Elevation* (State Proj). St. Paul, MN: Minnesota Department of Transportation.

MnDOT. (2018). *Bridge Load Rating and Evaluation Manual.* St. Paul, MN: Minnesota Department of Transportation.

MnDOT. (2020a). *LRFD Bridge Design Manual* (MnDOT Bridge Office (ed.)). St. Paul, MN: Minnesota Department of Transportation.

MnDOT. (2020b). *Superstructure Guidelines.* St. Paul, MN: Minnesota Department of Transportation.

NCHRP (National Cooperative Highway Research Program). (1998). *NCHRP 234 Manual for Bridge Rating Through Load Testing* (Issue NCHRP Project 12-28(13)A). Washington, DC: NCHRP.

Nelson, S. L. (2011). *Load Rating Report for Bridge 27909 Eastbound Trunk Highway 94 over Shingle Creek Hennepin County.* St. Paul, MN: Minnesota Department of Transportation.

Pastor, M., Binda, M., & Harčarik, T. (2012). Modal Assurance Criterion. *Procedia Engineering*, *48*, 543–548. Retrieved from https://doi.org/10.1016/j.proeng.2012.09.551

Peiris, A., Harik, I., Center, K. T., Cabinet, K. T., University of Kentucky, L., & Cabinet, K. T. (2019). *Bridge Load Testing Versus Bridge Load Rating.* Retrieved from https://doi.org/10.13023/ktc.rr.2019.16%0Ahttps://trid.trb.org/view/1671399%0Ahttps://rosap.ntl.bts.gov/view/dot/44084%0Ahttps://trid.trb.org/view/1693061

Russian, O., Belarbi, A., Feng, Q., & Dawood, M. (2020). Investigation of Material Properties for Load Rating of Historical Bridges. *Journal of Bridge Engineering*, *25*(4), 1–9. Retrieved from https://doi.org/10.1061/(ASCE)BE.1943-5592.0001540

Saraf, V. K. (1998). Evaluation of Existing RC Slab Bridges. *Journal of Performance of Constructed Facilities*, *12*(February), 20–24.

Sessions, L. M. (1985). *Load Testing of Three Bridges on Florida's Turnpike*. Tallahassee, FL: Florida Department of Transportation.

Shahrooz, B. M., Ho, I. K., Aktan, A. E., de Borst, R., Blaauwendraad, J., van der Veen, C., Iding, R. H., & Miller, R. A. (1994). Nonlinear Finite Element Analysis of Deteriorated RC Slab Bridge. *Journal of Structural Engineering*, *120*(2), 422–440. Retrieved from https://doi.org/10.1061/(asce)0733-9445(1994)120:2(422)

Sherman, R. J., Hebdon, M. H., & Lloyd, J. B. (2020). Diagnostic Load Testing for Improved Accuracy of Bridge Load Rating. *Journal of Performance of Constructed Facilities*, *34*(5), 1–9. Retrieved from https://doi.org/10.1061/(ASCE)CF.1943-5509.0001483

U.S. DOT FHWA, ICF Consulting, Lakshmanan, T. R., & Anderson, W. P. (2009). *Freight Transportation Improvements and the Economy.* Washington, DC: U.S. Department of Transportation Federal Highway Administration.

Wood, S. L. (1992). Evaluation of the Long-Term Properties of Concrete. In *ACI Materials Journal* (Vol. 88, Issue 6). Research and Development Bulletin RD102T. Retrieved from https://doi.org/10.14359/1201

Zokaie, T., Imbsen, R. A., & Osterkamp, T. A. (1991a). Distribution of Wheel Loads on Highway Bridges. *Transportation Research Record*, *1290*, 119-126.

Zokaie, T., Osterkamp, T. A., & Imbsen, R. A. (1991b). Distribution of Wheel Loads on Highway Bridges. *National Cooperative Highway Research Program Final Report*, *1*(12-26/1), 710.

APPENDIX A: PHOTOS OF SLAB-SPAN BRIDGES SPANNING SHINGLE CREEK

Figure A.1: Bridge 27909 from the East.

Figure A.2: Bridge 27926 from the East.

Figure A.3: Bridge 27925 from the East.

Figure A.4: North edge of Bridge 27909.

Figure A.5: South edge of Bridge 27926 (Primary testing structure).

Figure A.6: Cracking and spalling observed in the slab of Bridge 27909.

Figure A.7: Exposed steel reinforcement observed in Bridge 27909.

Figure A.8: Cracking and spalling observed in Bridge 27926.

Figure A.9: Abutment and barrier of Bridge 27909 from the South.

Figure A.10: Cracking observed in Bridge 27909.

Figure A.11: Expansion joint between Bridge 27909 and Bridge 27926.

Figure A.12: Deflection joint and barrier crack in Bridge 27926.

Figure A.13: Deflection joint and crack in barrier of Bridge 27925.

Figure A.14: Crack observed in Bridge 27925.

Figure A.15: Crack and spalling observed in Bridge 27925.

Figure A.16: Exposed steel reinforcement in Bridge 27925.

APPENDIX B: PHOTOS FROM SAMPLING AND TESTING TO QUANTIFY MATERIAL PROPERTIES

Figure B.1: MnDOT drill rig used for bridge deck coring.

Figure B.2: Drilling 1.75 in. cores from Bridge 27926.

Figure B.3: 1.75 in. core from Bridge 27926.

Figure B.4: 6 in. core bit.

Figure B.5: 6 in. cored holes in Bridge 27926.

Figure B.6: Aggregate-epoxy resin fill.

Figure B.7: Filled core hole.

Figure B.8: 1.75 in. core prepped for compression test.

Figure B.9: 4 in. core prepped for compression test.

Figure B.10: 4 in. core broken in compression.

Figure B.11: 4 in. core prepped for elastic modulus test.

Figure B.12: Epoxy coated steel reinforcement obtained from 6 in. cores from Bridge 27926.

Figure B.13: Steel reinforcement machined for tensile testing.

Figure B.14: Steel reinforcement during tensile test.

APPENDIX C: LOAD DISTRIBUTION PARAMETRIC STUDY RESULTS

A parametric study was conducted to determine if there is a relationship between strain load distribution and displacement load distribution. Simple 3-dimensional plate models were developed using Ansys Static Structural software with varying aspect ratios, edge supports, and loads. A total of nine analyses were conducted with the varied parameters. The results from each model were normalized to unity by dividing the results by the maximum magnitude of each test. The summation of the normalized results (Figure C.1) and the calculated equivalent widths (*E*) (Table C.1) from strain and displacement were compared for each analysis.

- **Analysis 1**: Simple model with aspect ratio width to length of 1, thickness of 12 in., modulus of elasticity of 3600 ksi, fixed on two opposite edges, single point 10-kip load at center.
- **Analysis 2**: Simple model with aspect ratio width to length of 2, thickness of 12 in., modulus of elasticity of 3600 ksi, fixed on two opposite edges, single 10-kip point load at center.
- **Analysis 3**: Simple model with aspect ratio width to length of 2, thickness of 12 in., modulus of elasticity of 3600 ksi, fixed on two opposite edges, single 10-kip point load at center, edge beams with width of 20 in. and height of 32 in.
- **Analysis 4**: Simple model with aspect ratio of width to length 2, thickness of 12 in., modulus of elasticity of 3600 ksi, fixed on two opposite edges, two 10-kip point loads 222.5 in. apart about center, edge beams with width of 20 in. and height of 32 in.
- **Analysis 5**: Simple model with aspect ratio of width to length 2, thickness of 12 in., modulus of elasticity of 3600 ksi, fixed on two opposite edges, two 10-kip point loads one at center and one at 111.25 in. offset from center, edge beams with width of 20 in. and height of 32 in.
- **Analysis 6**: Simple model with aspect ratio of width to length 2, thickness of 12 in., modulus of elasticity of 3600 ksi, fixed on two opposite edges, two 10-kip point loads 111.25 in. apart about center, edge beams with width of 20 in. and height of 32 in.
- **Analysis 7**: Simple model with three spans, single span aspect ratio of width to length 2, thickness of 12 in., modulus of elasticity of 3600 ksi, each span fixed at opposite edges, 10-kip point loads 111.25 in. apart about center.
- **Analysis 8**: Simple model with three spans, single span aspect ratio of width to length 2, thickness of 12 in., modulus of elasticity of 3600 ksi, each span fixed at opposite edges, 10-kip point loads 111.25 in. apart about center, edge beams with width of 20 in. and height of 32 in.
- **Analysis 9**: Simple model with three spans, single span aspect ratio of width to length 2, thickness of 12 in., modulus of elasticity of 3600 ksi, each span fixed at opposite edges, 10-kip point loads 96 in. apart and 30 in. from inside of edge beam, edge beams with width of 20 in. and height of 32 in.

The models with parameters resembling the slab-span bridges in the primary study had displacement results summations that were 27-30% greater than the strain results summation. This is similar to the results of the FEM equivalent width results (39% greater for exterior strips and 29% greater for interior strips). However, in the plate model the equivalent width results for displacement were within 3% of the equivalent width calculated from strain results. The similarity between displacement and strain equivalent width is shown to be less than or equal to 40% different at the most extreme.

When the equivalent width is calculated, the difference between strain and displacement results is reduced for two point loads compared to a simple summation of the normalized data. The 8th analysis run (interior strip) had a difference between *E* from strain and displacement of 24% and the 9th (exterior strip) analysis run had a difference between *E* from strain and displacement of 29%. The results are closer when calculating the actual *E* value compared to summing the results at each point across the bridge because the *E* calculation assumes a maximum value between the tire patches while the magnitude of the recorded strain values decreases at locations that were between tire patches in the model.

Based on the results of this parametric study, using displacement data from the field is a reliable method to estimate equivalent widths for slab-span bridges especially when conditions (cracking and spalling) limit the usefulness of strain gauges. The field data equivalent width for displacement in exterior strips was 15% greater than the strain equivalent width for exterior strips and the field data equivalent width for displacement in interior strips was 1% less than the field data equivalent width for strain in interior strips. The field test data indicate that *E* obtained from displacement data yields nearly identical results to *E* obtained using strain data. This is corroborated by the results of the parametric study and the modeling technique of the primary study which show *E* from strain and displacement approach the same values in the validated FEM and plate model. Modeling techniques negate this need and allow for strain results to be used in calculating *E* regardless of field conditions.

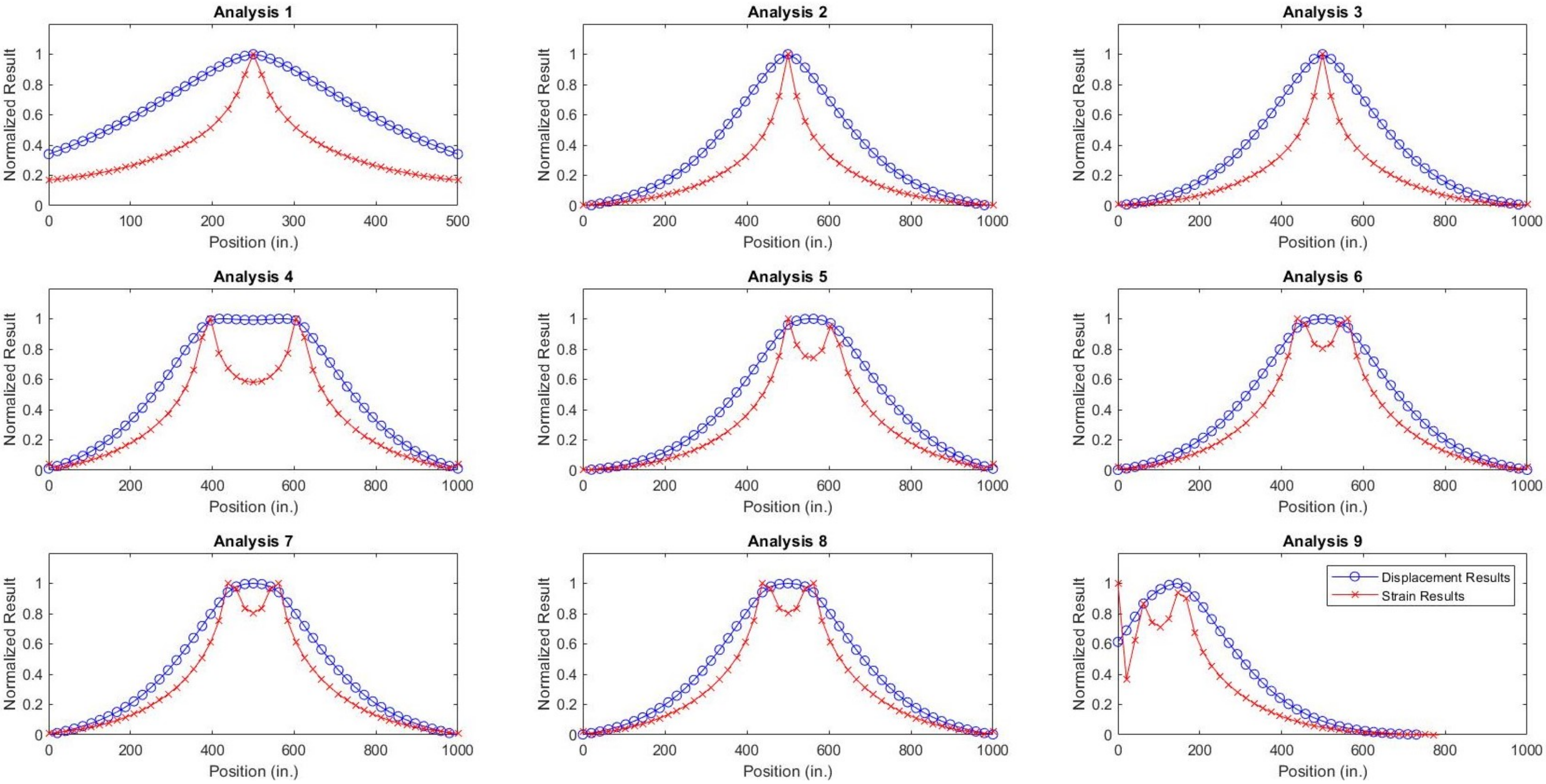

Figure C.1: Strain and displacement profiles normalized to a maximum of one to compare load distribution for each Ansys.

Table C.1: Equivalent widths from each test run using strain and displacement and comparison of displacement *E* divided by strain *E*.

Analysis Run	Strain *E* (in.)	Displacement *E* (in.)	Disp. *E* / Strain *E*	Disp. Sum / Strain Sum
1	187	332	1.78	1.779
2	194	356	1.84	1.836
3	192	354	1.84	1.841
4	421	521	1.24	1.459
5	321	411	1.28	1.390
6	330	408	1.24	1.282
7	333	412	1.24	1.280
8	330	408	1.24	1.282
9	238	307	1.29	1.347

APPENDIX D: TESTING PLANS FOR EACH BRIDGE

Table D.1: Test schedule page 1 for Bridge 27926 on June 6, 2021.

Time Increment	Actual Start Time	Test Name	Test Description	Test Goal	Priority	Top Temp °F	Bottom Temp °F
1	7:32	Zero 1	Instruments in place and zeroed, Start Set 1		0	91	94
2	7:45	L1T1W	Front axle 22' from EOS Long. Path 1	DB	2		
3	7:49	L1T2W	Front axle 30' from EOS Long. Path 1	AB	1		
4	7:52	L1T3W	Front axle 37' from EOS Long. Path 1	DB	2		
5	7:56	L1T5W	Front Axle 75' from EOS Long. Path 1	AB	1		
6	8:00	L1T2W	Front axle 30' from EOS Long. Path 1	AB	1		
7	8:03	Zero 2	Set 2		0	85.6	
8	8:09	L2T1W	Front axle 22' from EOS Long. Path 2	DB	2		
9	8:12	L2T2W	Front axle 30' from EOS Long. Path 2	AB	1		
10	8:16	L2T3W	Front axle 37' from EOS Long. Path 2	DB	2		
11	8:18	L2T5W	Front axle 75' from EOS Long. Path 2	AB	1		
12	8:24	L2T2W	Front axle 30' from EOS Long. Path 2	AB	1		
13	8:26	Zero 3	Set 3		0	91.6	
14	8:29	L3T1W	Front axle 22' from EOS Long. Path 3	DC	2		
15	8:31	L3T2W	Front axle 30' from EOS Long. Path 3	AC	1		
16	8:35	L3T3W	Front axle 37' from EOS Long. Path 3	DC	2		
17	8:38	L3T5W	Front axle 75' from EOS Long. Path 3	AC	1		
18	8:40	L3T2W	Front axle 30' from EOS Long. Path 3	AC	1		
19	8:43	Zero 4	Set 4		0	91	85.6
20	8:54	L1T2W L3T2W SS	Two trucks Side by Side	A	1		
21	8:59	L1T5W L3T5W SS	Two trucks Side by Side	A	1		
22	9:08	L1T2W L3T2W SS	Two trucks Side by Side	AR	2		
23	9:17	Zero 5	MnDOT Break #1		0	91.8	85.6
24	9:42	Zero 6	Set 6		0	101.5	88.3
25	9:51	L1T2W BB #1	Two trucks Back to Back	AB	1		
26	9:52	L1T2W BB #2	Two trucks Back to Back	AB	1		
27	9:59	L2T2W BB	Two trucks Back to Back	AB	1		
28	10:07	L3T2W BB	Two trucks Back to Back	AC	1		
29	10:15	L5T2W BB	Two trucks Back to Back	AC	3		
30	10:24	L4T2W BB	Two trucks Back to Back	AC	0		
31	10:27	Zero 7	Truck Drove Across Bridge		0		
32	10:29	Zero 7	Set 7		0	102.6	86.2
33	10:35	L1T2W BB	Two trucks Back to Back	ABR	2		
34	10:41	L1T5W BB	Two trucks Back to Back	ABR	2		
35	10:49	L4T5W BB	Two trucks Back to Back	ABR	2		
36	10:56	Zero 8	Set 8		0	93	64.8
37	11:00	L4T2W	Front axle 30' from EOS Long. Path 4	ABF	1		
38	11:03	L4T5W	Front axle 75' from EOS Lon. Path 4	ABF	1		
39	11:09	L5T2W	Front axle 30' from EOS Long. Path 5	AC	1		

Table D.2: Test schedule page 2 for Bridge 27926 on June 6, 2021.

Time Increment	Actual Start Time	Test Name	Test Description	Test Goal	Priority	Top Temp °F	Bottom Temp °F
40	11:11	L5T5W	Front axle 75' from EOS Long. Path 5	AC	1		
41	11:16	L1T2W	Front axle 30' from EOS Long. Path 1	ABR	2		
42	11:19	L1T5W	Front axle 75' from EOS Long Path 1	ABR	2		
43	11:22	Zero 9	Set 9			100.5	71.1
44	11:25	L2T2W	Front axle 30' from EOS Long. Path 2	ABR	1		
45	11:28	L2T5W	Front axle 75' from EOS Long. Path 2	ABR	1		
46	11:32	L3T2W	Front axle 30' from EOS Long. Path 3	ACR	1		
47	11:34	L3T5W	Front axle 75' from EOS Long. Path 3	ACR	1		
48	11:37	L4T2W	Front axle 30' from EOS Long. Path 4	ACR	1		
49	11:40	L4T5W	Front axle 75' from EOS Long Path 4	ACR	1		
50	11:44	Zero 10			0		
51	12:34	Zero 11	Set 11		0	107	69.8
52		L5T2W	Front axle 30' from EOS Long. Path 5	ACR	1		
53		L5T5W	Front axle 75' from EOS Lon. Path 5	ACR	1		
54	12:42	L1T1E	Front axle 22' from EEOS Long. Path 1	DBE	3		
55	12:45	L1T2E	Front axle 30' from EEOS Long. Path 1	ABE	2		
56	12:47	L1T3E	Front axle 37' from EEOS Long. Path 1	DBE	3		
57	12:51	L1T5E	Front axle 75' from EEOS Long. Path 1	ABE	2		
58	12:53	Zero 12	Set 12		0	115.2	74.5
59	12:56	L2T1E	Front axle 22' from EEOS Long Path 2	DBE	3		
60	12:59	L2T2E	Front axle 30' from EEOS Long. Path 2	ABE	2		
61	1:04	L2T3E	Front axle 37' from EEOS Long. Path2	DBE	3		
62	1:06	L2T5E	Front axle 75' from EEOS Long. Path 2	ABE	2		
63	1:11	Zero 13	Set 13		0	109	67.4
64	1:14	L3T1E	Front Axle 22' from EEOS Long. Path 3	DCE	3		
65	1:16	L3T2E	Front axle 30' from EEOS Long. Path 3	ACE	2		
66	1:19	L3T3E	Front axle 37' from EEOS Long. Path 3	DCE	3		
67	1:21	L3T5E	Front axle 75' from EEOS Long. Path 3	ACE	2		
68	1:23	L4T5E	Truck was still moving		2		
69	1:26	L4T5E			2		
70	1:29	Zero 14	Setup for Dynamic Testing		0	108.1	74.6
71	2:52	Zero 15			0		
72	3:06	EWN	Dynamic Truck Test East-West North Lane	H	1		
73	3:09	EWS	Dynamic Truck Test East-West South Lane	H	1		
74	3:11	WEN	Dynamic Truck Test West-East North Lane	H	1		
75	3:12	WES	Dynamic Truck Test West-East South Lane	H	1		
76	3:31	IH #1	Accel # 65531	H	1	123.4	83.3
77	3:32	IH #2	Accel # 69529	H	1		
78	3:34	IH #3	Accel # 69519	H	1		

Table D.3: Test schedule page 3 for Bridge 27296 on June 6, 2021.

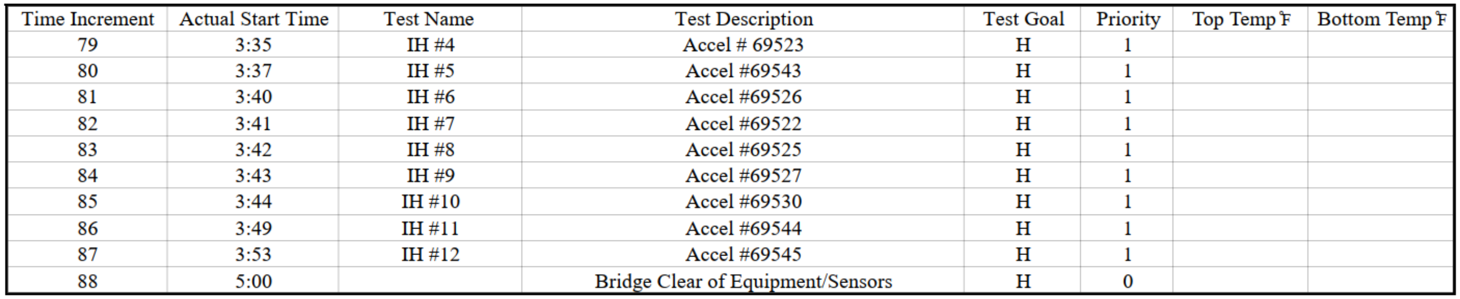

Time Increment	Actual Start Time	Test Name	Test Description	Test Goal	Priority	Top Temp ˚F	Bottom Temp ˚F
79	3:35	IH #4	Accel # 69523	H	1		
80	3:37	IH #5	Accel #69543	H	1		
81	3:40	IH #6	Accel #69526	H	1		
82	3:41	IH #7	Accel #69522	H	1		
83	3:42	IH #8	Accel #69525	H	1		
84	3:43	IH #9	Accel #69527	H	1		
85	3:44	IH #10	Accel #69530	H	1		
86	3:49	IH #11	Accel #69544	H	1		
87	3:53	IH #12	Accel #69545	H	1		
88	5:00		Bridge Clear of Equipment/Sensors	H	0		

Table D.4: Test schedule page 1 for Bridge 27925 on June 12, 2021.

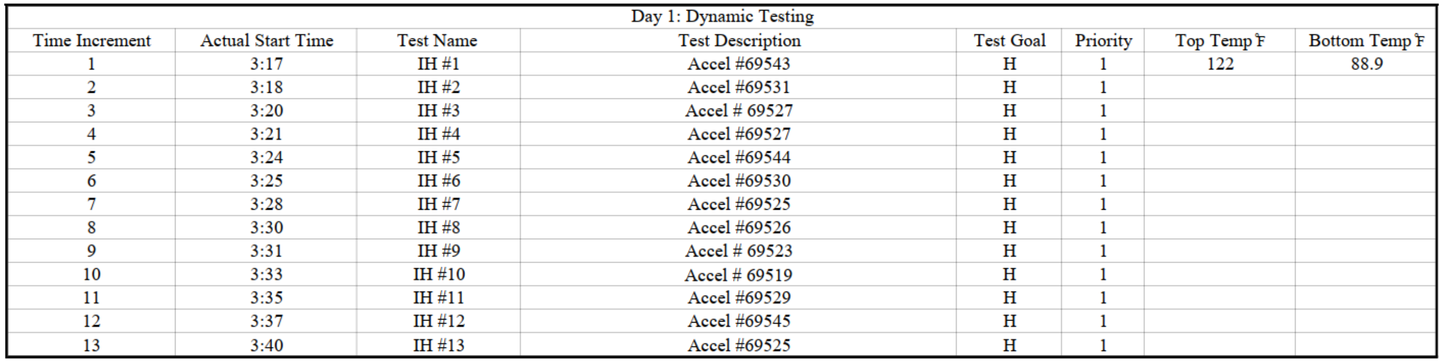

Day 1: Dynamic Testing							
Time Increment	Actual Start Time	Test Name	Test Description	Test Goal	Priority	Top Temp ˚F	Bottom Temp ˚F
1	3:17	IH #1	Accel #69543	H	1	122	88.9
2	3:18	IH #2	Accel #69531	H	1		
3	3:20	IH #3	Accel # 69527	H	1		
4	3:21	IH #4	Accel #69527	H	1		
5	3:24	IH #5	Accel #69544	H	1		
6	3:25	IH #6	Accel #69530	H	1		
7	3:28	IH #7	Accel #69525	H	1		
8	3:30	IH #8	Accel #69526	H	1		
9	3:31	IH #9	Accel # 69523	H	1		
10	3:33	IH #10	Accel # 69519	H	1		
11	3:35	IH #11	Accel #69529	H	1		
12	3:37	IH #12	Accel #69545	H	1		
13	3:40	IH #13	Accel #69525	H	1		

Table D.5: Test schedule page 2 for Bridge 27925 on June 13, 2021.

Day 2: Static Testing							
Time Increment	Actual Start Time	Test Name	Test Description	Test Goal	Priority	Top Temp ℉	Bottom Temp ℉
1			UMD Team arrive at Site, Assign initial roles				
2			Check LVDT Level and Strain Gauge fixture				
3			Start Base Station and Nodes				
4			Check Sensor Output				
5			MnDOT Trucks Arrive, Verify Truck Dimensions				
6	7:35	Zero 1	Instruments in place and zeroed, Start Set 1		0	79.2	85.1
7	7:47	L1T1 BB	Rear axles of two trucks centered at midspan	AB	1		
8	7:54	L2T1 BB	Rear axles of two trucks centered at midspan	AB	2		
9	7:59	L3T1 BB	Rear axles of two trucks centered at midspan	AC	1		
10	8:07	L4T1 BB	Rear axles of two trucks centered at midspan	AC	2		
11	8;09	L5T1 BB	Rear axles of two trucks centered at midspan	AC	1		
12	8:14	Zero 2	Set 2		0	70.2	70.9
13	8:23	L1T1E SS	Two trucks side by side 1' from near barrier	AB	1		
14	8:32	L2T1E SS	Two Trucks side by side inside truck aligned with Path 2	AB	2		
15	8:39	L3T1E SS	Two Trucks side by side inside truck aligned with Path 3	AC	2		
16	8:46	L4T1E SS	Two Trucks side by side inside truck aligned with Path 4	AC	1		
17	8:53	L5T1E SS	Two Trucks side by side inside truck aligned with Path 5	AC	1		
18	9:02	Zero 3			0	83.7	76.8
		Zero 4	Set 4			93.9	83.5
19	9:23	L1T1 BB	Rear axles of two trucks centered at midspan	ABR	1		
20	9:29	L5T1 BB	Rear axles of two trucks centered at midspan	ACR	1		
21	9:35	L1T1W	Front axle 30' from EOS Long. Path 1	AB	2		
22	9:38	L1T2W	Front axle 55' from EOS Long. Path 1	B	2		
23	9:41	L2T1W	Front axle 30' from EOS Long. Path 2	AB	2		
24	9:44	L2T2W	Front axle 55' from EOS Long. Path 2	B	2		
25	9:48	Zero 5	Set 5		0	100.2	86
26	9:53	L3T1W	Front axle 30' from EOS Long. Path 3	A	1		
27	9:55	L3T2W	Front axle 55' from EOS Long. Path 3	A	2		
28	9:59	L4T1W	Front axle 30' from EOS Long. Path 4	AB	1		
29	10:03	L4T2W	Front axle 55' from EOS Long. Path 4	AB	2		
30	10:06	L5T1W	Front axle 30' from EOS Long. Path 5	AC	1		
31	10:09	L5T2W	Front axle 55' from EOS Long. Path 5	AC	2		
32	10:13	L1T1W	Front axle 30' from EOS Long. Path 1	ABR	1		
33	10:16	L1T2W	Front axle 55' from EOS Long. Path 1	ABR	2		
34	10:18	Zero 6	Set 6		0	113.5	91.6
35	10:25	L5T2E	Front axle 30' from EOS Long. Path 5	ACE	1		
36	10:27	L5T1E	Front axle 55' from EOS Long. Path 5	ACE	2		
37	10:30	L4T2E	Front axle 30' from EOS Long. Path 4	ACE	1		
38	10:33	L4T1E	Front axle 55' from EOS Long. Path 4	ACE	2		
39	10:36	L3T2E	Front axle 30' from EOS Long. Path 3	ACE	1		
40	10:38	L3T1E	Front axle 55' from EOS Long. Path 3	ACE	2		

Table D.6: Test schedule page 3 for Bridge 27925 on June 13, 2021.

Time Increment	Actual Start Time	Test Name	Test Description	Test Goal	Priority	Top Temp ℉	Bottom Temp ℉
41	10:44	Zero 7	Complete Set 6, MnDOT Break #2 (Lunch)		0	102.6	77.6
42	10:52	L2T1E	Front axle 30' from EOS Long. Path 2	ABE	1		
43	10:49	L2T2E	Front axle 55' from EOS Long. Path 2	ABE	2		
44	10:54	L1T2E	Front axle 30' from EOS Long. Path 1	ABE	1		
45	10:57	L1T1E	Front axle 55' from EOS Long. Path 1	ABE	2		
46	11;00	L5T2E	Front axle 30' from EOS Long. Path 2	ACE	1		
47	11:02	L5T1E	Front axle 55' from EOS Long. Path 2	ACE	2		
48	11:04	Zero 8			0	101.2	76.8

APPENDIX E: EXACT TRUCK POSITIONS FROM EACH TEST ON BRIDGE 27926

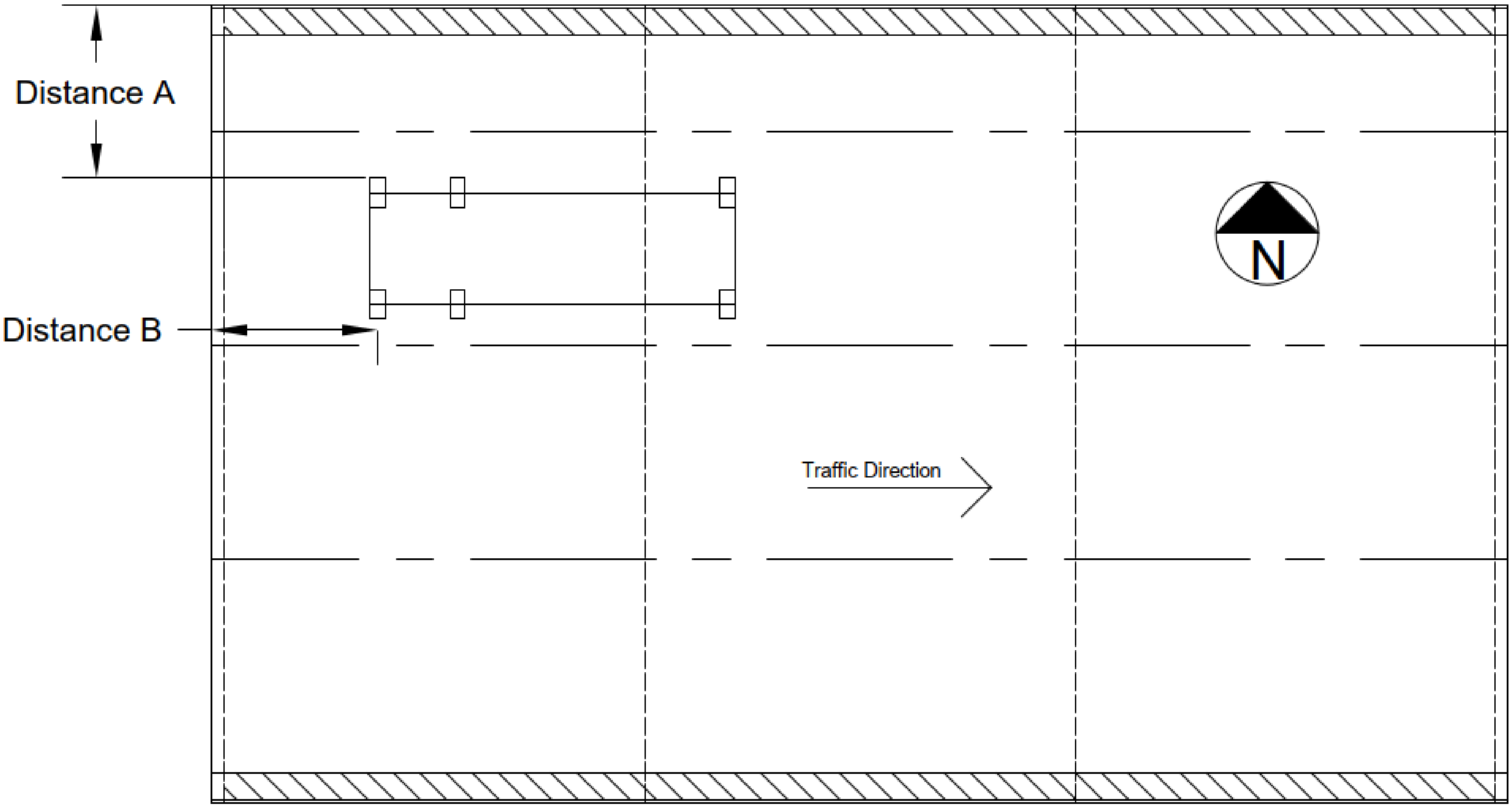

Figure E.1: Truck position key for Bridge 27926.

Table E.1: Truck axle positions for the field test on Bridge 27926.

Truck Test	Truck 215556			Truck 214579		
	(A) Rear Axle 1 Transverse Location to center of tire (in.)	Rear Axle 2 Transverse Location to center of tire (in.)	(B) Rear Axle Longitudinal Location to center of tire (in.)	(A) Rear Axle 1 Transverse Location to center of tire (in.)	Rear Axle 2 Transverse Location to center of tire (in.)	(B) Rear Axle Longitudinal Location to center of tire (in.)
L1T1W	33	129	21	---	---	---
L1T2W	33	129	117	---	---	---
L1T3W	33	129	202	---	---	---
L1T5W	33.5	129.5	660	---	---	---
L1T2W	33	129	120	---	---	---
L2T1W	74	170	25	---	---	---
L2T2W	74	170	118	---	---	---
L2T3W	74	170	200	---	---	---
L2T5W	73	169	658	---	---	---
L2T2W	73.5	169.5	119	---	---	---
L3T1W	115	211	22	---	---	---
L3T2W	114.5	210.5	117	---	---	---
L3T3W	114	210	200	---	---	---
L3T5W	115	211	657	---	---	---
L3T2W	115	211	117	---	---	---
L1T2W L3T2W SS	33.5	129.5	119	143	239	119.5
L1T5W L3T5W SS	34	130	658	145	241	659
L1T2W L3T2W SS	34	130	119	147	243	118
L1T2W BB #1	34	130	241	36	132	145

Table E.1 (cont): Truck axle positions for the field test on Bridge 27926.

Truck Test	(A) Rear Axle 1 Transverse Location to center of tire (in.)	Rear Axle 2 Transverse Location to center of tire (in.)	(B) Rear Axle Longitudinal Location to center of tire (in.)	(A) Rear Axle 1 Transverse Location to center of tire (in.)	Rear Axle 2 Transverse Location to center of tire (in.)	(B) Rear Axle Longitudinal Location to center of tire(in.)
L1T2W BB #2	33.5	129.5	192	36.5	132.5	96
L2T2W BB	73.5	169.5	193	77	173	98
L3T2W BB	115	211	192	119.5	215.5	97
L3T5W BB	116.5	212.5	768	118	214	674
L4T2W BB	220	316	200	220	316	100
L4T5W BB	219	315	768	220	316	673
L1T2W BB	23	119	195	28.5	124.5	99
L1T5W BB	36	132	770	35	131	679
L4T2W	219	315	119	---	---	---
L4T5W	215.5	311.5	661	---	---	---
L5T2W	408	504	117	---	---	---
L5T5W	407	503	656	---	---	---
L1T2W	32.5	128.5	117	---	---	---
L1T5W	33.5	129.5	661	---	---	---
L2T2W	71	167	118	---	---	---
L2T5W	72.5	168.5	662	---	---	---
L3T2W	115	211	119	---	---	---
L3T5W	115	211	659	---	---	---
L4T2W	218.5	314.5	118	---	---	---
L4T5W	216	312	658	---	---	---

Table E.1 (cont): Truck axle positions for the field test on Bridge 27926.

Truck Test	(A) Rear Axle 1 Transverse Location to center of tire (in.)	Rear Axle 2 Transverse Location to center of tire (in.)	(B) Rear Axle Longitudinal Location to center of tire (in.)	(A) Rear Axle 1 Transverse Location to center of tire (in.)	Rear Axle 2 Transverse Location to center of tire (in.)	(B) Rear Axle Longitudinal Location to center of tire(in.)
L1T1E	27.5	123.5	850	---	---	---
L1T2E	28.5	124.5	754	---	---	---
L1T3E	28.5	124.5	672	---	---	---
L1T5E	29	125	215	---	---	---
L2T1E	71	167	841	---	---	---
L2T2E	70	166	756	---	---	---
L2T3E	70	166	673	---	---	---
L2T5E	70.5	166.5	214	---	---	---
L3T1E	112	208	850	---	---	---
L3T2E	112.5	208.5	756	---	---	---
L3T3E	111.5	207.5	672	---	---	---
L3T5E	111	207	215	---	---	---
L4T5E	217	313	212	---	---	---

APPENDIX F: PHOTOS FROM INSTRUMENTING AND TESTING BRIDGE 27926

Figure F.1: Strain gauges installed at midspan of the West span Bridge 27926.

Figure F.2: Tiltmeter installed perpendicular to traffic direction on the North side of Bridge 27926.

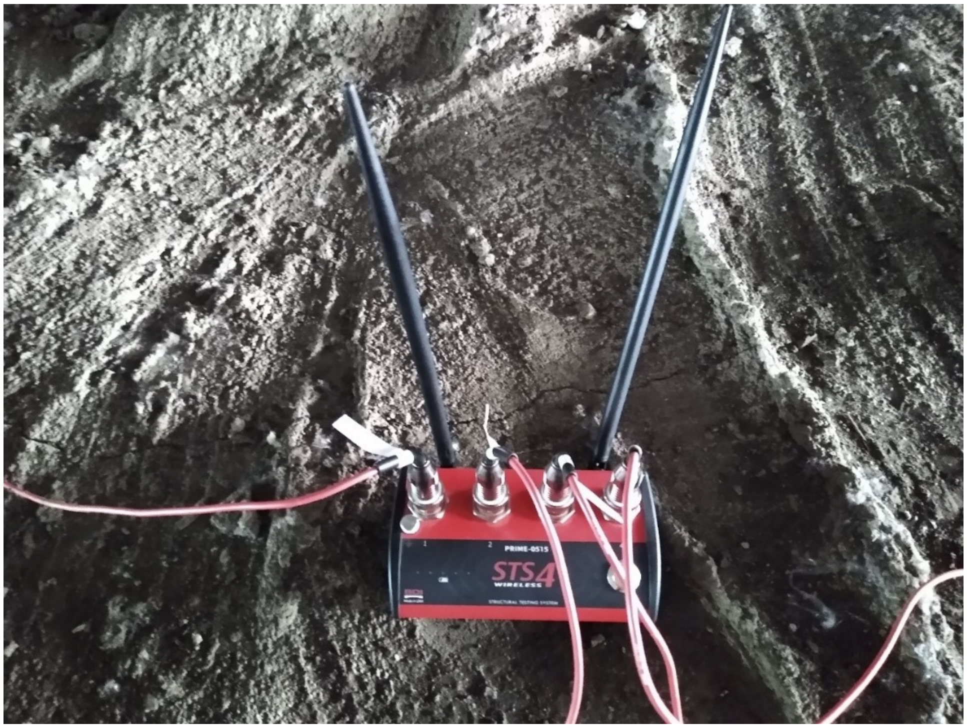

Figure F.3: Bridge Diagnostics four-channel node used for data collection.

Figure F.4: Bridge Diagnostics strain gauge.

Figure F.5: Array of LVDTs, strain gauges, nodes, and tiltmeters installed on the West span of Bridge 27926.

Figure F.6: LVDTs installed on the East span of Bridge 27926.

Figure F.7: Truck positioned at L2T4W (4.5 ft from the barrier and midspan of center span) on Bridge 27926 during live load testing.

Figure F.8: Aligning truck for side-by-side testing.

Figure F.9: Side-by-side truck test on the West span of Bridge 27926.

Figure F.10: Back-to-back truck tests on Bridge 27926.

Figure F.11: Back-to-back truck tests on the West span of Bridge 27926 centered at midspan (deflection joint and instruments).

Figure F.12: Truck positioned at L1T4W of Bridge 27926.

Figure F.13: Truck positioned at L1T2W of Bridge 27926.

Figure F.14: Back-to-back trucks at West span of Bridge 27926.

Figure F.15: Back-to-back trucks at West span of Bridge 27926.

Figure F.16: Back-to-back trucks at East span of Bridge 27926.

Figure F.17: Back-to-back trucks at East span of Bridge 27296.

Figure F.18: Single truck at L2T1E on Bridge 27926.

Figure F.19: Dynamic impact hammer testing on Bridge 27926.

APPENDIX G: TESTING PLANS FOR EACH BRIDGE

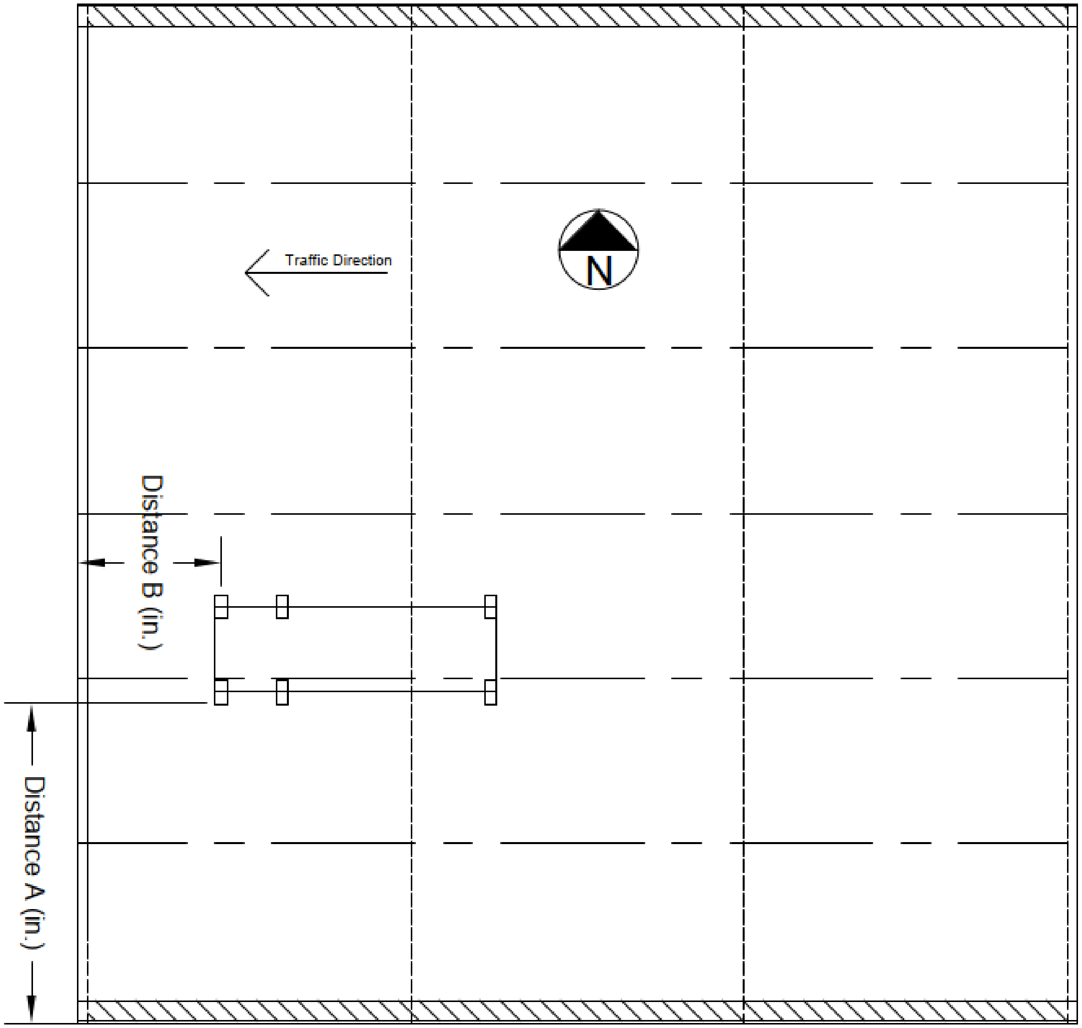

Figure G.1: Bridge 27925 truck position key facing West.

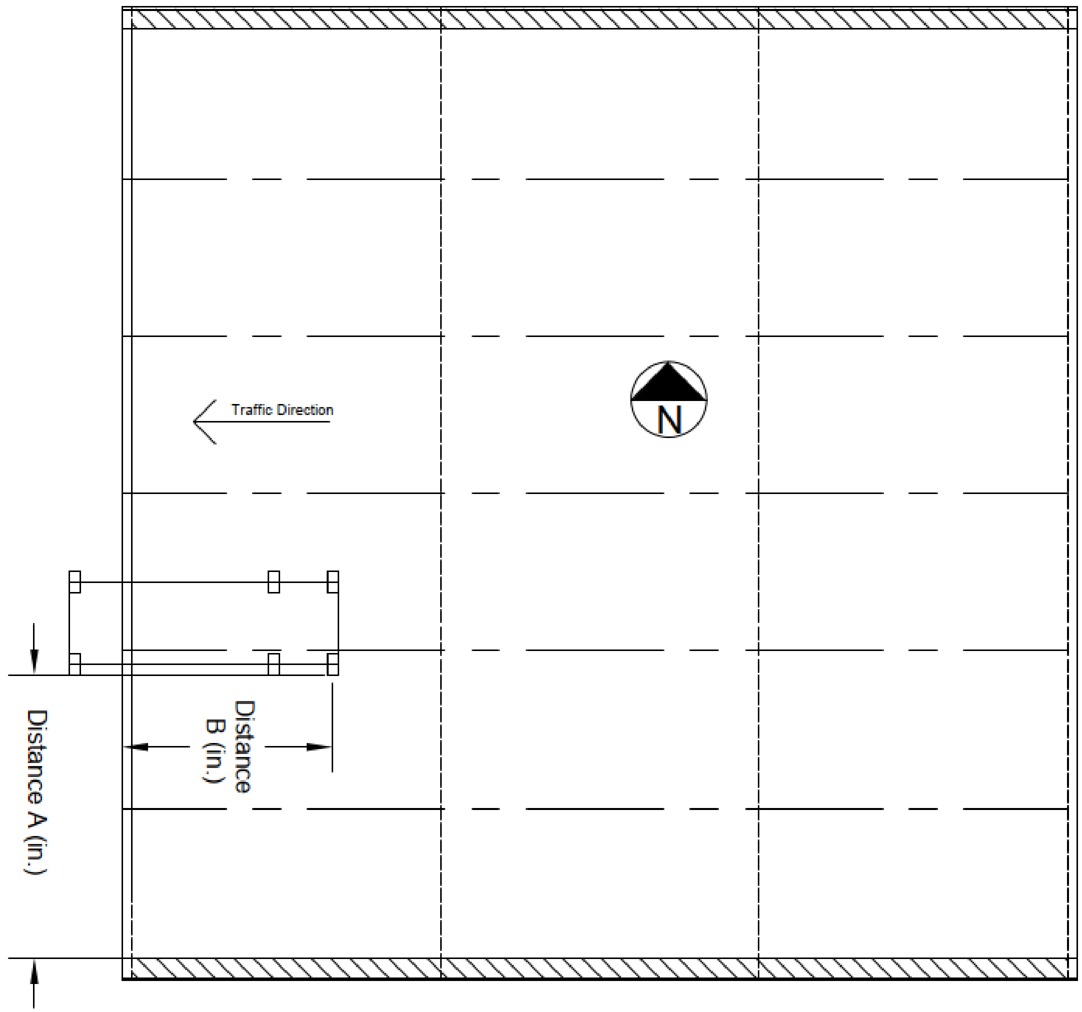

Figure G.2: Bridge 27925 truck position key facing East.

Table G.1: Truck axle positions from the field test on Bridge 27925.

Truck Test	Truck 215556			Truck 214579		
	(A) Rear Axle 1 Transverse Location to center of tire (in.)	Rear Axle 2 Transverse Location to center of tire (in.)	(B) Rear Axle Longitudinal Location to center of tire (in.)	(A) Rear Axle 1 Transverse Location to center of tire (in.)	Rear Axle 2 Transverse Location to center of tire (in.)	(B) Rear Axle Longitudinal Location to center of tire(in.)
L1T1 BB	33	129	196	30	126	101
L2T1 BB	107	203	196	105	201	100
L3T1 BB	204	300	196	200	296	102
L4T1 BB	296	392	196	297	393	101
L5T1 BB	398	494	194	399	495	99
L1T1E SS	143	239	183	33	129	183
L2T1E SS	217	313	184	105	201	184
L3T1E SS	312.5	408.5	182	201	297	181
L4T1E SS	408.5	504.5	181	298	394	183
L5T1E SS	510	606	182	398	494	182.5
L1T1 BB R	32	128	199	33	129	106
L5T1 BB R	395	491	196	397	493	102
L1T1W	29	125	121	---	---	---
L2T1W	106	202	120	---	---	---
L3T1W	199	295	120	---	---	---
L4T1W	294	390	117	---	---	---
L5T1W	395	491	115	---	---	---
L1T1W R	31	127	118	---	---	---
L5T1W R	---	---	---	399	495	177
L4T1E	---	---	---	297	393	178
L3T1E	---	---	---	202	298	179

Table G.1 (cont): Truck axle positions from the field test on Bridge 27925.

Truck Test	(A) Rear Axle 1 Transverse Location to center of tire (in.)	Rear Axle 2 Transverse Location to center of tire (in.)	(B) Rear Axle Longitudinal Location to center of tire (in.)	(A) Rear Axle 1 Transverse Location to center of tire (in.)	Rear Axle 2 Transverse Location to center of tire (in.)	(B) Rear Axle Longitudinal Location to center of tire(in.)
L2T1E	---	---	---	105	201	180
L1T1E	---	---	---	33.5	129.5	183
L5T1E	---	---	---	398	494	179

APPENDIX H: PHOTOS FROM INSTRUMENTING AND TESTING BRIDGE 27925

Figure H.1: Strain gauges installed on the West span of Bridge 27925.

Figure H.2: Strain gauge installed on the West span of Bridge 27925.

Figure H.3: View North from midspan of Bridge 27925.

Figure H.4: Center span of Bridge 27925 before installation of accelerometers.

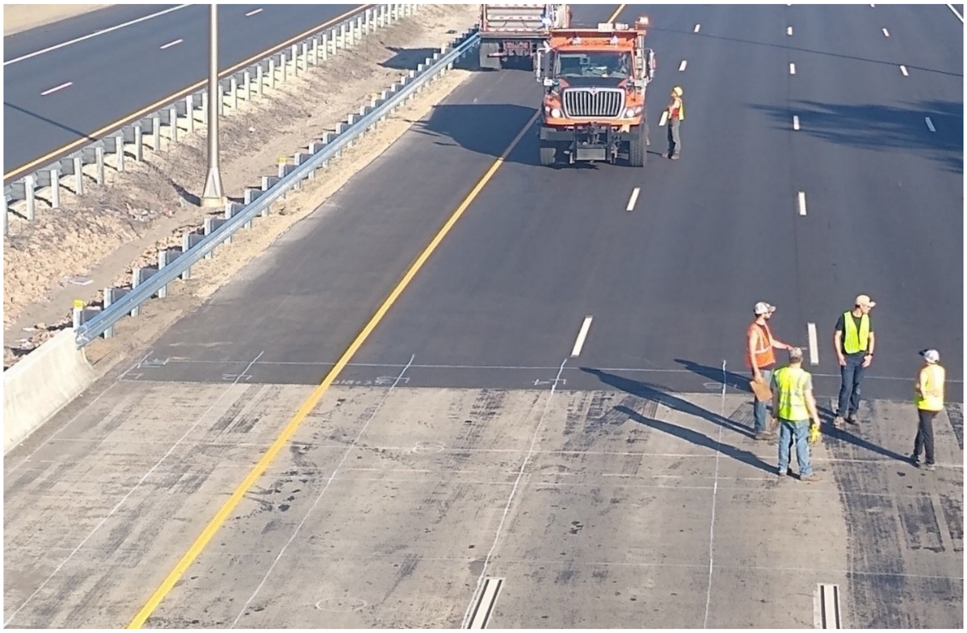

Figure H.5: Pre-test meeting on Bridge 27925.

Figure H.6: Back-to-back trucks at the West span of Bridge 27925 (L1T1W).

Figure H.7: Back-to-back trucks at the West span of Bridge 27925 (L1T1W).

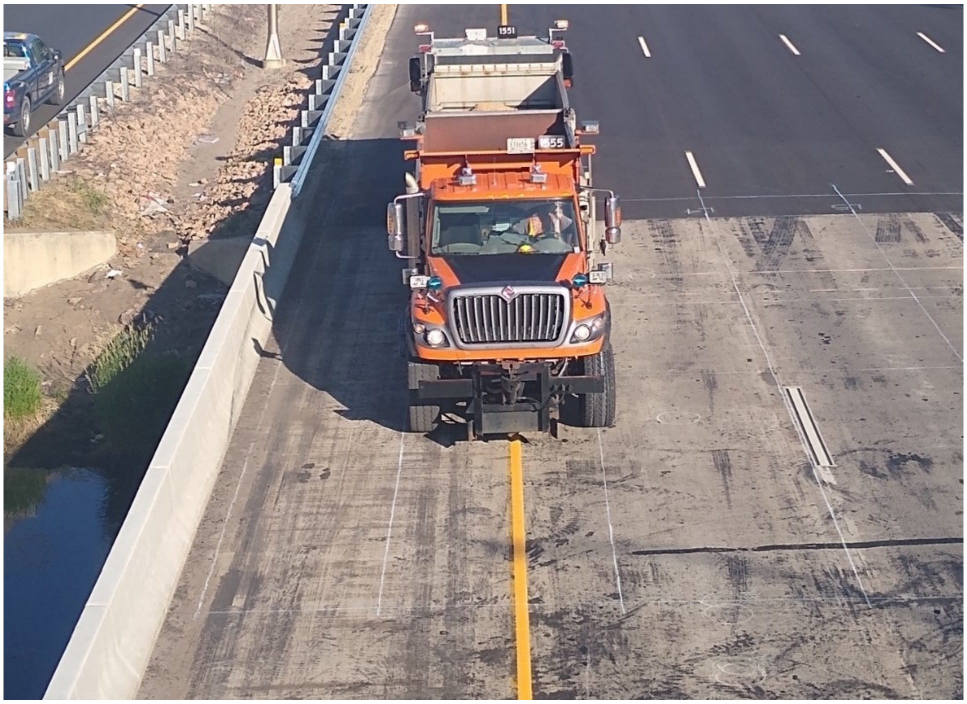

Figure H.8: Back-to-back trucks at West span of Bridge 27925 (L2T1W).

Figure H.9: Back-to-back trucks at West span of Bridge 27925 (L3T1W).

Figure H.10: Back-to-back trucks at West span of Bridge 27925 (L4T2W).

Figure H.11: Back-to-back trucks at West span of Bridge 27925 (L4T1W).

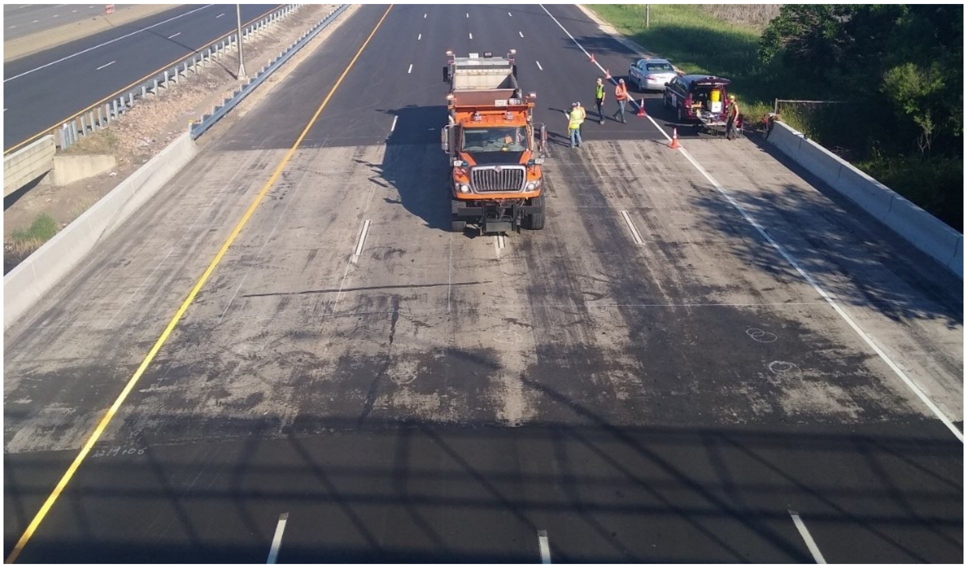

Figure H.12: Back-to-back trucks at West span of Bridge 27925 (L5T1W).

Figure H.13: Back-to-back trucks at West span of Bridge 27925 (L5T1W).

Figure H.14: Side-by-side trucks at West span of Bridge 27925.

Figure H.15: Side-by-side trucks at West span of Bridge 27925.

Figure H.16: Side-by-side trucks at West span of Bridge 27925.

Figure H.17: Side-by-side trucks at West span of Bridge 27925.

Figure H.18: Side-by-side trucks at West span of Bridge 27925.

APPENDIX I: ZERO-READINGS FROM EACH INSTRUMENT PLOTTED AGAINST TEMPERATURE

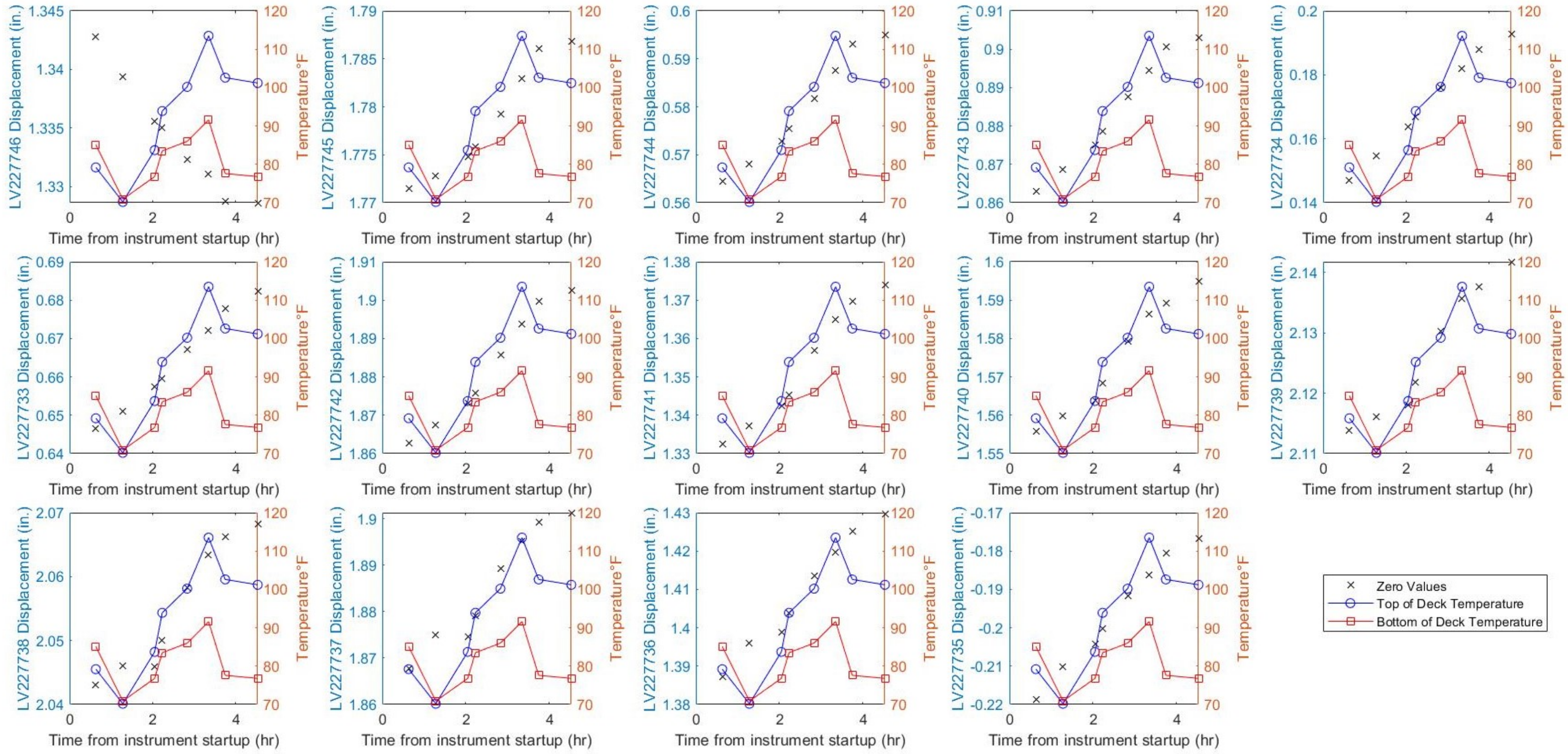

Figure I.1: Average zero-reading data for all LVDTs and bridge deck temperatures during live load testing on Bridge 27926.

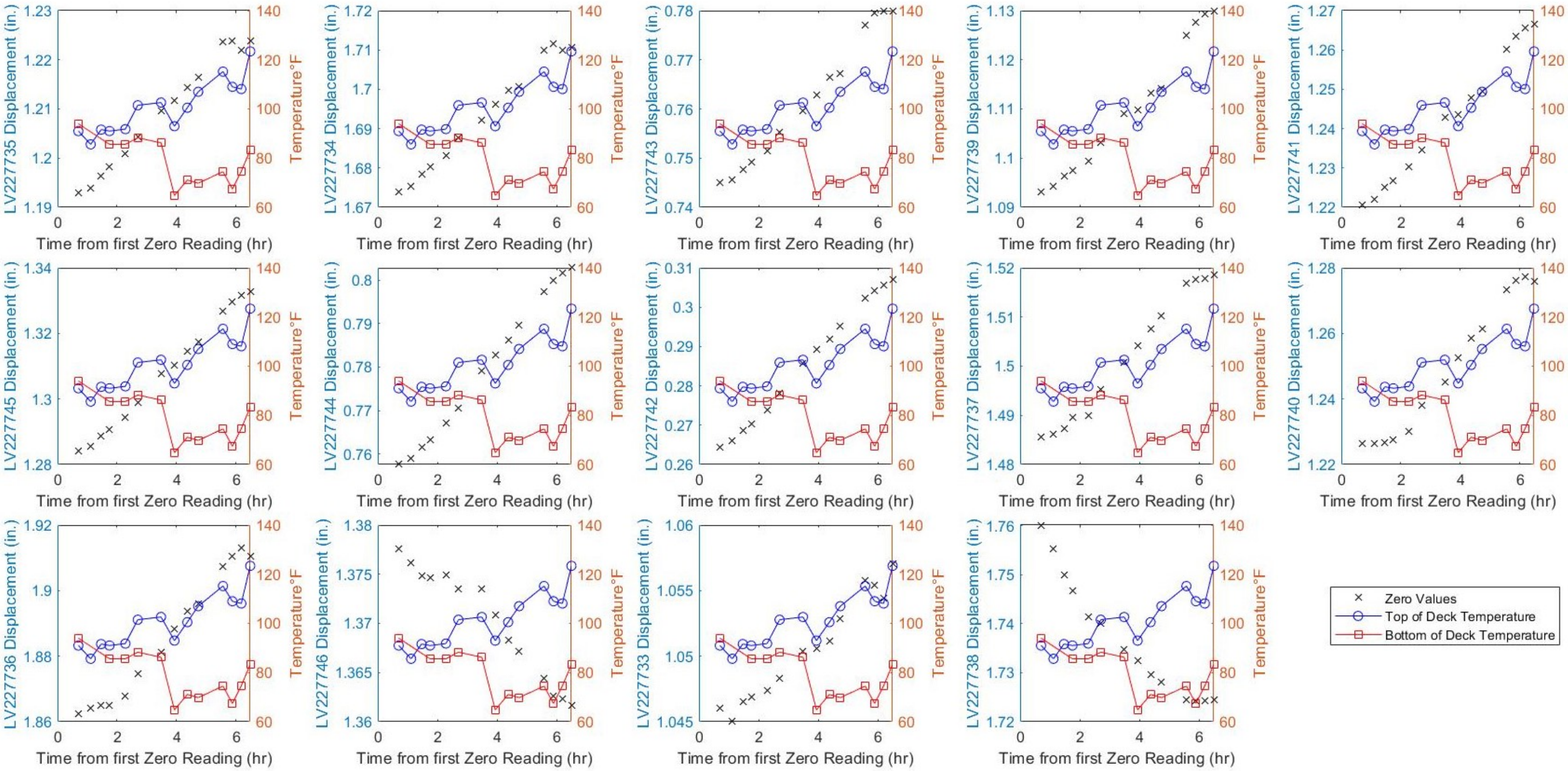

Figure I.2: Average zero-reading data for all LVDTs and bridge deck temperatures during live load testing on Bridge 27925.

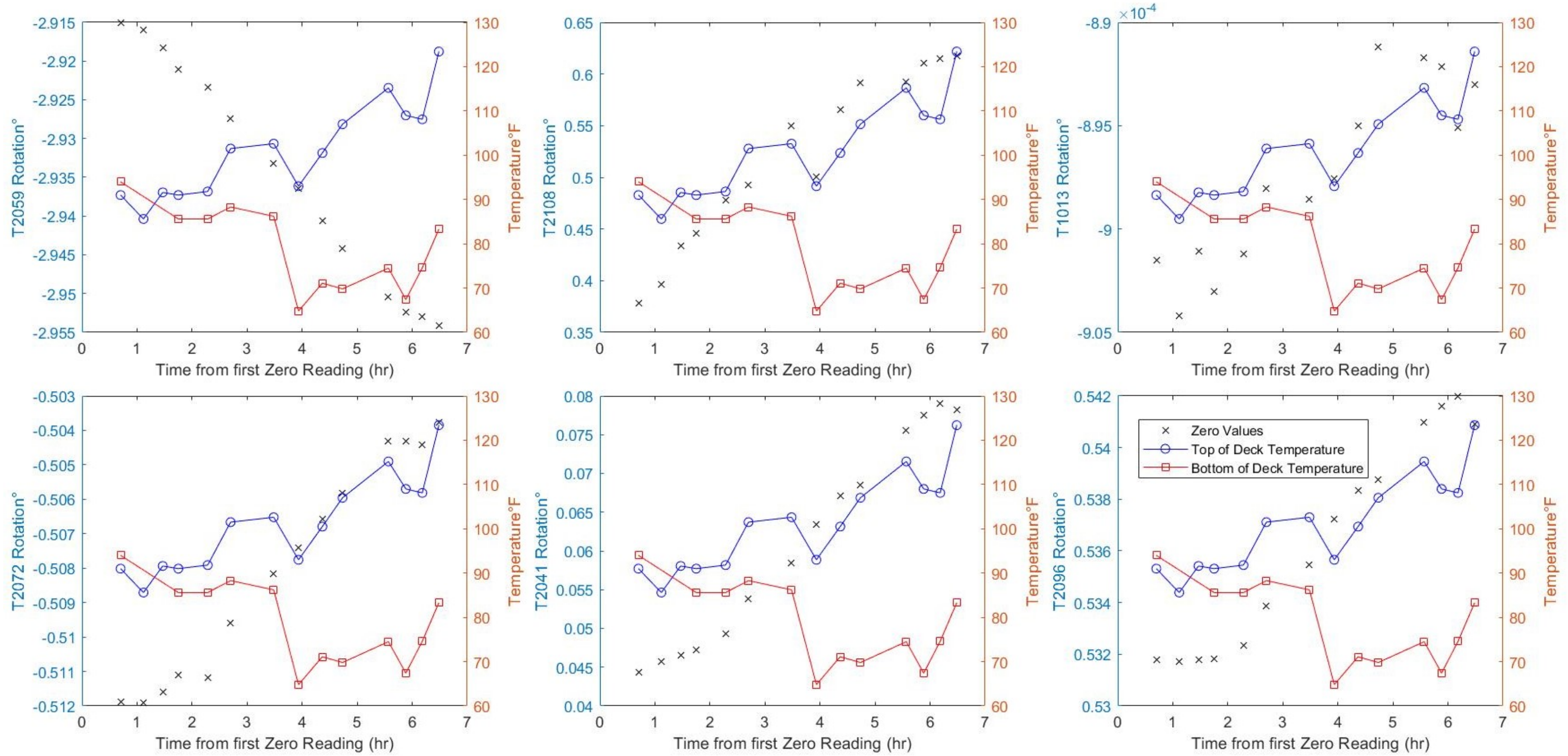

Figure I.3: Average zero-reading data for all tiltmeters and bridge deck temperatures during live load testing on Bridge 27926.

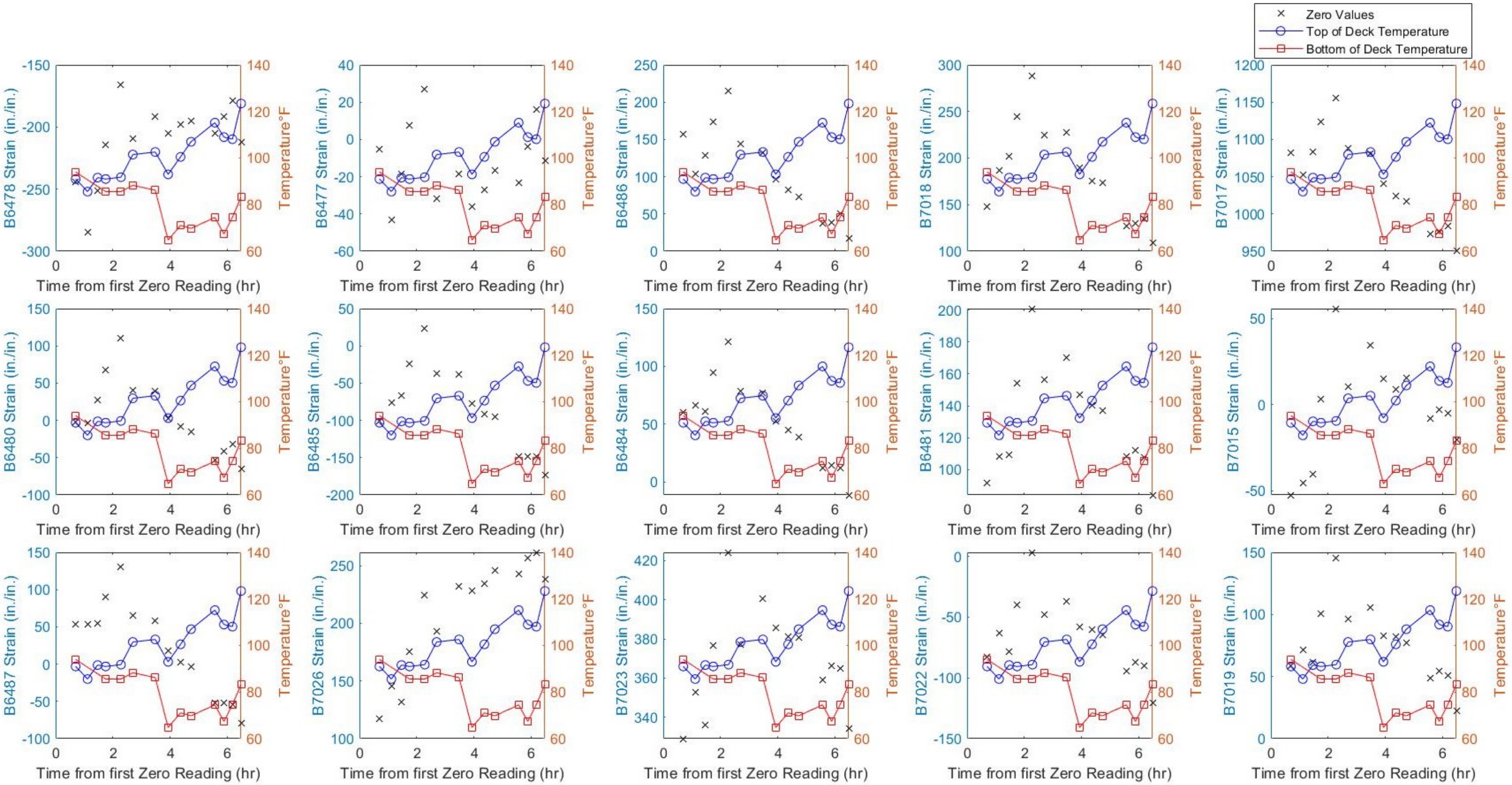

Figure I.4: Average zero-reading data for all strain gauges and bridge deck temperatures during live load testing on Bridge 27926.

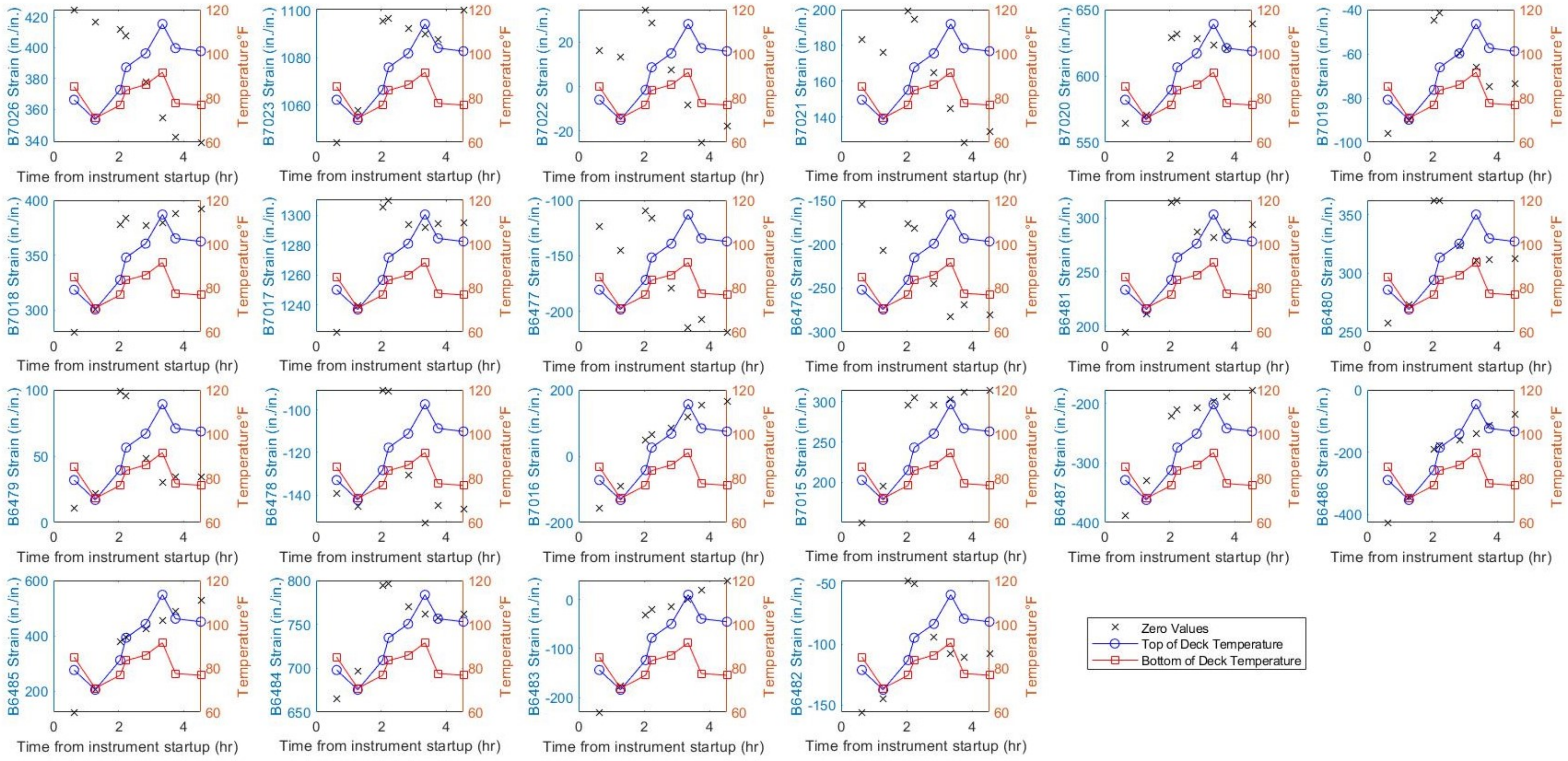

Figure I.5: Average zero-reading data for all strain gauges and bridge deck temperatures during live load testing on Bridge 27925.

APPENDIX J: STRAIN AND DISPLACEMENT AREA METHOD RESULTS FOR BRIDGE 27926

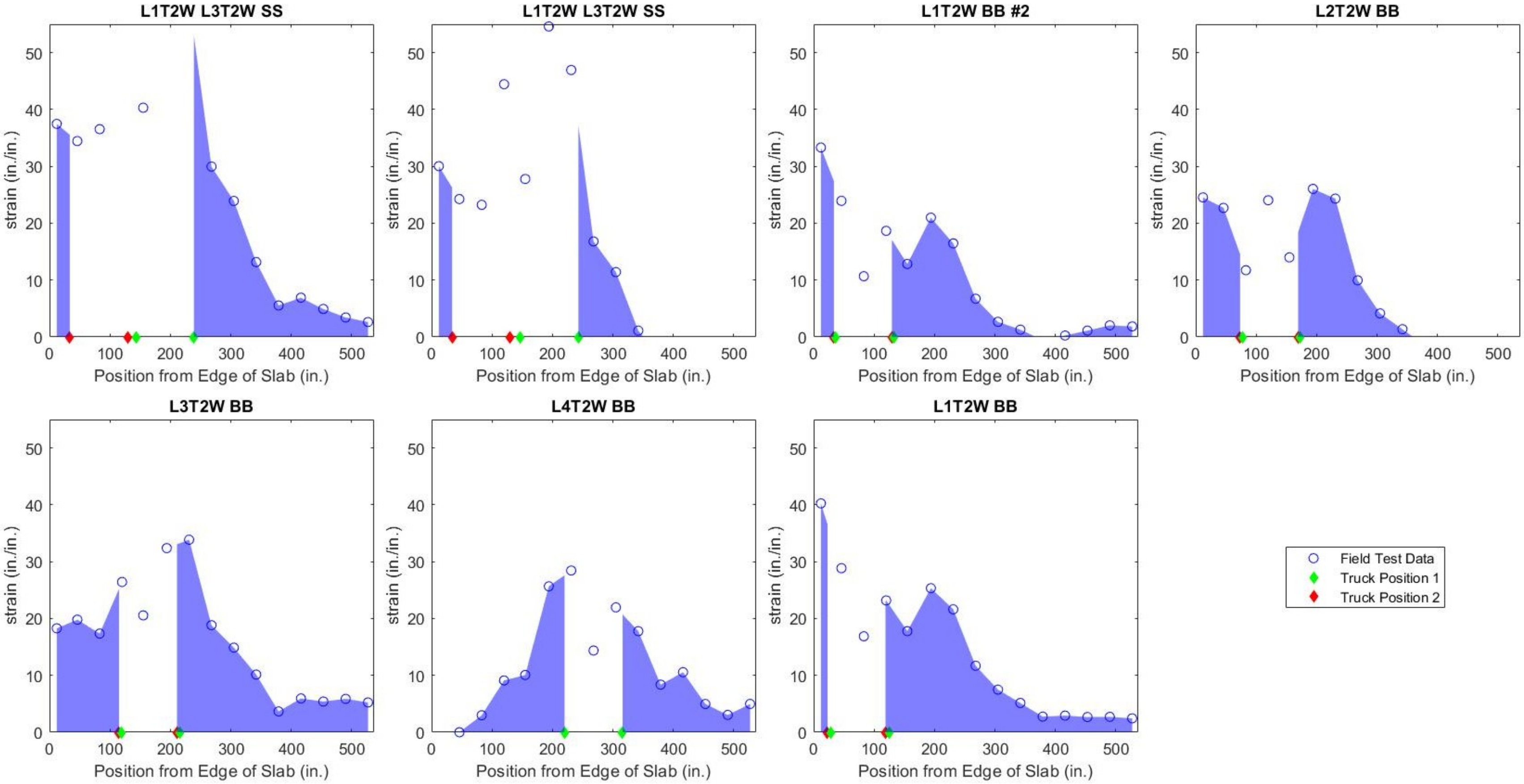

Figure J.1: Strain profiles for Bridge 27926 from back-to-back and side-by-side tests.

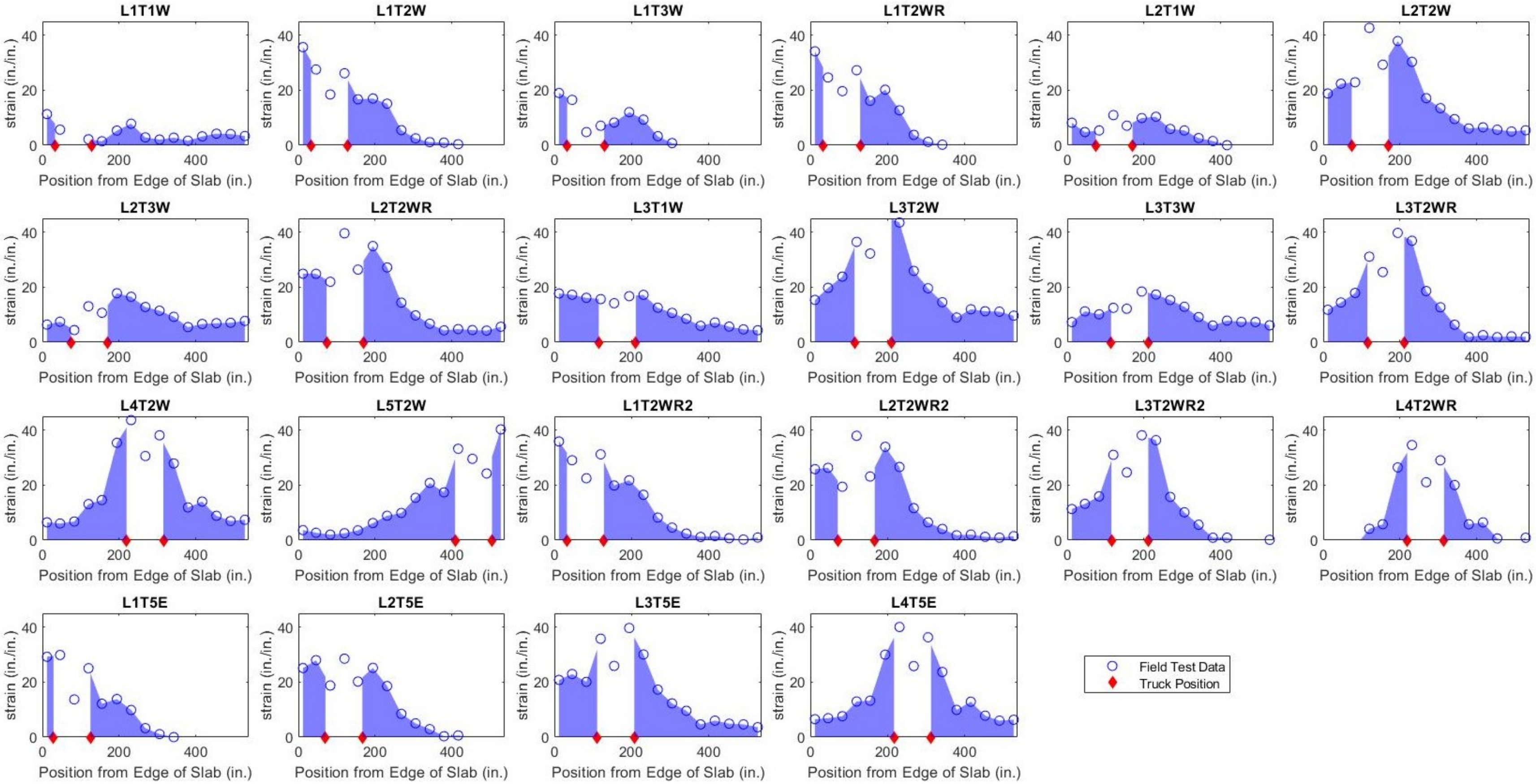

Figure J.2: Strain profiles for Bridge 27926 from single truck tests.

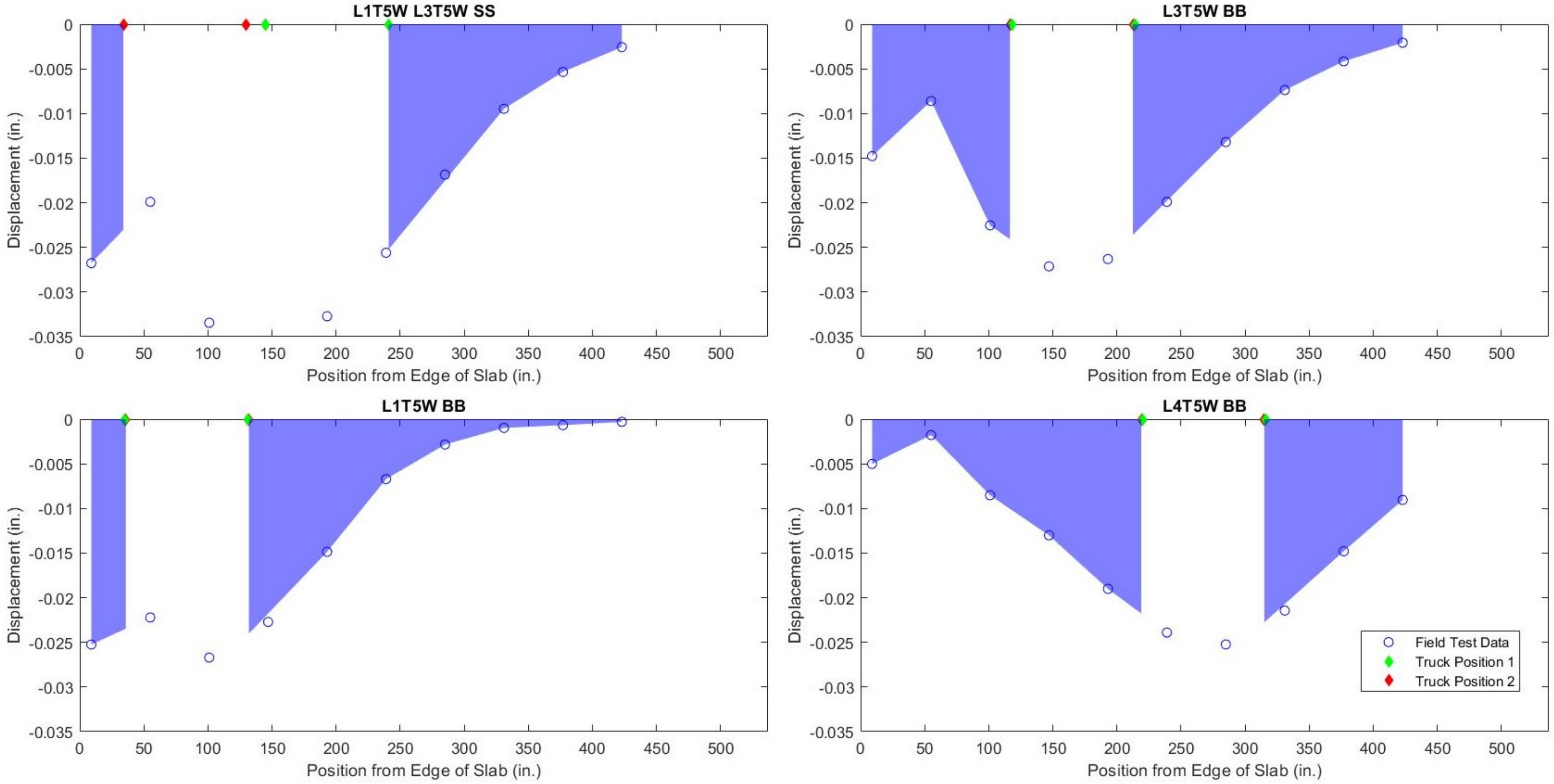

Figure J.3: Displacement profiles from back-to-back and side-by-side truck tests from Bridge 27926.

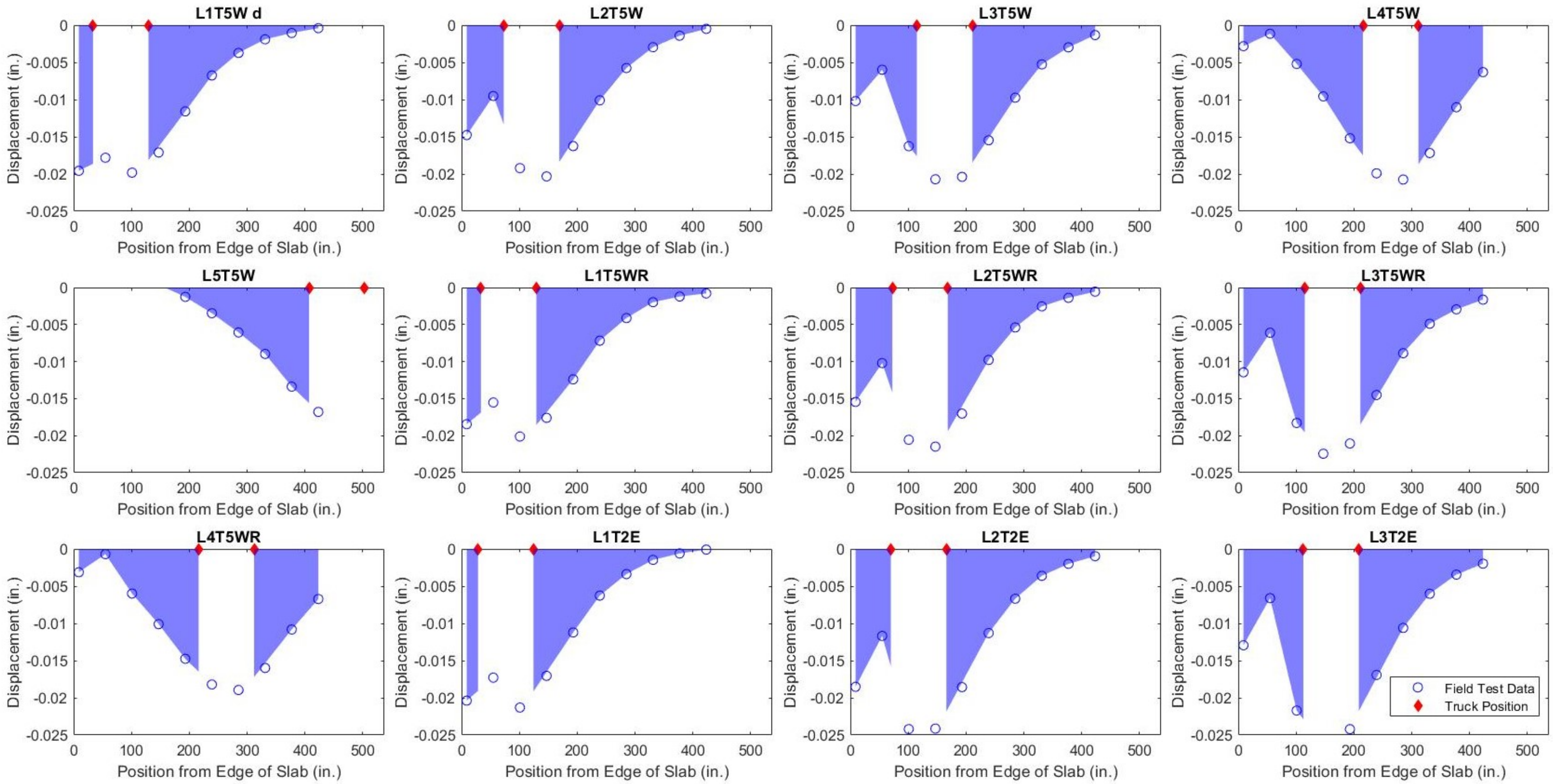

Figure J.4: Displacement profiles from single truck tests from Bridge 27926.

APPENDIX K: STRAIN AND DISPLACEMENT AREA METHOD RESULTS FOR BRIDGE 27925

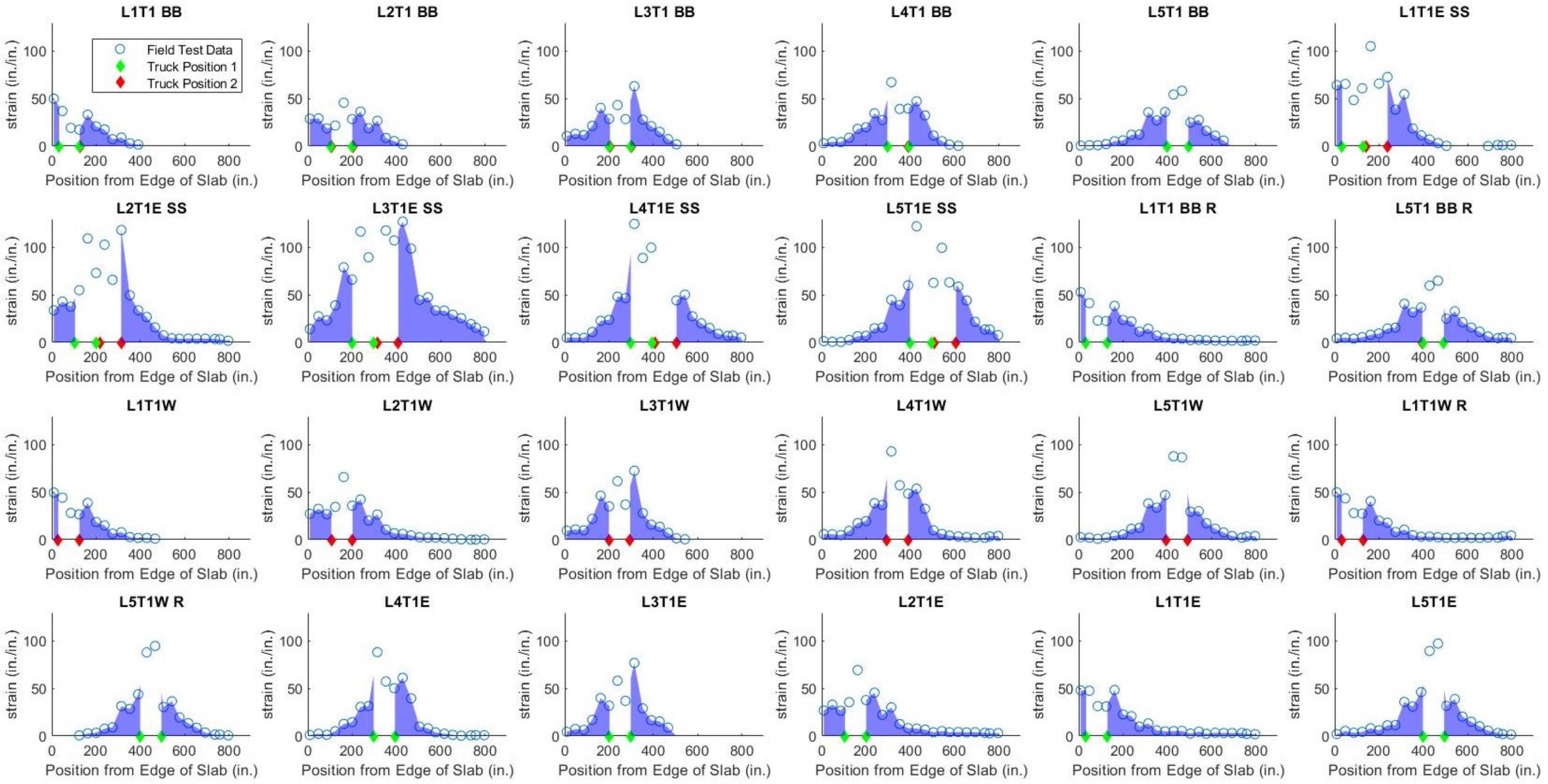

Figure K.1: Strain profiles from live load tests on Bridge 27925.

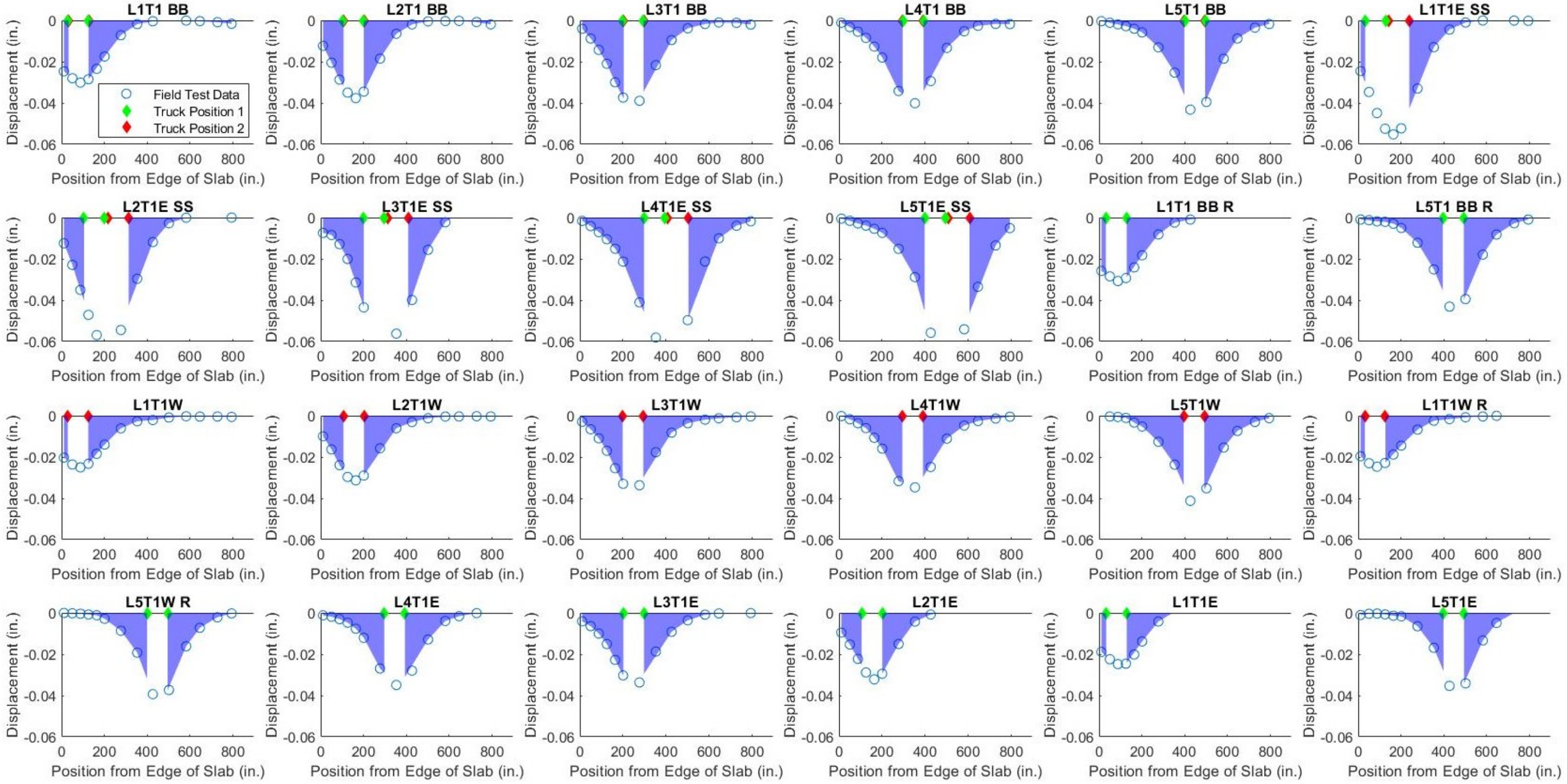

Figure K.2: Displacement profiles from live load tests on Bridge 27925